UNIVERSITY OF ŽILINA
Faculty of Mechanical Engineering
Department of Materials Engineering

UNIVERSITY OF ŽILINA
Faculty of Mechanical Engineering

Department of Materials Engineering

SEMDOK 2026

29th International Seminar of Ph.D. Students

MATERIALS
SCIENCE
MASTERS

Western Tatras - Zuberec, Slovak Republic
February 4 – February 6, 2026

Publisher

Department of Materials Engineering

Faculty of Mechanical Engineering

University of Žilina, Slovak Republic

Title

29th International Seminar of Ph.D. Students SEMDOK 2026

Kind of publication

SEMDOK Proceedings

Zostavovateľ /Editor

Assoc. prof. Ing. Lenka Kucharikovà, PhD.

Edition

First

Size

138 pages

Publisher's address

Žilinská univerzita v Žiline

Strojnícka fakulta, Katedra materiálového inžinierstva,

Univerzitná 8215/1, 010 26 Žilina

Slovak Republic

https://www.fstroj.uniza.sk/index.php

lenka.kucharikova@fstroj.uniza.sk

ISBN 978-80-554-2278-7

SEMDOK 2026

29th International Seminar of Ph.D. Students

The traditional European international seminar SEMDOK history began in the year 1996. The seminar is organized by the Department of Materials Engineering, Faculty of Mechanical Engineering, University of Žilina.

This seminar is organized for Ph.D. students and offers them an opportunity to present and discuss their scientific interests with experts and Ph.D. students from different countries and fields of Technology, Engineering, and Materials Sciences (CZ, IT, PL, SRB, and SK). The seminar lasts three days every year. The language is English to prepare students for the international symposiums awaiting them during their studies and for international student internships. Each article is reviewed by two reviewers. The selected papers accepted by the scientific committee are published in some journals in addition to this proceeding.

This scientific undertaking was realized in the framework of projects:

- *VEGA, 1/0461/24 – "Štúdium novej generácie sekundárnych (recyklovaných) Al-zliatin" (zodp. riešiteľ prof. Ing. Eva Tillová, PhD.);*
- *VEGA 1/0729/26 - „Štúdium mechanizmov ovplyvňujúcich únavovú odolnosť a vnútorné tlmenie austenitických ocelí po plastickej deformácii", (zodp. riešiteľ doc. Ing. Milan Uhríčik, PhD.).*

Welcome, we hope you will have a pleasant stay at Western Tatras, Zuberec,
Slovak Republic.
Organizing Committee

SEMDOK 2026

29th International Seminar of Ph.D. Students

Western Tatras - Zuberec, Slovak Republic
February 4 – February 6, 2026

* * *

International Scientific Committee

prof. Ing. Otakar Bokůvka, PhD. (SK)
prof. Ing. Peter Palček, PhD. (SK)
prof. Ing. Eva Tillová, PhD. (SK)
prof. Ing. Branislav Hadzima, PhD. (SK)
prof. Ing. František Nový, PhD. (SK)
Assoc. prof. Ing. Lenka Kuchariková, PhD. (SK)
Assoc. prof. Ing. Libor Trško, PhD. (SK)
Assoc. prof. Ing. Milan Uhríčik, PhD. (SK)
prof. Dr. Ing. Ružica Nikolić (SRB)
Dr.h.c. prof. Ing. Mario Guagliano (IT)
prof. dr hab. inż. Robert Ulewicz (PL)
prof. P.Cz. dr hab. inż. Jacek Selejdak (PL)
dr hab. inż. Mgdalena Mazur (PL)
dr h.c. dr hab. inż. Mirosław Bonek, prof. PŚ. (PL)
prof. dr hab. inż. Tomasz Tański (PL)
dr hab. inż. Marek Roszak, prof. PŚ. (PL)
prof. Ing. Eva Schmidová, PhD. (CZ)

* * *

National Organizing Committee

prof. Ing. Otakar Bokůvka, PhD.
prof. Ing. František Nový, PhD.
Assoc. prof. Ing. Lenka Kuchariková, PhD.
Assoc. prof. Ing. Milan Uhríčik, PhD.
Ing. Martin Vicen, PhD.

SEMDOK 2026

29th International Seminar of Ph.D. Students

Western Tatras - Zuberec, Slovak Republic
February 4 – February 6, 2026

****

All papers were reviewed by two members of the International Scientific Committee and the Department of Materials Engineering- UNIZA.

Reviewers

prof. Ing. Otakar Bokůvka, PhD.
prof. Ing. Peter Palček, PhD.
prof. Ing. Eva Tillová, PhD.
prof. Ing. Radomila Konečná, PhD.
prof. Ing. Branislav Hadzima, PhD.
Assoc. prof. Ing. Libor Trško, PhD.
Assoc. prof. Ing. Milan Uhríčik, PhD.
prof. dr hab. inż. Robert Ulewicz
prof. P.Cz. dr hab. inż. Jacek Selejdak
dr hab. inż. Mgdalena Mazur
dr h.c. dr hab. inż. Mirosław Bonek, prof. PŚ.
prof. dr hab. inż. Tomasz Tański
dr hab. inż. Marek Roszak, prof. PŚ.
Dr.h.c. prof. Ing. Mario Guagliano
prof. Ing. František Nový, PhD.
Assoc. prof. Ing. Lenka Kuchariková, PhD.
Assoc. prof. Ing. Juraj Belan, PhD.
RNDr. Viera Zatkalíková, PhD.
Ing. Lenka Markovičová, PhD.
Ing. Zuzana Straková, PhD.

****

Note: Authors are responsible for the language contents of their papers

AUTHORS INDEX

29th International Seminar of Ph.D. Students

SEMDOK 2026

Western Tatras – Zuberec, Slovak Republic
February, 4 to February 6, 2026

AN IMPROVED MATERIAL MODEL TO ACCURATELY PREDICT THE DEFORMATION OF COLD SPRAY PARTICLES

Xuanyu Ge[1], **Mario Guagliano**[1*]
[1] Politecnico di Milano, Department of Mechanical Engineering, Milan, Italy
**Corresponding author: mario.guagliano@polimi.it, 00390223998206, Via Giuseppe La Masa, 1, 20156 Milan, Italy*

1. Introduction

Cold spray (CS) is a solid-state coating deposition process in which micron-scale particles are propelled at high velocities, typically ranging from 300 to 1200 m/s, by a compressed and preheated gas stream to impact a substrate and build up a coating [1]. Compared with fusion-based manufacturing methods, CS offers several notable benefits, including high deposition efficiency, the ability to produce thick deposits, and broad material compatibility, while effectively minimizing residual stresses [2]. Owing to these advantages, CS has gained increasing attention as a promising additive manufacturing technique for various classes of materials [3]. However, a persistent limitation of CS is the relatively low ductility commonly observed in as-deposited materials, as reported in previous studies [4], which constrains the broader application of CS-fabricated or coated components. While post-spray heat treatment has been shown to markedly enhance ductility [5], it partially undermines the principles of rapid manufacturing. Consequently, a fundamental understanding of particle–substrate bonding mechanisms in CS is essential for optimizing process parameters and achieving the desired mechanical performance in as-sprayed deposits.

Experimental investigation of deposition mechanisms in cold spray (CS) is challenging and costly due to the micron-scale particle size and extremely high impact velocities. Although high-speed imaging and electron microscopy have been used to observe particle impacts and infer bonding mechanisms, their ability to fully resolve the transient deformation process remains limited [6,7]. As a result, numerical simulations have become an effective approach for studying particle impact behavior in CS [8]. In such simulations, the constitutive material model is critical for accurately capturing the severe plastic deformation during impact. The Johnson–Cook (JC) model [9], despite its widespread use, has been shown to overestimate particle deformation because it was developed for strain rates far below those encountered in CS. Consequently, modified JC models and alternative constitutive formulations have been proposed [10]. Among these, the Ma–Wang (MW) model [11] has gained attention due to its ease of calibration and reported agreement with experiments; however, our simulations of high-velocity cold-sprayed copper (Cu) particles reveal noticeable discrepancies with experimental results, particularly in predicting overall deformation and localized jetting behavior.

Thus, in this study, we proposed a new material model to accurately predict the deformation of cold spray particles. The proposed formulation incorporates the coupled influences of strain hardening, strain-rate sensitivity, and thermal softening on material flow stress while maintaining a relatively simple mathematical structure. The model was applied to simulate cold spray (CS) deposition of Cu particles over a wide range of impact velocities, from 590 to 1058 m/s. Comparison with corresponding experimental results demonstrates that the proposed model provides improved predictive accuracy, particularly in reproducing particle deformation behavior and localized jet formation.

2. New material model

To more accurately capture the deformation of CS deposited particles, a new material model was developed. Compared with the MW model [11], the proposed model primarily modifies the normal strain rate and the thermal softening terms, as follows:

$$\sigma_y = \left[\underbrace{\left(\sigma_{y0} + A\varepsilon_p{}^n\right)}_{\text{Strain hardening}} + \underbrace{\left(\alpha\varepsilon_p{}^n + \beta\right) ln\left(\frac{\dot{\varepsilon}_p}{\dot{\varepsilon}_s}\right)}_{\text{Normal strain rate}} + \underbrace{Bln\left(\frac{\dot{\varepsilon}_p}{\dot{\varepsilon}_u}\right)}_{\text{High strain rate}} \right] \underbrace{\left(\frac{1+e^{(T_r - T_{ref})\eta}}{1+e^{(T - T_{ref})\eta}}\right)}_{\text{Thermal softening}} \tag{1}$$

Here, the flow stress σ_y is expressed as a function of the equivalent plastic strain ε_p, equivalent plastic strain rate $\dot{\varepsilon}_p$, and temperature T. The parameters $\dot{\varepsilon}_s$ and $\dot{\varepsilon}_u$ denote the reference equivalent plastic strain rates corresponding to the normal and high strain-rate hardening regimes, respectively. T_r represents the room temperature, while T_{ref} is the reference temperature at which the reduction in flow stress is most pronounced. The parameter η is a fitting coefficient that governs the rate of flow stress degradation and is assumed to be dependent on the equivalent plastic strain rate.

Thus, the flow stress can be determined by four main terms in the proposed model: strain hardening, strain rate hardening for normal strain rate, strain rate hardening for high strain rate and thermal softening. The material parameters of the proposed model can be calibrated by the experimental data [11,12], they are listed in Table 1.

Tab. 1 *Material parameters of the proposed model*

Young's modulus E (GPa)	128	**n**	0.41
Poisson's ratio v	0.34	**α (MPa)**	7.5
Density ρ (kg/m^3)	8960	**β (MPa)**	0.01
Specific heat c_p (J·kg^{-1}·°C^{-1})	384.6	**$\dot{\varepsilon}_s$ (s^{-1})**	0.001
Conductivity k (W·m^{-1}·°C^{-1})	385	**$\dot{\varepsilon}_u$ (s^{-1})**	10000
Taylor-Quinney coefficient Q	0.75	**B (MPa)**	110
σ_{y0} (MPa)	39	**T_{ref} (°C)**	220
A (MPa)	320	**η (°C^{-1})**	0.003

Numerical simulations of single Cu particle deposition onto a Cu substrate were carried out using an Eulerian formulation implemented in Abaqus. Consistent with the experimental work [13], the particle diameter was chosen to be 10 µm. To accurately resolve the impact zone, a refined mesh with an element size of *h=d/50* was employed in the vicinity of particle–substrate impact region, whereas a coarser mesh was adopted in other regions. The proposed constitutive model was implemented through VUMAT subroutine. In addition, a thermally coupled analysis was performed using a thermal-displacement step in combination with EC3D8RT to evaluate the temperature evolution during impact.

3. Results and discussion

Figure 1 presents a comparison between the experimentally observed morphologies of deposited particles and the corresponding simulation results predicted by the proposed material model. The results indicate that the model is capable of accurately reproducing the deformation behavior of CS Cu particles over a wide range of impact velocities from 590 to 1058 m/s. With increasing impact velocity, deeper particle penetration into the substrate was observed, accompanied by pronounced material jetting.

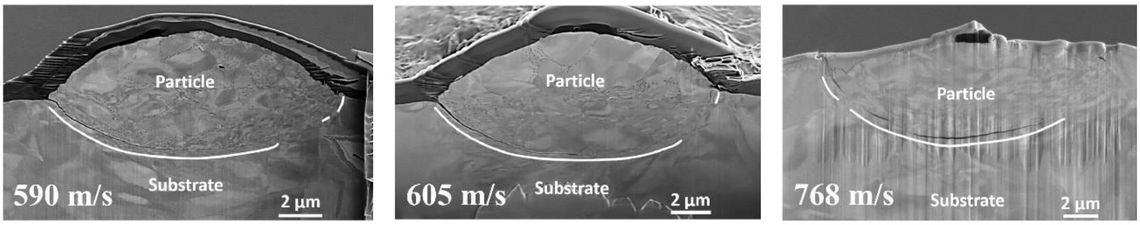

a) Experiment-590 m/s *b) Experiment-605 m/s* *c) Experiment-768 m/s*

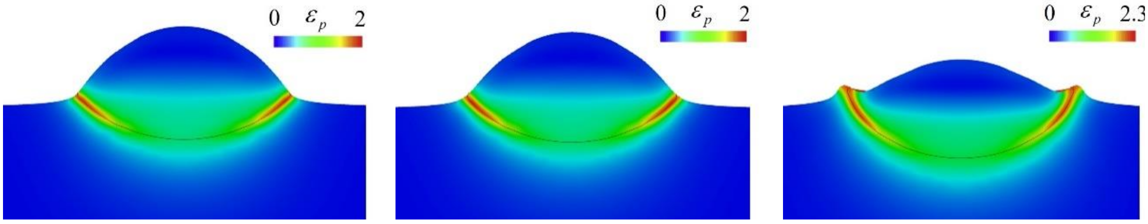

d) Simultaion-590 m/s *e) Simultaion-605 m/s* *f) Simultaion-768 m/s*

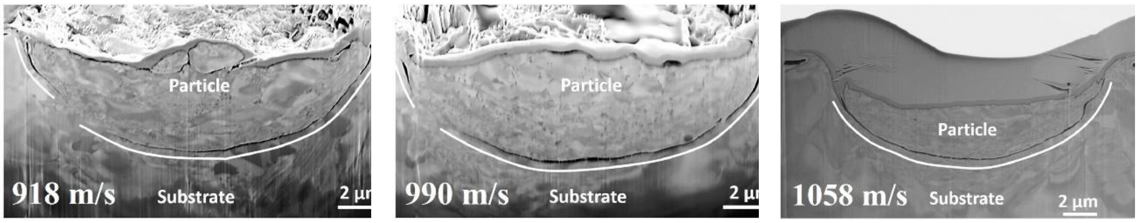

g) Experiment-918 m/s *h) Experiment-990 m/s* *i) Experiment-1058 m/s*

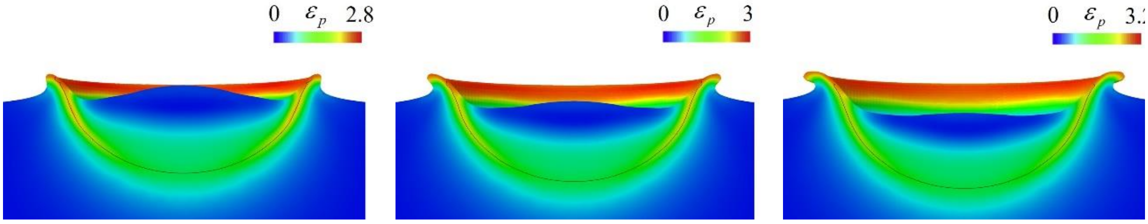

j) Simultaion-918 m/s *k) Simultaion-990 m/s* *l) Simultaion-1058 m/s*

Fig. 1 *Comparison between the experimental [13] and simulated morphologies.*

The particle profiles were obtained from experimental observations and numerical simulations for a detailed comparative analysis, as illustrated in Fig. 2. The comparison demonstrated that the proposed material model provided a more reliable description of the global deformation behavior of the particles, while also offering an improved representation of the localized jet formation resulting from thermal softening effects.

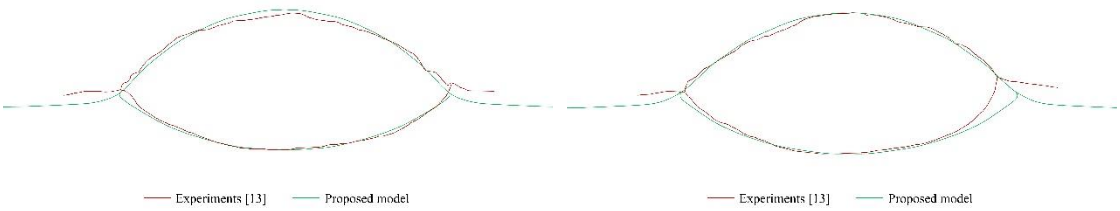

a) 590 m/s *b) 605 m/s*

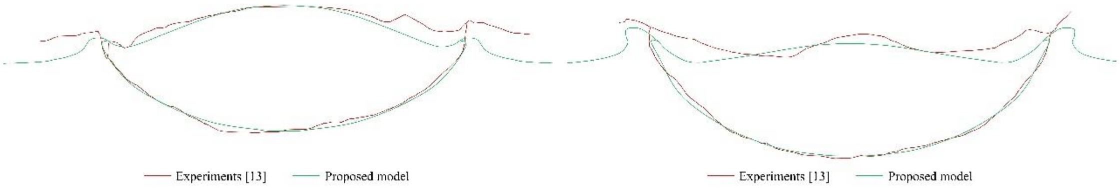

c) 768 m/s *d) 918 m/s*

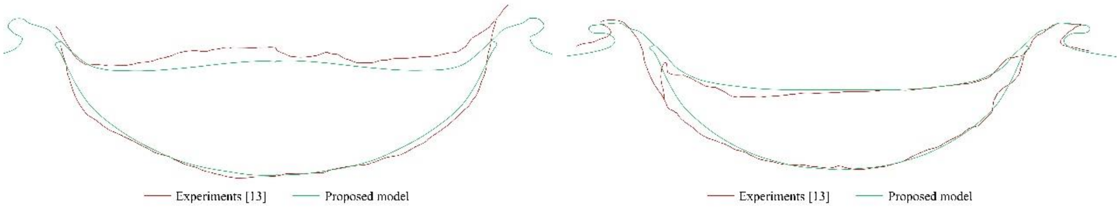

e) 990 m/s *f) 1058 m/s*

Fig. 2 *Overlapped particle profiles for comparison between the experimental data [13] and the simulated results.*

4. Conclusion

In this study, an improved material model was proposed to accurately predict the deformation of CS particles. The impact of Cu particle on Cu substrate was simulated using the proposed model and the results were compared with the experimental observations.

The proposed constitutive material model successfully captured the key deformation characteristics of CS particles, including overall plastic deformation and localized jetting behavior across a broad impact velocity range of 590–1058 m/s. By accounting for strain hardening, strain-rate sensitivity, and thermal softening effects, the model provides a robust and adaptable framework that can be efficiently calibrated using experimental data and extended beyond Cu to other metallic materials for CS simulations.

Acknowledgment

X.G. acknowledges the Chinese Scholarship Council (CSC) for the financial support (No. 202306290021).

References

[1]Li, W., Yang, K., Yin, S., Yang, X., Xu, Y., Lupoi, R.: Solid-state additive manufacturing and repairing by cold spraying: A review. Journal of Materials Science & Technology, Vol. 34, pp. 440–457, 2018.

[2]Bagherifard, S., Monti, S., Zuccoli, M.V., Riccio, M., Kondás, J., Guagliano, M.: Cold spray deposition for additive manufacturing of freeform structural components compared to selective laser melting. Materials Science and Engineering A, Vol. 721, pp. 339–350, 2018.

[3]Bagherifard, S., Kondas, J., Monti, S., Cizek, J., Perego, F., Kovarik, O., Lukac, F., Gaertner, F., Guagliano, M.: Tailoring cold spray additive manufacturing of steel 316L for static and cyclic load-bearing applications. Materials & Design, Vol. 203, pp. 109575, 2021.

[4]Julien, S.E., Nourian-Avval, A., Liang, W., Schwartz, T., Ozdemir, O.C., Müftü, S.: Bulk fracture anisotropy in cold-sprayed Al 6061 deposits. Engineering Fracture Mechanics, Vol. 263, pp. 108301, 2022.

[5]Huang, C., Arseenko, M., Zhao, L., Xie, Y., Elsenberg, A., Li, W., Gärtner, F., Simar, A., Klassen, T.: Property prediction and crack growth behavior in cold sprayed Cu deposits. Materials & Design, Vol. 206, pp. 109826, 2021.

[6]Yin, S., Hassani, M., Xie, Q., Lupoi, R.: Unravelling the deposition mechanism of brittle particles in metal matrix composites fabricated via cold spray additive manufacturing. Scripta Materialia, Vol. 194, pp. 113614, 2021.

[7]Assadi, H., Gärtner, F., Stoltenhoff, T., Kreye, H.: Bonding mechanism in cold gas spraying. Acta Materialia, Vol. 51, pp. 4379–4394, 2003.

[8]Fardan, A., Berndt, C.C., Ahmed, R.: Numerical modelling of particle impact and residual stresses in cold sprayed coatings: A review. Surface and Coatings Technology, Vol. 409, pp. 126835, 2021.

[9]Johnson, G.R., Cook, W.H.: Fracture characteristics of three metals subjected to various strains, strain rates, temperatures and pressures. Engineering Fracture Mechanics, Vol. 21, No. 1, pp. 31–48, 1985.

[10]Chakrabarty, R., Song, J.: A modified Johnson–Cook material model with strain gradient plasticity consideration for numerical simulation of cold spray process. Surface and Coatings Technology, Vol. 397, pp. 125981, 2020.

[11]Wang, Q., Ma, N., Luo, X., Li, C.: Towards better understanding supersonic impact-bonding behavior of cold sprayed 6061-T6 aluminum alloy based on a high-accuracy material model. Additive Manufacturing, Vol. 48, pp. 102469, 2021.

[12]Follansbee, P.S., Kocks, U.F.: A constitutive description of the deformation of Cu based on the use of the mechanical threshold stress as an internal state variable. Acta Metallurgica, Vol. 36, No. 1, pp. 81–93, 1988.

[13]Tiamiyu, A.A., Sun, Y., Nelson, K.A., Schuh, C.A.: Site-specific study of jetting, bonding, and local deformation during high-velocity metallic microparticle impact. Acta Materialia, Vol. 202, pp. 159–169, 2021.

EXPERIMENTAL INVESTIGATION OF HYDROGEN EMBRITTLEMENT IN WELDED JOINTS OF S960MC STEEL

Branislav Hajas[1]**, Denisa Straková**[1]***, Lukáš Šikyňa**[1]**, František Nový**[1]

[1] *University of Žilina in Žilina, Faculty of Mechanical Engineering, Department of Materials Engineering, Slovak Republic*
**Corresponding author: denisa.strakova@uniza.sk*

1. Introduction

Hydrogen embrittlement represents a major limitation in the application of advanced high-strength steels, particularly in welded joints where microstructural heterogeneity and residual stresses facilitate hydrogen-assisted degradation [1]. The fundamental mechanisms governing hydrogen diffusion, trapping, and fracture behaviour—most notably hydrogen-enhanced localized plasticity (HELP) and hydrogen-enhanced decohesion (HEDE)—have been widely discussed in the literature [2,3].

Although advanced high-strength steels are increasingly used due to their favourable strength-to-weight ratio, their susceptibility to hydrogen embrittlement significantly affects the structural reliability of welded components [4,5]. The present study directly follows a previously published theoretical work [1] and aims to experimentally verify the proposed mechanisms using welded joints of S960MC steel, with emphasis on correlating mechanical property degradation with microstructural evolution and fracture mechanisms.

2. Experimental Material and Methods

The investigated material was thermomechanically processed high-strength steel S960MC, supplied as sheets with thicknesses of 3 mm (base material) and 4 mm (welded joints). The chemical composition complied with the manufacturer's specifications [6].

Tab. 1 *Chemical composition of S960MC steel [wt. %]*

C	*Si*	*Mn*	*P*	*S*	*Nb*	*V*	*Ti*	*Fe*
0.08–0.14	*0.18–0.30*	*1.10–1.31*	*≤0.02*	*≤0.01*	*<0.004*	*0.01–0.04*	*0.01–0.02*	*Balance*

Welded joints were produced using the TIG welding method under fully automated conditions to ensure reproducibility. Welding was performed using a 2.4 mm tungsten electrode at a current of 170 A, voltage of 12 V, welding speed of 3.5 $\text{mm}\cdot\text{s}^{-1}$, and shielding gas flow rate of 12 $\text{L}\cdot\text{min}^{-1}$. Flat tensile specimens were prepared in accordance with DIN 50125:2009-07, type E, using wire electrical discharge machining for welded specimens and laser cutting for non-welded specimens (Fig. 1).

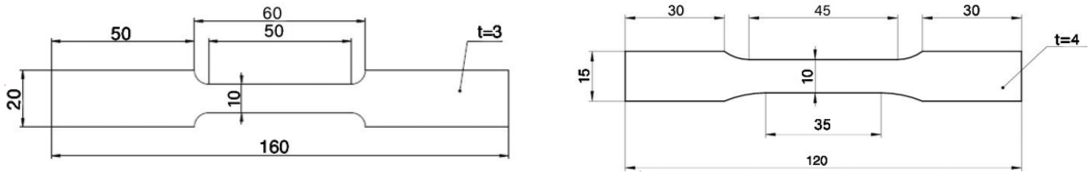
a)
b)

Fig. 1 *Schematic representation of specimen geometry for tensile testing: a) with welded joint; b) without welded joint [mm].*

Electrolytic hydrogen charging was performed using a direct current power supply (Mastech HY3003-3) with a platinized tungsten counter electrode. Specimens were partially immersed to avoid electric-field distortion and charged at 20 ± 3 °C using current densities of 30–50 $mA \cdot cm^{-2}$ for welded joints and 50–70 $mA \cdot cm^{-2}$ for base material specimens, with exposure times of 8–24 h. The effective hydrogen-exposed surface area (PV) was calculated from specimen geometry according to Eq. (1):

$$PV = 2A + (P - 15)t\ [mm^2], \qquad (1)$$

where A is the surface area of one specimen face, P the specimen perimeter, and t the specimen thickness.

Tensile testing was performed in accordance with ISO 6892-1 using an Instron 5985 universal testing machine immediately after hydrogen charging to minimize hydrogen desorption. Microstructural and fractographic analyses were conducted using optical microscopy and scanning electron microscopy (SEM with EDS). Vickers microhardness measurements (HV0.5) were carried out according to ISO 6507 across the weld metal, heat-affected zone, and base material.

3. Results and Discussion

Tensile test results (Table 3, Fig. 2) show that hydrogen charging has a negligible effect on yield strength and ultimate tensile strength, while causing a substantial reduction in ductility, consistent with hydrogen-assisted damage mechanisms reported in the literature [7]. In welded specimens, fracture occurred within the heat-affected zone. In the reference condition, failure was localized in the subcritical heat-affected zone (SCHAZ), in agreement with observations by Mičian [8].
After hydrogen charging, fracture occurred exclusively in the intercritical heat-affected zone (ICHAZ) and exhibited a sharper, more brittle character, indicating reduced ductility and enhanced hydrogen embrittlement.

***Tab. 2** Tensile properties before and after hydrogen charging.*

Specimen	Yield strength [MPa]	UTS [MPa]	Elongation [%]
Base material reference	1070	1141	7.3
Base material H charged	1057–1123	1074–1160	1.05–1.7
Welded joint reference	989	1049	8.47
Welded joint H charged	983–1023	1029–1069	2.81–4.69

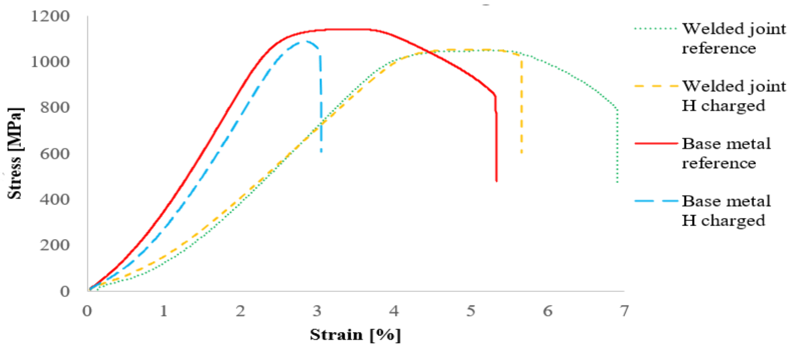

***Fig. 2** Stress–strain curves of reference and hydrogen-charged specimens*

Microhardness measurements across the welded joint enabled clear identification of individual heat-affected zone subregions (Fig. 3). The base material exhibited a reference hardness of 341 HV0.5, while a pronounced decrease was observed in the heat-affected zone, with a minimum value of 244 HV0.5 in the ICHAZ due to partial austenitization and formation of softer phases [9]. This local mechanical weakening increases susceptibility to hydrogen-assisted cracking.

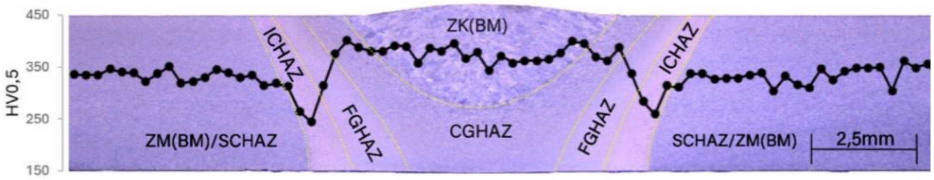

Fig. 3 *Microhardness distribution across the transverse cross-section steel welded joint.*

Fractographic analysis revealed predominantly brittle fracture features characterized by cleavage facets and river patterns, accompanied by limited regions of ductile dimple morphology (Fig. 4). Hydrogen-induced damage was preferentially associated with segregation bands and inclusion-rich regions, confirming non-uniform hydrogen distribution. The fracture behaviour reflects a synergistic interaction of HEDE-dominated brittle fracture and locally activated HELP mechanisms.

4. Conclusion

The experimental results provide strong validation of previously proposed theoretical models of hydrogen embrittlement in high-strength steel welds. Electrolytic hydrogen charging causes a severe reduction in ductility and promotes fracture initiation in critical heat-affected zone regions, particularly the ICHAZ. The observed degradation behaviour is governed by the synergistic interaction of HELP and HEDE mechanisms. These findings highlight the importance of controlling hydrogen sources and welding parameters to mitigate hydrogen-assisted cracking in advanced high-strength steel structures.

Acknowledgements

This research was financially supported by the Ministry of Education, Research, Development and Youth of the Slovak Republic under contract numbers 1/0831/25 and 1/0044/22.

References

[1] Hajas, B., Straková, D. (2026). *Overview of hydrogen embrittlement in weld joints of high-strength steels: Mechanisms, risks, and mitigation*. In Proceedings of the International Students Scientific Conference TALENTDETECTOR2026_WINTER (Gliwice, Poland, January 9, 2026). Silesian University of Technology.

[2] Chen, Y.-S., Huang, C., Liu, P.-Y., Yen, H.-W., Niu, R., Burr, P., Moore, K. L., Martínez-Pañeda, E., Atrens, A., Cairney, J. M. (2025). *Hydrogen trapping and embrittlement in metals – A review*. International Journal of Hydrogen Energy, 136, 789–821. https://doi.org/10.1016/j.ijhydene.2024.04.076.

[3] Djukic, M. B., Bakic, G. M., Zeravcic, V. S., Sedmak, A., & Rajicic, B. (2015). *Hydrogen damage of steels: A case study and hydrogen embrittlement model*. Engineering Failure Analysis, 58, 485–498. https://doi.org/10.1016/j.engfailanal.2015.05.017.

[4] Padhy, G. K., Komizo, Y. (2013). *Diffusible hydrogen in steel welds: A status review*. Transactions of the Joining and Welding Research Institute, 42(2), 1–14.

[5] Xue, J., Guo, W., Xia, M., Zhang, Y., Tan, C., Shi, J., Li, X., Zhu, Y., & Zhang, H. (2024). *In-depth understanding in the effect of hydrogen on microstructural evolution, mechanical properties and fracture micro-mechanisms of advanced high-strength steels welded joints*. Corrosion Science, 233, 112112. https://doi.org/10.1016/j.corsci.2024.112112 .

[6] SSAB. *Strenx® 960 MC structural steel*. Available online: https://www.ssab.com/en/brands-and-products/strenx/product-offer/960/mc (accessed 8th Jan 2026).

[7] Depover, T., Laureys, A., Perez Escobar, D., Wallaert, E., Verbeken, K. *Effect of hydrogen charging on the mechanical properties of advanced high strength steels.* International Journal of Hydrogen Energy, 39(9), 4647–4656 (2014). https://doi.org/10.1016/j.ijhydene.2013.12.190.

[8] Mičian, M. (2024). *Vplyv procesu zvárania na zmenu vlastností teplom ovplyvnenej oblasti ocele S960MC*. EDIS. ISBN 978-80-554-2062-2.

[9] Sun, Z., *et al.* (2025). *Investigation on the mechanical properties of the heat-affected zone of butt-welded joints of Q690 and Q960 steel based on physical thermal simulation*. Construction and Building Materials, 471, 140684.

Non-welded H charged ***TIG welded H charged***

a) overall fracture surfaces

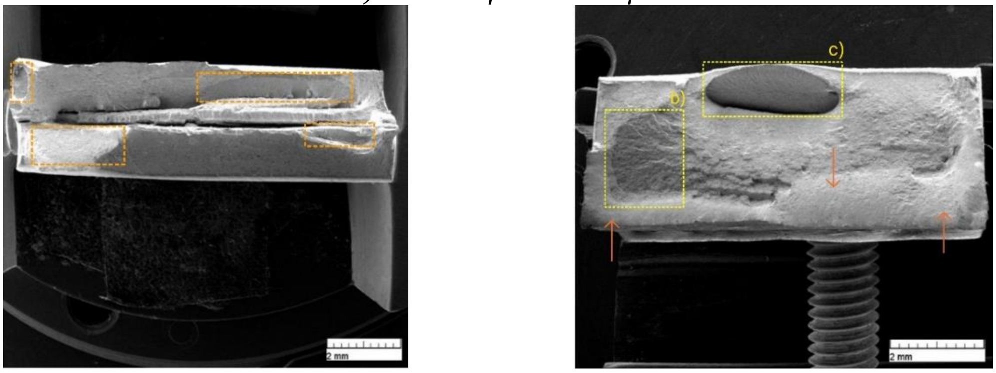

b) details

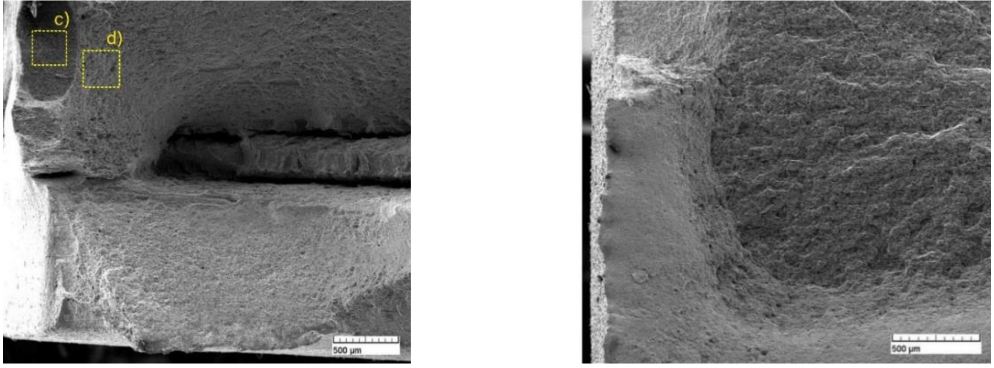

c) cleavage fracture surface morphology (HEDE)

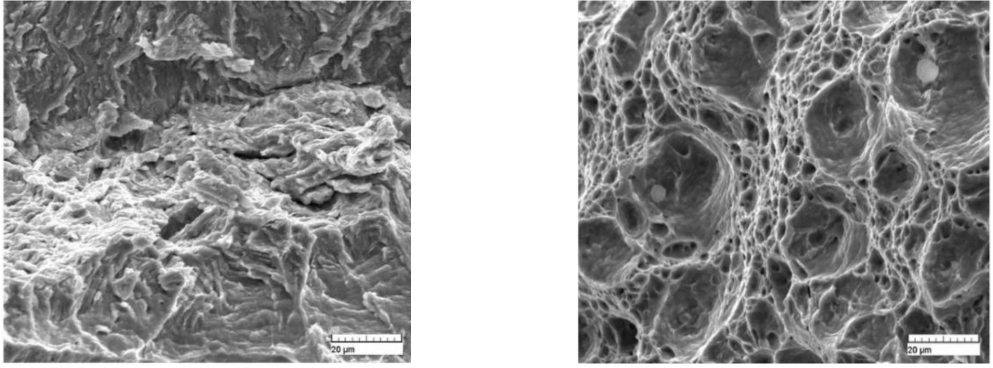

d) dimple fracture surface morphology (HELP)

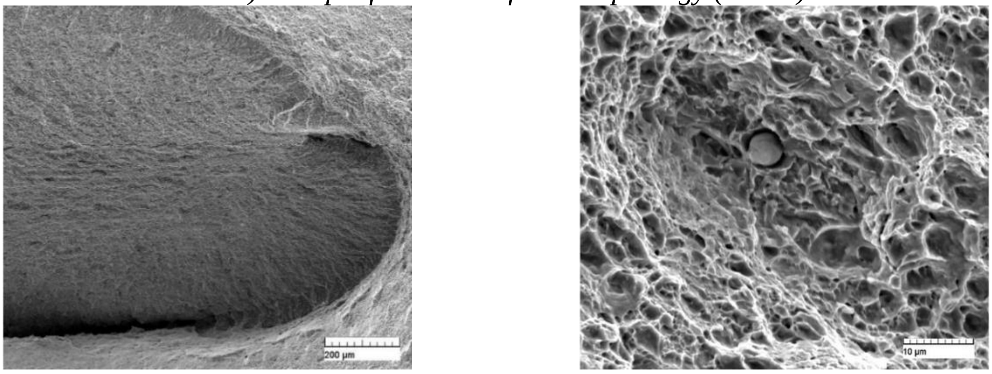

Fig. 4 *Fracture surfaces of non-welded and welded specimens after hydrogen charging.*

29th International Seminar of Ph.D. Students

SEMDOK 2026

Western Tatras – Zuberec, Slovak Republic
February, 4 to February 6, 2026

THE INFLUENCE OF COMBINED SURFACE TREATMENT ON CORROSION BEHAVIOUR OF AZ31 MAGNESIUM ALLOY

Ľuboš Halimovič[1,2*], Filip Pastorek[2], Branislav Hadzima[2]
[1] Department of Physics, Faculty of Electrical Engineering and Information Technology, University of Žilina, Univerzitná 8215/1, 010 26 Žilina, Slovak Republic
[2] Research Centre UNIZA, University of Žilina, Univerzitná 8215/1, 010 26 Žilina, Slovak Republic
**Corresponding author: halimovic.lubos@feit.uniza.sk, +421 41 513 7605, Department of Physics, Faculty of Electrical Engineering and Information Technology, University of Žilina, Univerzitná 8215/1, 010 26 Žilina, Slovak Republic*

1. Introduction

Magnesium and its alloys are well-known materials in the automotive and biomedical industries [1,2]. In technical applications, these materials are mainly used due to their low density. Another advantage is the possibility of obtaining the magnesium from seawater, for example, which is both environmentally and economically beneficial [2]. However, these materials suffer from one of the major problem – corrosion. The standard electrode potential of pure magnesium is – 2.36 V, which indicates very low thermodynamic stability. Due to this fact, in magnesium alloy systems, magnesium is polarized as anode, while other alloying elements or intermetallic phases are polarized as cathodes. This phenomena leads to formation of micro-galvanic couples and subsequently to micro-galvanic. As result, the degradation of the alloy occurs [3]. The corrosion process proceeds when a corrosion environment is present. To stop or slow down this process, it is necessary to prevent contact between the alloy and the corrosion environment. One possible solution is surface treatment. There are many possibilities for surface modification, such as chip machining [4,5]or heat treatment processes, shot-peening [6], laser ablation [7] or laser melting. These types of surface treatment can be classified as pre-treatment methods.

Another approach to the surface treatment is use of conversion coatings. The conversion coatings utilize the oxidizing ability of the material [8]. There are many ways to obtain resulting coating; however, chemical and electrochemical proceedings are probably the best known and most widely used. One of these methods is plasma electrolytic oxidation (PEO). The PEO coatings exhibits significantly higher corrosion resistance than conventionally machined surfaces or only pre-treated surfaces. However, they are porous and therefore gradually lose their protective function over time [6]. For this reason, efforts are focused on sealing the pores as effectively as possible, thereby increasing the durability and effectiveness of these coatings [9].

In this study the influence of combined surface treatment on electrochemical behaviour of AZ31 magnesium alloy is investigated. A three-step surface treatment was applied: laser ablation as pre-treatment, PEO treatment and sealing of the PEO coating with polylactic acid (PLA) polymer.

2. Materials and methods

2.1 Experimental material

The AZ31 magnesium alloy was used as an experimental material. The chemical composition was determined using spectrometer EDXRF Thermo ARL Quant X.

2.2 Surface treatment

The samples of the AZ31 magnesium alloy were cut into pieces with dimensions of 20 x 10 x 7 mm. The surfaces of the samples were ground by SiC emery papers up to P1200, with water used as a coolant. Subsequently, the samples were treated by laser ablation using a pulse laser QFC-LP Cleaning Laser (P-Laser INDUSTRIAL LASER CLEANING, Heusden – Zolder, Belgium). The work distance was set to 300 mm. Full surface coverage by the laser beam was secured. The maximum output power of 100 W was used.

The chemical composition of the PEO electrolyte consisted of 12 g/L $Na_3PO_4 \cdot 12H_2O$, 1 g/L KOH and 1 g/L TiO_2 particles (size of the TiO_2 particles 420 nm ± 20 nm) [6,10,11]. The three-step electrolyte preparation procedure was applied. In the first step the, $Na_3PO_4 \cdot 12H_2O$ and KOH agents were solved in the DEMI water. Due to the low solubility of the TiO_2 particles in water [12], the particles were dispersed in 100 ml of DEMI water by sonic homogenizer for 30 seconds. Subsequently, the dispersed particles were added to the pre-prepared electrolyte. As the final step of the electrolyte preparation, the electrolyte was stirred for 24 hours [11].

The PEO process was carried out by KEYSIGHT N8762A DC power supply. The DC regime was used with applied current density of 0.05 $A.cm^{-2}$ for each sample. The PEO treatment time was set to 14 minutes [13]. The PEO bath was continuously cooled to ensure stable bath temperature. During the PEO process, the sample was polarized as anode (positive charge),while a stainless steel electrode was used as the cathode (negative charge). The distance between the anode and cathode was set to 10 cm.

2.3 Sealing process

Polylactic acid (PLA) was used as a polymer sealant for the PEO coating. The sealing process was carried out using a polymer solution prepared by dissolving PLA in dichloromethane (CH_2Cl_2) to obtain a 3 wt.% PLA-CH_2Cl_2 solution. Subsequently, the solution was stirred for 3 hours to ensure homogeneous distribution of polymer. The PEO treated samples were immersed in the solution for 5 minutes. During the immersion of the samples the solution was stirred (Fig. 1). Subsequently, the samples were dried in vertical position at room temperature for 24 hours.

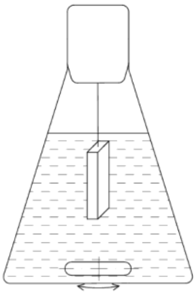

Fig. 1 *Scheme of the PLA sealing process*

2.4. Corrosion testing

The electrochemical impedance spectroscopy (EIS) was used to evaluate corrosion behaviour of the PEO coated and PEO/PLA coated samples. The measurements were carried out in 0.1 M NaCl solution at room temperature. A three-electrode cell system was used, with electrodes connected to a Biologic VSP-300 potentiostat (Biologic, Seyssinet-Pariset, France). The sample served as the working electrode, a platinum electrode as the counter electrode and the standard calomel electrode (+ 0.2448 V vs. SHE) was used as the reference electrode. The exposed surface area was 1 cm^2. The frequency range was set from 10^5 to 10^{-2} Hz. The amplitude of the sinusoidal signal was set to 10 mV vs. open circuit potential (OCP). The EIS measurements were performed after OPC stabilization times of 1 hour and 24 hours [13].

The obtained data were plotted as Nyquist plots and analyzed using EC-lab software by the equivalent circuits method (Fig. 2). The R_s represents the electrolyte resistance.
When the first capacitive loop is smaller and the second was larger, the equivalent circuit shown in the Fig. 2a was used. In this case, the R_{p1} corresponds to the surface polarization resistance and CPE_1 (constant phase element) represents the quasi-capacitance of the surface. The parameters R_{p2} and CPE_2 describe the properties of the second, separately distinguishable part of the surface [14].

If the first capacitive loop is larger than the second the R_{p1} and CPE_1 are adjoined with the outer part of the surface, for example the coating and the R_{p2}, CPE_2 represent the inner part of the coating, such as or pores at the bottom of the coating or pits. In this case the circuit showed in Fig. 2b is used, where the surface system is partially interconnected. The main evaluated characteristic was the total polarization resistance R_{sum}, calculates as the sum of the individual polarization resistances ($R_{sum} = R_{p1} + R_{p2}$).

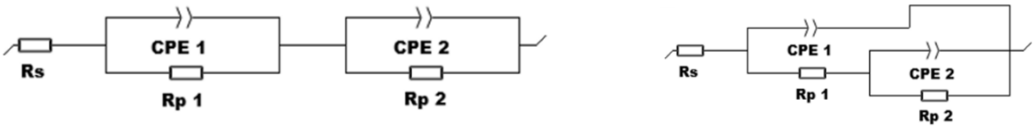

a) equivalent circuit for two conductive loop (1^{st} loop is smaller)

b) equivalent circuit for two conductive loop (1^{st} loop is larger)

Fig. 2 *Schemes for equivalent circuits*

3. Results and discussion

3.1 Chemical composition results

In the Tab. 1 the chemical composition of the AZ31 magnesium alloy is shown. According to the ASTM standard, the chemical composition corresponded to the specified composition.

Tab. 1 *Chemical composition*

Elements	***Al***	***Zn***	***Si***	***Mn***	***Mg***
[wt. %]	*3.21*	*0.65*	*0.57*	*0.19*	*balance*

3.2.Corrosion testing results

In The Nyquist plots are shown in the Fig. 3. Two capacitive loops were observed in all cases (PEO 1h, PEO 24h, PEO/PLA 1h, PEO/PLA 24h). The first capacitive loop was smaller than the second one ($R_{p1} < R_{p2}$) after the 1st hour of the exposure to the aggressive environment.

In case of PEO coating without the PLA sealing, the first capacitive loop (R_{p1}, CPE_1) was associated with the outer porous part of the coating, while the second capacitive loop (R_{p2}, CPE_2) represented the inner compact part of the coating. A similar behaviour was observed in case of PEO/PLA samples, however, the interpretation was different. The first capacitive loop (R_{p1}, CPE_1) was most likely related to the PLA film formed on the PEO surface, whereas the second loop represented the entire PEO coating beneath the PLA film. Nevertheless, the values of the R_{p1}, R_{p2} and R_{sum} (Tab. 2) were almost the same as in the case of PEO layer without the PLA sealing.

The first capacitive loop became larger than the second one after 24 hours of the exposure. In case of PEO sample the first capacitive loop represented the resistance of the remaining coating. The smaller second capacitive loop indicated the electrolyte penetration to the coating. This loop was associated with the charge transfer resistance at the bottom of the pores [13]. The increase in the R_s characteristic (electrolyte resistance) indicates depletion of ions in the electrolyte due to reaction with the coating, leading to the formation of corrosion products [15]. The corrosive effect of the aggressive environment is also reflected by the decrease in the R_{sum}.

A similar change in the relative size of the capacitive loops was observed in case of PEO/PLA sample. The R_p values (Tab. 2) suggest that the PLA sealing was still present however, the electrolyte penetrated into the sealed coating, as indicated by (R_{p2}). The PLA polymer film acted as a quasi-barrier or semi-permeable membrane. for the ions from the electrolyte (oxygen, hydrogen, chlorides) [16]. The ions likely diffused through the PLA sealing toward the coating, where electrochemical reactions occurred. The hydrogen evolution led to the formation of the hydrogen bubbles during the magnesium corrosion (Mg present in PEO coating) [3]. This phenomenon caused swelling of the PLA sealing and subsequently the local delamination of the sealing [17] which led to the decrease in R_{sum}.

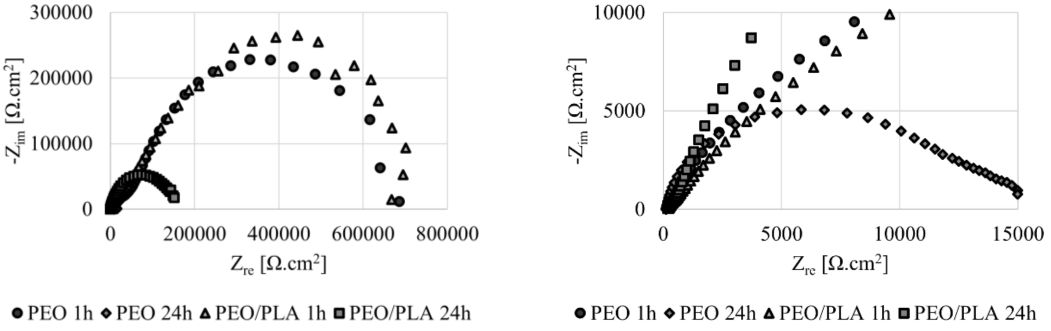

a) overview *b) detail*

Fig. 3 *Representative Nyquist plots of the treated surfaces*

Tab. 2 *The R_p characteristic of the treated surfaces*

Sample	***R_s [Ω.cm^2]***	***R_{p1} [Ω.cm^2]***	***R_{p2} [Ω.cm^2]***	***R_{sum} [Ω.cm^2]***
PEO 1h	*87*	*41986*	*630144*	*672130*
PEO 24h	*122*	*11518*	*3942*	*15460*
PEO/PLA 1h	*186*	*49879*	*692738*	*7426917*
PEO/PLA 24h	*222*	*150566*	*6945*	*157511*

4. Conclusions

The presented study proves that the combination of the pre-treatment, PEO and sealing of the PEO coatings by PLA polymer significantly improves the corrosion resistance and corrosion durability of these coatings. The degradation process of the PEO coatings is already well known and it is discussed in many scholar papers. However, the degradation of the PEO/PLA combination coatings is more complex and requires further in-depth studies.

Acknowledgment

Funded by the EU NextGenerationEU through the Recovery and Resilience Plan for Slovakia under the project No. 09I03-03-V03-00036.

References

[1] K.K. Thomas, M.N. Zafar, W.G. Pitt, G.A. Husseini, Biodegradable Magnesium Alloys for Biomedical Implants: Properties, Challenges, and Surface Modifications with a Focus on Orthopedic Fixation Repair, Applied Sciences 14 (2023) 10. https://doi.org/10.3390/app14010010.

[2] Guang-ling Song, Corrosion of magnesium alloys, Woodhead Pub. ; CRC Press, 2010.

[3] G.L. Song, A. Atrens, Corrosion Mechanisms of Magnesium Alloys, Adv Eng Mater 1 (1999) 11–33. https://doi.org/10.1002/(SICI)1527-2648(199909)1:1<11::AID-ADEM11>3.0.CO;2-N.

[4] J. Sovík, D. Kajánek, F. Pastorek, M. Štrbák, Z. Florková, M. Jambor, B. Hadzima, The Effect of Mechanical Pretreatment on the Electrochemical Characteristics of PEO Coatings Prepared on Magnesium Alloy AZ80, Materials 16 (2023) 5650. https://doi.org/10.3390/ma16165650.

[5] U. Reddy, D. Dubey, S.S. Panda, N. Ireddy, J. Jain, K. Mondal, S.S. Singh, Effect of Surface Roughness Induced by Milling Operation on the Corrosion Behavior of Magnesium Alloys, J Mater Eng Perform 30 (2021) 7354–7364. https://doi.org/10.1007/s11665-021-05933-8.

[6] D. Kajánek, F. Pastorek, B. Hadzima, S. Bagherifard, M. Jambor, P. Belány, P. Minárik, Impact of shot peening on corrosion performance of AZ31 magnesium alloy coated by PEO: Comparison with conventional surface pre-treatments, Surf Coat Technol 446 (2022) 128773. https://doi.org/10.1016/j.surfcoat.2022.128773.

[7] D. Kajánek, Ľ. Halimovič, M. Jacková, L. Doskočil, I. Zuziaková, B. Hadzima, INFLUENCE OF LASER ABLATION TREATMENT ON

ELECTROCHEMICAL CHARACTERISTICS OF AZ80 MAGNESIUM ALLOY, Communications - Scientific Letters of the University of Zilina 27 (2025). https://doi.org/10.26552/com.C.2025.039.

[8] X.B. Chen, N. Birbilis, T.B. Abbott, Review of Corrosion-Resistant Conversion Coatings for Magnesium and Its Alloys, CORROSION 67 (2011) 035005-1-035005–16. https://doi.org/10.5006/1.3563639.

[9] B. Mingo, R. Arrabal, M. Mohedano, Y. Llamazares, E. Matykina, A. Yerokhin, A. Pardo, Influence of sealing post-treatments on the corrosion resistance of PEO coated AZ91 magnesium alloy, Appl Surf Sci 433 (2018) 653–667. https://doi.org/10.1016/J.APSUSC.2017.10.083.

[10] J. Sovík, D. Kajánek, L. Trško, Z. Florková, J. Pastorková, M. Buchtík, B. Hadzima, Improvement of corrosion resistance of DC PEO coating on AZ80 magnesium alloy through two-step PEO process combined with laser cleaning, Surf Coat Technol 502 (2025) 131935. https://doi.org/10.1016/j.surfcoat.2025.131935.

[11] H. Mozafarnia, A. Fattah-Alhosseini, R. Chaharmahali, M. Nouri, M.K. Keshavarz, M. Kaseem, Corrosion, Wear, and Antibacterial Behaviors of Hydroxyapatite/MgO Composite PEO Coatings on AZ31 Mg Alloy by Incorporation of TiO2 Nanoparticles, Coatings 12 (2022) 1967. https://doi.org/10.3390/coatings12121967.

[12] C.Y. Hsu, Z.H. Mahmoud, S. Abdullaev, F.K. Ali, Y. Ali Naeem, R. Mzahim Mizher, M. Morad Karim, A.S. Abdulwahid, Z. Ahmadi, S. Habibzadeh, E. kianfar, Nano titanium oxide (nano-TiO2): A review of synthesis methods, properties, and applications, Case Studies in Chemical and Environmental Engineering 9 (2024) 100626. https://doi.org/10.1016/J.CSCEE.2024.100626.

[13] D. Kajánek, B. Hadzima, J. Buhagiar, J. Wasserbauer, M. Jacková, Corrosion degradation of AZ31 magnesium alloy coated by plasma electrolytic oxidation, Transportation Research Procedia 40 (2019) 51–58. https://doi.org/10.1016/J.TRPRO.2019.07.010.

[14] S. Fintová, J. Drábiková, F. Pastorek, J. Tkacz, I. Kuběna, L. Trško, B. Hadzima, J. Minda, P. Doležal, J. Wasserbauer, P. Ptáček, Improvement of electrochemical corrosion characteristics of AZ61 magnesium alloy with unconventional fluoride conversion coatings, Surf Coat Technol 357 (2019) 638–650. https://doi.org/10.1016/J.SURFCOAT.2018.10.038.

[15] Z.-X. Wang, L. Xu, J.-W. Zhang, F. Ye, W.-G. Lv, C. Xu, S. Lu, J. Yang, Preparation and Degradation Behavior of Composite Bio-Coating on ZK60 Magnesium Alloy Using Combined Micro-Arc Oxidation and Electrophoresis Deposition, Front Mater 7 (2020). https://doi.org/10.3389/fmats.2020.00190.

[16] J. Dai, C. Wu, J. Yang, L. Zhang, Q. Dong, L. Han, X. Li, J. Bai, F. Xue, P.K. Chu, C. Chu, Poly-lactic acid coatings on the biomedical WE43 Mg alloy: Protection mechanism and ion permeation effects, Prog Org Coat 177 (2023) 107427. https://doi.org/10.1016/j.porgcoat.2023.107427.

[17] A. Fattah-alhosseini, R. Chaharmahali, A. Rajabi, K. Babaei, M. Kaseem, Performance of PEO/Polymer Coatings on the Biodegradability, Antibacterial Effect and Biocompatibility of Mg-Based Materials, J Funct Biomater 13 (2022) 267. https://doi.org/10.3390/jfb13040267.

VPLYV PODMIENOK VALCOVANIA NA ŠTRUKTÚRU METASTABILNEJ AUSTENITICKEJ OCELE

Veronika Chvalníková[1*], Milan Uhričík[1], Michal Jambor[2], Martin Slezák[1], Lukáš Šikyňa[1]

[1]Strojnícka fakulta, Katedra materiálového inžinierstva, Žilinská univerzita v Žiline, Univerzitná 8215/1, 010 26 Žilina, Slovenská republika

[2]Ústav fyziky materiálů, Akademie věd České republiky, Žižkova 22, 616 62 Brno-střed, Česká republika

**veronika.chvalnikova@fstroj.uniza.sk, +421 41 513 2632, Strojnícka fakulta, Katedra materiálového inžinierstva, Žilinská univerzita v Žiline, Univerzitná 8215/1, 010 26 Žilina, Slovenská republika.*

1. Úvod

Austenitické nehrdzavejúce ocele predstavujú v súčasnosti dominantnú skupinu materiálov v širokom spektre priemyselných odvetví ako aj v aplikáciách leteckej a raketovej techniky. Ich široké uplatnenie vyplýva z kombinácie koróznej odolnosti, dobrej zvárateľnosti, a priaznivého pomeru medzi úžitkovými vlastnosťami a cenou. Kľúčovým faktorom zabezpečujúcim koróznu stabilitu je vysoký obsah chrómu, ktorý na povrchu vytvára pasívnu ochrannú vrstvu. Stabilita austeniticej štruktúry je podmienená rovnováhou medzi austenitotvornými prvkami a feritotvornými prvkami [1,2].

Napriek mnohým výhodám naráža aplikácia v technickej praxi na limity v podobe nízkej tvrdosti, medze klzu a odolnosti voči opotrebeniu. Tieto nedostatky je možné eliminovať procesom deformácie za studena, ktorá vedie k výraznému spevneniu materiálu. Tento proces však prináša nepriaznivé metalurgické zmeny, predovšetkým tvorbu deformačného martenzitu (α'). Táto fázová transformácia mení vlastnosti ocele a podľa viacerých štúdii vedie k degradácii koróznej odolnosti v dôsledku lokálnych zmien v matrici. Pri kovoch s plošne centrovanou kubickou mriežkou (fcc) sa vznik deformačných mechanizmov odvíja od energie vrstevnej chyby ku ktorým patria aj austenitické nehrdzavejúce ocele [3,4].

Vplyv podmienok valcovania výrazne mení mikroštruktúrnu austenitických nehrdzavejúcich ocelí prostredníctvom troch primárnych mechanizmov plastickej deformácie ako sú deformáciou indukovaný martenzit, deformačné dvojčatenie a sklz. Mikroštruktúrna odozva a uplatnenie mechanizmov závisí vo veľkej miere od zloženia ocele či podmienok deformácie. V rôznych štúdiách sa uvádzajú konzistentné kritické prahové hodnoty deformácie pre počiatočné uplatňovanie deformácie (8-15%), pre prudký nárast dislokácie a hustoty dvojčaťových hraníc (15-17%) a začiatok významnej tvorby martenzitu (20%) [5-7].

Tieto mikroštrukturálne zmeny sú základom pozorovaného spevňovania v austenitických oceliach po valcovaní, pričom zosilnenie v dôsledku deformácie je dominované zosilnením jemných zŕn z dislokačných buniek a klzných pásov, zatiaľ čo tvorba rozhraní γ/α' a deformačných dvojčiat vytvára miesta pre segregáciu vodíka a potenciálne krehnutie [8,9,10,11].

Je potrebné poznamenať, že vplyv valcovania za studena môže výrazne ovplyvniť mikroštruktúru. Vývoj deformačného martenzitu počas spracovania za studena môže výrazne zmeniť textúru deformácie a tak významne prispieť k zmene celkových vlastností polotovarov vyrobených z austenitických nehrdzavejúcich ocelí. V rámci tejto štúdie sa preto aplikovalo valcovanie za studena pri 3 rôznych podmienkach, pri ktorom sa sledovalo ako tieto podmienky vplývajú na mikroštruktúru. Cieľom výskumu je preskúmať vzťah medzi štruktúrnymi zmenami a spevnením metastabilných austenitických ocelí spracovaných valcovaním za studena, ktoré prispejú k objasneniu nasledujúcim štúdiám, vplyvu deformačných mechanizmov na scitlivenie austenitických nehrdzavejúcich ocelí a ako zmeny vplývajú na vlastností ocele.

2. Experimentálny materiál

Experimentálnym materiálom použitým pre objasnenie vplyvu podmienok deformácie bola austenitická nehrdzavejúca oceľ AISI 304L. Materiál bol valcovaný za tepla s následne aplikovaným rozpúšťacím žíhaním, dodaným vo forme plechu s hrúbkou 20 mm. Chemické zloženie austenitickej ocele AISI 304L je uvedené v Tab. 1.

Tab. 1 *Chemické zloženie AISI 304L (hmot. %)*

	C	***Mn***	***Si***	***Cr***	***Ni***	***Mo***	***S***	***P***	***Fe***
AISI 304L	*0,035*	*1,29*	*0,37*	*18,62*	*8,19*	*0,33*	*0,024*	*0,027*	*zv. 70,2*

Na zistenie vplyvu podmienok deformácie boli vyhotovené série stavov materiálu valcovaného za studena s redukciou hrúbky 20% pri rôznych teplotách. Aby bolo možné pozorovať zmeny mikroštruktúry hraníc zŕn na vzorkách po valcovaní, bolo potrebné pripraviť materiál štandardnými metalografickými technikami. Na zistenie kryštalografických orientácii povrchu vzoriek bola použitá difrakcia spätného rozptylu elektrónov (EBSD) na elektrónovom mikroskope Tescan LYRA 3. Merania objemového podielu feromagnetických fáz prebiehalo pomocou zariadenia Fisher Feritscope FMP30C.

3. Výsledky a diskusia

Mikroštruktúra referenčného materiálu austenitickej ocele bola tvorená polyedrickými zrnami austenitu. Pri statickej deformácii valcovaním za studena s redukciou 20% vzniká rovnomerná deformácia v celom objeme materiálu. V materiáli dochádza k natáčaniu hraníc zŕn a kumuluje sa plastická deformácia ktorá má typickú deformačnú textúru. Vzniká intenzívne zdeformovaná nerovnovážna štruktúra s veľmi vysokou dislokačnou hustotou. Rozdielne podmienky valcovania, najmä teplota a úroveň redukcie, identifikujú plastickú deformáciu pri vzniku rôznych deformačných mechanizmov: deformáciou indukovaný martenzit, deformačné dvojčatenie a sklz (Tab. 2).

Pri pozorovaní mikroštruktúry bola potvrdená prítomnosť feromagnetických fáz. Odmeraním objemového podielu je delta feritu je možné potvrdiť, že jeho hodnota je konštantná. V Tab. 2 sú zhrnuté hodnoty plošnej hustoty hraníc zŕn, vypočítané v programe Matlab s doplnkový nástrojom Mtex a výskyt alfa-martenzitu s delta-feritom [12].

Mikroštruktúra na všetkých vzorkách je polyedrická s rôznou veľkosťou zŕn. Všetky vzorky obsahovali žíhacie dvojčatá, ktoré sú typické pre austenitické zrno. Na spracovanie SEM fotografii a identifikáciu hraníc zŕn bol použitý program Matlab [12].

Tab.2 *Závislosť mikroštruktúrnych charakteristík od podmienok tvárnenia*

Vzorka	***Teplota pretvárnenia (°C)***	***Plošná hustota hraníc zŕn*** (mm^{-1})	***Dislokačná hustota***	***alpha+delta (Vol %)***	***Výskyt deformačných mechanizmov***
REF	**-**	***134,89***	***1,39±1,06x10***^{13}	***2,0***	**-**
1	*100*	*305,01*	*5,2±2,7x10*^{14}	*4,1*	*všetky*
2	*200*	*212,57*	*2,84±2,41x10*^{14}	*2,7*	*sklz, dvojčatenie*
3	*400*	*148,94*	*2,99±3,47x10*^{14}	*2,6*	*sklz*

Mapy orientácii zŕn z EBSD analýzy sa používajú na hodnotenie mechanizmov deformačného spevnenia. Každé zrno má inú kryštalografickú orientáciu čo zvýrazňujú aj rôzne farebné zobrazenie. Tieto farby zodpovedajú mape inverzného pólového obrazu (IPF), kde je orientácia kódovaná vzhľadom na špecifický smer vo vzorke. Všetky IPF mapy sú v smere valcovania.

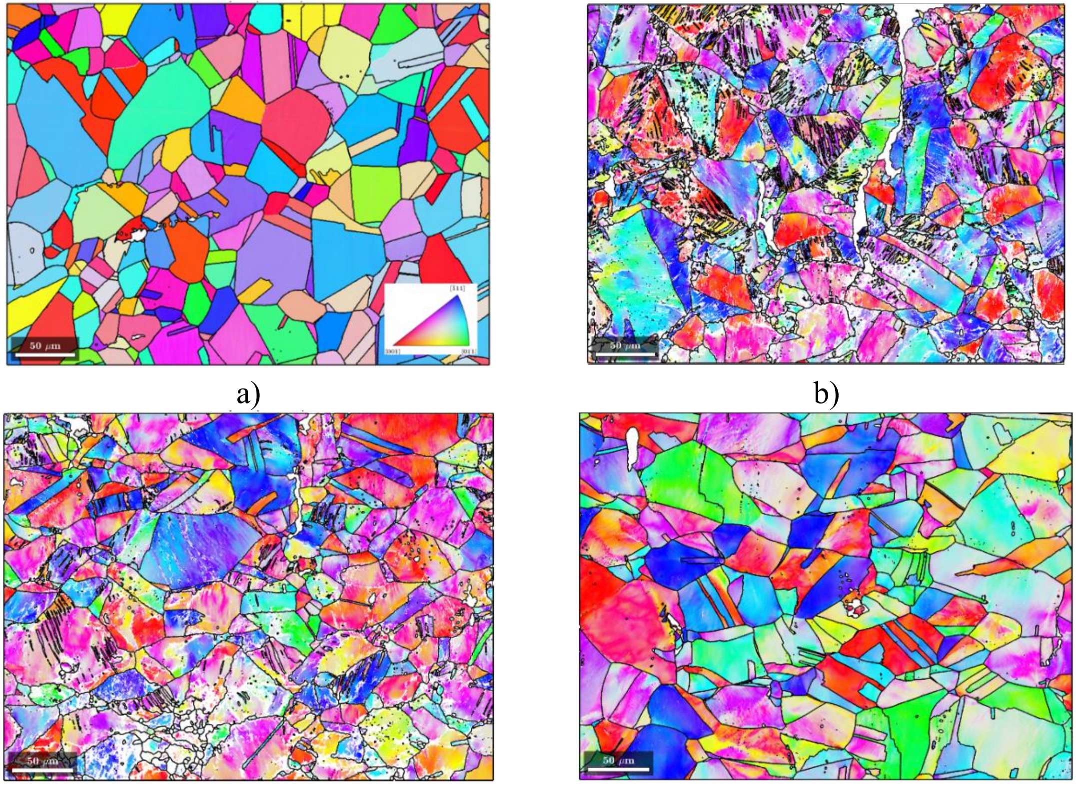

a) b)

c) d)

Obr. 1 *IPF mapy austenitickej ocele AISI 304L, a) referenčná vzorka ,b) vzorka 1 ,c) vzorka 2 , d) vzorka 3*

Mikroštruktúrne charakteristiky vzoriek AISI 304l sú znázornené na obr. 1 (a-d). Priemerná veľkosť zŕn z merania EBSD bola 40 μm. Mikroštruktúra referenčnej vzorky ukázala rovnoosé austenitické zrná. IPF mapy vzoriek po valcovaní za studena ukazujú rozloženie a množstvo hraníc zŕn a výskyt ďalších fáz, a ktorý z deformačných mechanizmov sa uplatňuje najčastejšie. Na valcovaných vzorkách sa v rámci jedného zrna vyskytujú rôzne odtiene čo hovorí o veľkom gradiente orientácie a teda potvrdzuje zvýšenú dislokačnú hustotu. Žíhacie dvojčatá sú vplyvom valcovania zdeformované. Časť bielych miest predstavuje výskyt feromagnetických fáz a teda deformáciou indukovaný martenzit spoločne s neurčenými hranicami zŕn. Na vzorke č. 1 vidieť veľké množstvo dvojčaťových hraníc a veľké množstvo zárodkov martenzitu [5]. Pri vyšších teplotách sa vo vzorke vyskytuje prevažne sklz [13].

V EBSD analýze sa hranice medzi zrnami klasifikujú na základe misorientácie medzi susednými zrnami. Táto misorientácia (uhlová disorientácia) sa vyjadruje v stupňoch a určuje ako sa líši orientácia kryštalických mriežok v dvoch susediacich zrnách. Na obr. 2(a-d) sú zvýraznené hranice zŕn, kde sú farebne odlíšené stupne misorientácie, ktoré vyjadruje farebný stĺpec napravo každej mikroštruktúry. Misorientácia sa posudzuje podľa hraníc zŕn s nízkym uhlom (LAGB) a vysokým uhlom misorientácie (HAGB). Špeciálne hranice zŕn sú často charakterizované modelom Coincidence Site Lattice (CSL). Mapy misorientácii zobrazujú takisto množstvo hraníc vzniknutých počas valcovania.

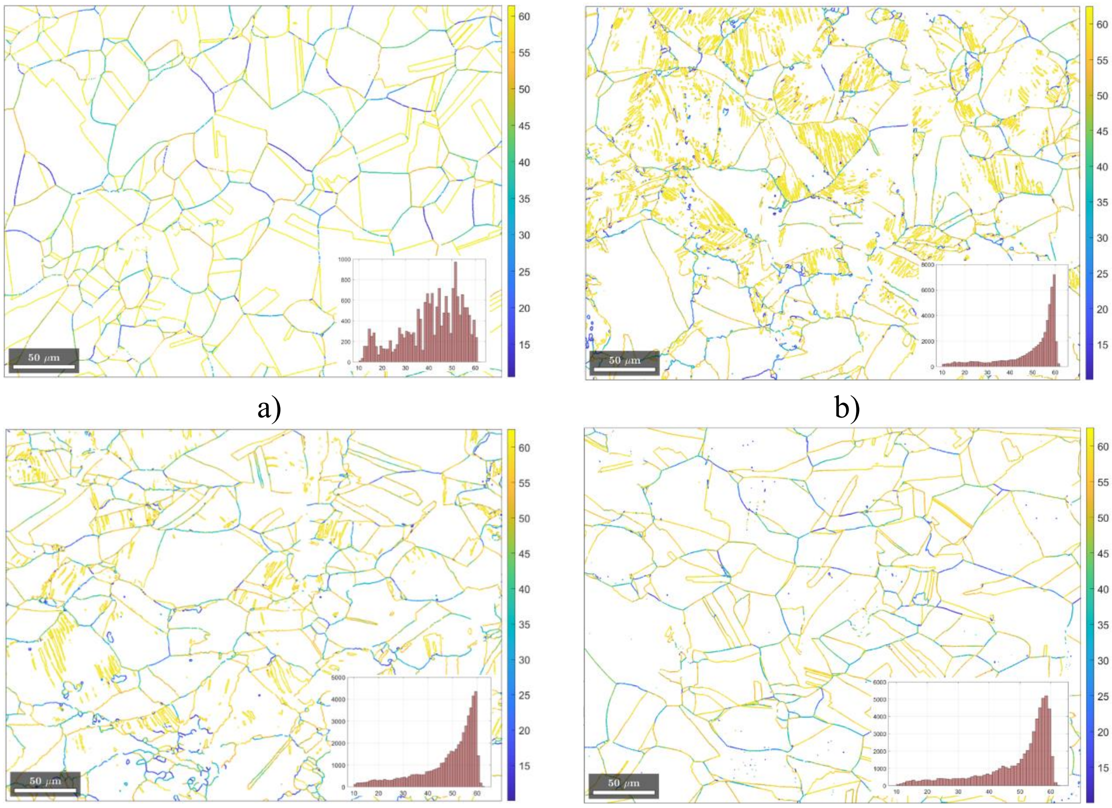

a) b) c) d)

Obr. 2 *Misorientácia zŕn na vzorkách AISI 304L, a) referenčná vzorka ,b) vzorka 1 ,c) vzorka 2 , d) vzorka 3*

Histogram nachádzajúci sa pri každej mikroštruktúre približuje výskyt konkrétnych hraníc zŕn, kde na y-ovej osi je uvedený počet hraníc zŕn a x-vá os predstavuje uhly misorientácie. Vysoká frekvencia misorientácie pri 60° naznačuje významný výskyt žíhacích dvojčat v referenčnej vzorke a takisto prítomnosť CSL3 hraníc, ktoré naznačujú prítomnosť deformačných dvojčat. Pri porovnaní na vzorke 1 a vzorke 2 je viditeľný pokles počtu hraníc s uhlom 60° čo je spôsobené zvýšením teploty pretvárnenia. Tento jav potvrdzuje aj údaj plošnej hustoty hraníc zŕn. Pri nízkej teplote deformácie sa výrazne aktivuje tvorba dvojčaťových hraníc. S rastúcou teplotou sa ich tvorba postupne potláča, čo vedie k mikroštruktúre zloženej prevažne z dislokácii a rekryštalizačných zŕn. Pri najvyššej teplote mechanické dvojčatenie nehrá významnú úlohu v deformačnom správaní materiálu [14].

Deformačné mechanizmy sú tvorené skrutkovými a hranovými dislokáciami. V závislosti od orientácie môžu mať dislokácie jednotlivé časti, kde časť môže byť skrutková a časť hranová.

4 Záver

V štúdii bol skúmaný vplyv podmienok valcovania na štruktúru austenitickej ocele AISI 304L pri rôznych teplotách pretvárnenia. Výsledky výskumu ukazujú, že pri nízkych teplotách pretvárnenia sa uplatňujú všetky mechanizmy, pri ktorých je generované veľké množstvo nových hraníc, vďaka ktorým sa materiál spevňuje. So zvyšujúcou teplotou klesá tvorba deformáciou indukovaného martenzitu. Pri najvyšších teplotách sa znížil vznik martenzitu a deformačných dvojčat a prevažuje výskyt slzu.

Poďakovanie

Výskum bol podporený Vedeckou grantovou agentúrou Ministerstva školstva SR a Slovenskej akadémie vied, projektom KEGA č.033ŽU-4/2026, VEGA 1/0461/24, VEGA 1/0729/26, APVV-23-0317 a projektom na podporu mladých vedeckých pracovníkov na UNIZA, ďalšie poďakovania patria projektu Erazmus+ a Grantovému projektu UNIZA.

Použitá literatúra

[1] FENG, Wen; YANG, Sen; YAN, Yinbiao. Dependence of grain boundary character distribution on the initial grain size of 304 austenitic stainless steel. *Philosophical Magazine*, 2017, 97.13: 1057-1070.

[2] SAHA, S., et al. Any effect of processing history on precipitation hardening of metastable austenitic stainless steels. *Key Engineering Materials*, 2012, 504: 851-856.

[3] STAUDHAMMER, K. P.; MURR, L. E.; HECKER, S. S. Nucleation and evolution of strain-induced martensitic (bcc) embryos and substructure in stainless steel: a transmission electron microscope study. *Acta Metallurgica*, 1983, 31.2: 267-274.

[4] SUN, Chao, et al. Revealing the Role of Pre-Strain on the Microstructure and Mechanical Properties of a High-Mn Austenitic Steel. *Crystals*, 2024, 14.12: 1054.

[5] KORZNIKOVA, Galia, et al. EBSD characterization of cryogenically rolled type 321 austenitic stainless steel. *Metallurgical and Materials Transactions A*, 2018, 49.12: 6325-6336.

[6] LEE, W.-S.; LIN, C.-F. Effects of prestrain and strain rate on dynamic deformation characteristics of 304L stainless steel: Part 1—Mechanical behaviour. *Materials science and technology*, 2002, 18.8: 869-876.

[7] LEE W-S, Lin C-F. Effects of prestrain and strain rate on dynamic deformation characteristics of 304L stainless steel: Part 2—Microstructural study. *Materials Science and Technology*. 2002;18(8):877-884.

[8] PARK, Il-Jeong, et al. The effect of pre-strain on the resistance to hydrogen embrittlement in 316L austenitic stainless steel. *Materials Transactions*, 2014, 55.6: 964-970.

[9] ORTOLLAND, Victor, et al. Experimental study of the hydrogen-microstructure interactions in a pre-strained 316L austenitic stainless steel. *International Journal of Hydrogen Energy*, 2024, 67: 577-591.

[10] WANG, Yanfei; WU, Xuanpei; WU, Weijie. Effect of α′ martensite content induced by tensile plastic prestrain on hydrogen transport and hydrogen embrittlement of 304L austenitic stainless steel. *Metals*, 2018, 8.9: 660.

[11] WANG, Yanfei, et al. Warm pre-strain: Strengthening the metasTable 304L austenitic stainless steel without compromising its hydrogen embrittlement resistance. *Materials*, 2017, 10.11: 1331.

[12] BACHMANN, Florian, Ralf Hielscher a Helmut Schaeben. *MTEX: Free Matlab* toolbox for Quantitative Texture Analysis. Verzia 5.11. Dostupné online na: https://mtex-toolbox.github.io/

[13] IK, Gopalakrishnan, et al. Cold rolled texture and microstructure in types 304 and 316L austenitic stainless steels. *ISIJ international*, 2003, 43.10: 1581-1589.

[14] SRINIVASAN, N.; KUMARAN, S. Senthil; VENKATESWARLU, D. Effects of in-grain misorientation developments in sensitization of 304 L austenitic stainless steels. *Materials Research Express*, 2018, 6.1: 016551.

29th International Seminar of Ph.D. Students

SEMDOK 2026

Western Tatras – Zuberec, Slovak Republic
February, 4 to February 6, 2026

QUENCHING OPTIMIZATION AND ITS EFFECT ON THE MICROSTRUCTURE OF HIGH-STRENGTH LOW-ALLOY STEELS

Edita Illichmanová[1*], Milan Uhríčik[1], Melisa Šnircová[1], Martin Slezák[1], Lenka Kucharíková[1]

[1] Department of Materials Engineering, Faculty of Mechanical Engineering, University of Žilina, Univerzitná 8215/1, 010 26 Žilina, Slovak Republic

**Corresponding author: edit.illichmanova@fstroj.uniza.sk, +421 41 513 2620, Department of Materials Engineering, Faculty of Mechanical Engineering, University of Žilina, Univerzitná 8215/1, 010 26 Žilina, Slovak Republic*

Abstract

This study evaluates the effect of selected heat treatment parameters on HSLA 38MnVS6 steel with the objective of obtaining a predominantly martensitic microstructure and achieving hardness in the range of 49 – 54 HRC across the sample cross-section. Three heat treatment modes were applied involving variations in carbon potential, quenching oil type, and oil temperature. Hardness was measured using the Rockwell method, and microstructures were analyzed by optical microscopy after Nital etching. The results confirmed that increased furnace carbon potential improved surface hardness by reducing ferrite formation, while the decisive factor for achieving the required core hardness was the viscosity and cooling capacity of the quenching oil. Lower oil temperature effectively suppressed the formation of undesirable fine lamellar pearlite (troostite).

Keywords: HSLA steels, 38MnVS6, austenitization, quenching

1. Introduction

High-strength low-alloy steels (HSLA) represent advanced structural materials characterized by a high yield strength at a relatively low carbon content. Their properties are achieved through microalloying with elements such as vanadium, niobium, or titanium, which promote precipitation strengthening and grain refinement. These characteristics make HSLA steels highly suitable for automotive components subjected to cyclic or impact loading.

The microstructure and properties of HSLA steels are significantly influenced by thermomechanical processing and subsequent heat treatment. Processes such as austenitization, quenching, and tempering are decisive for controlling transformation behavior and the phase distribution of ferrite, bainite, and martensite. Proper selection of these parameters enables the optimization of hardness, strength, and ductility, which are essential for components exposed to dynamic loading.

Steel grade 38MnVS6 is commonly used in the precipitation-hardened condition due to its good machinability and strength. Extending its application to the fully quenched condition requires detailed knowledge of the influence of heat treatment parameters on microstructure evolution. Therefore, this work focuses on the comparison and optimization of austenitization and quenching modes for this steel [1, 2].

2. Methodology of research

2.1 Experimental material

The investigated material was an HSLA steel, specifically 38MnVS6, standardized according to EN 10267:1998 *“Ferritic-pearlitic steels for precipitation hardening from hot-working temperatures”.* Cylindrical specimens with a diameter of 16 mm and a length of 50 mm were prepared for the experiments. Five specimens were processed for each heat treatment modes [3].

The chemical composition of the material, verified by emission spectrometry and compliant with the standard requirements, is presented in Tab. 1.

***Tab. 1** Chemical composition*

Steel	*Concentration of chemical elements [Wt%]*							
	C	*Si*	*Mn*	*P*	*S*	*Cr*	*V*	*N*
38MnVS6	*0.390*	*0.100*	*1.480*	*0.010*	*0.021*	*0.090*	*0.100*	*0.013*

2.2 Design of heat treatment

Heat treatment was carried out in a chamber furnace Aichelin VKES 4/1. The furnace is equipped with a protective endothermic gas atmosphere (endogas), consisting mainly of CO, H_2 , and N_2 , which prevents oxidation and surface decarburization of the material.

Mode 1 was designed based on theoretical considerations. Subsequent Modes 2 and 3 were gradually optimized based on the results of the preceding experiments.

Two different quenching oils were used as quenching media. Oil 1 is an isothermal quenching oil with an operating temperature range of 50 – 160 °C. Oil 2 is a fast-quenching oil with lower viscosity and higher cooling intensity, intended for temperatures between 50 – 80 °C [4, 5].

All heat treatment modes included low-temperature tempering at 200 °C for 70 minutes in order to reduce residual stresses without a significant loss of hardness.

2.3 Metallographic analysis

Samples for microstructural analysis were sectioned perpendicular to the axis of the cylindrical bars, mounted, ground, and polished using a Struers TegraPol-15 device. The surface was etched with 3% Nital for 5 seconds and subsequently examined using a Leica Dmi8 inverted optical microscope.

Hardness was measured by the Rockwell method according to STN EN ISO 6508-1 using a Struers DuraVision-30 hardness tester. The required hardness after heat treatment was defined in the range of 49 – 54 HRC. Measurements were performed on the surface (three indentations) and in the core (four indentations) of each specimen [6, 7, 8].

3. Results and discussion

The material in the initial condition exhibited a ferritic-pearlitic microstructure with elongated manganese sulfide inclusions oriented in the direction of prior forming. This condition corresponded to the standard delivery state of the steel.

3.1 Heat treatment Mode 1

The first heat treatment modes was designed based on theoretical knowledge with the aim of achieving complete transformation of the initial ferritic-pearlitic microstructure into homogeneous austenite while minimizing the risk of excessive austenitic grain growth. Mode 1 included austenitization at 870 °C for 80 minutes. The carbon potential of the furnace atmosphere was maintained at Cp = 0.39. Quenching was carried out in isothermal Oil 1 at a temperature of 120 °C, followed by tempering at 200 °C for 70 minutes. The hardness results after Mode 1 are summarized in Tab. 2, showing that the required hardness values were not achieved [9, 10].

Tab. 2 *Results of hardness tests for Mode 1*

Measurement location	***Method***	***Sample***				
		1	***2***	***3***	***4***	***5***
Surface	*HRC*	*46.7*	*48.1*	*47.5*	*47.8*	*45.9*
Core	*HRC*	*47.8*	*49.5*	*48.8*	*48.6*	*46.4*

The resulting microstructure was evaluated as martensitic–bainitic–pearlitic, with approximately 40% of fine lamellar pearlite (troostite) (Fig. 1). The high temperature of the quenching oil resulted in an insufficient cooling rate for complete martensitic transformation. Pronounced ferritic regions were observed on the surface, indicating partial surface decarburization.

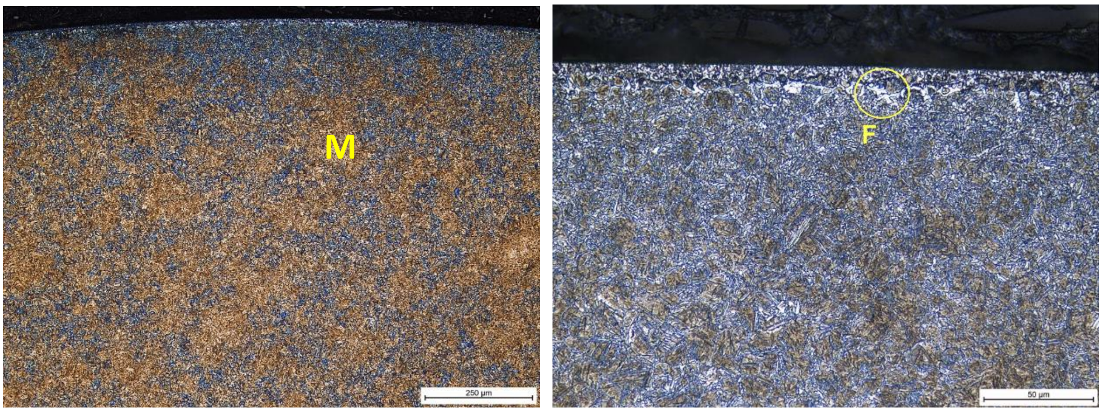

Fig. 1 *Microstructure of the surface of a 38MnVS6 steel sample, Mode 1, etched with 3% Nital*

3.2 Heat treatment Mode 2

Due to the insufficient surface hardness and the presence of ferrite, the carbon potential in Mode 2 was increased to Cp = 0.42. The oil temperature was reduced to 70 °C, while quenching was still performed in Oil 1.

Tab. 3 demonstrates that after Mode 2, the surface hardness increased significantly, confirming the beneficial effect of the higher carbon potential. However, the core hardness did not reach sufficient values.

Tab. 3 *Results of hardness tests for Mode 2*

Measurement location	***Method***	***Sample***				
		1	***2***	***3***	***4***	***5***
Surface	*HRC*	*49.5*	*50.2*	*49.7*	*51.1*	*50.6*
Core	*HRC*	*46.2*	*47.4*	*46.8*	*48.6*	*48.0*

The resulting microstructure was finer and more homogeneous, with a small fraction of troostite and a minimal amount of surface ferrite (Fig. 2). These findings indicated that further improvement required a change in the quenching medium.

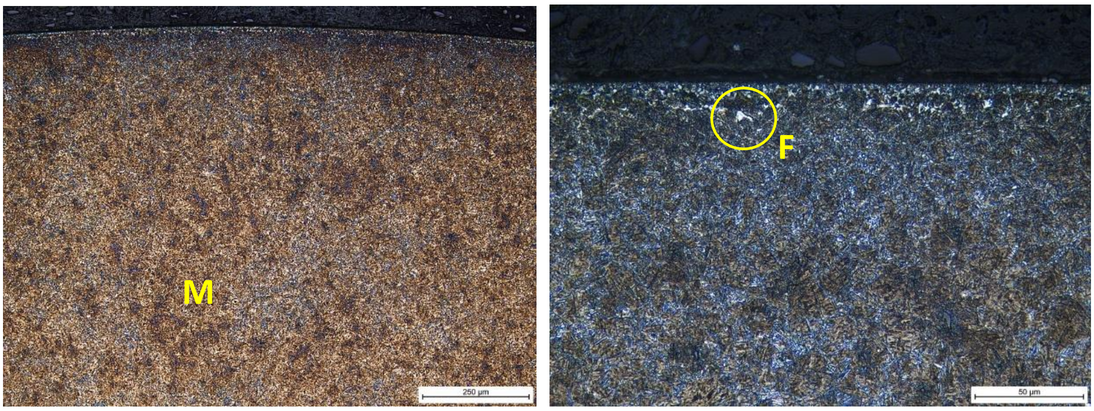

Fig. 2 *Microstructure of the surface of a 38MnVS6 steel sample, Mode 2, etched with 3% Nital*

3.3 Heat treatment Mode 3

In Mode 3, fast-quenching Oil 2 with lower viscosity was applied at a temperature of 70 °C. The remaining heat treatment parameters were kept unchanged.

This modification led to the achievement of the required properties. The surface and core hardness of all specimens fell within the favorable range of the required values, 49 – 54 HRC (Tab. 4).

Tab. 4 *Results of hardness tests for Mode 3*

Measurement location	***Method***	***Sample***				
		1	***2***	***3***	***4***	***5***
Surface	*HRC*	*53.1*	*52.9*	*53.0*	*53.5*	*52.7*
Core	*HRC*	*50.9*	*50.2*	*50.6*	*51.0*	*50.2*

The change to a quenching oil with a higher cooling rate was reflected in the microstructure by the formation of a predominantly martensitic structure with a smaller proportion of bainite and unevenly distributed islands of fine lamellar pearlitic structure (troostite). Surface decarburization, manifested by the presence of ferrite, was also minimal. The resulting microstructure is shown in Fig. 3. The results confirmed that the decisive factor is the viscosity and cooling capacity of the quenching oil, rather than its temperature alone.

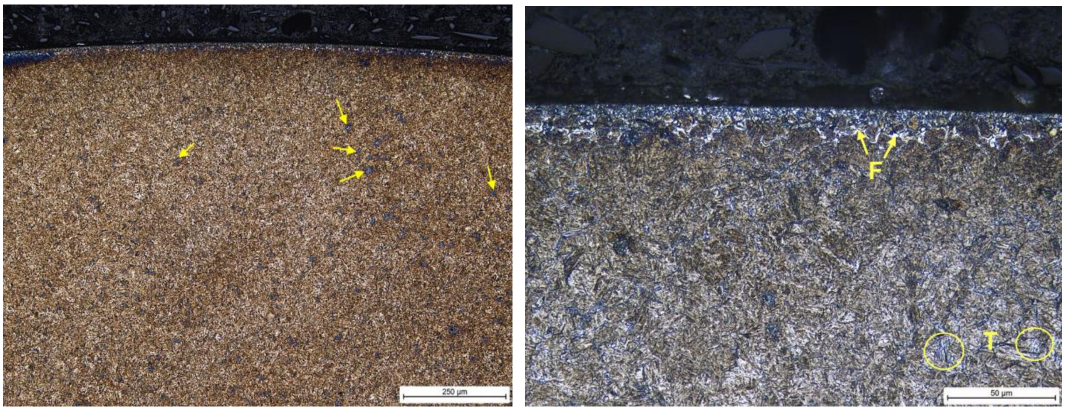

Fig. 3 *Microstructure of the surface of a 38MnVS6 steel sample, Mode 3, etched with 3% Nital*

4. Conclusion

The study focuses on the optimization of austenitization, hardening, and low-temperature tempering conditions of 38MnVS6 steel with the objective of achieving a predominantly martensitic microstructure and a hardness of 49 – 54 HRC on both the surface and in the core. Based on experimental evaluation of three heat treatment modes, including parameter optimization, hardness measurements, and microstructural analysis, the following conclusions can be drawn:

1. All heat treatment modes resulted in a martensitic–bainitic microstructure with a negligible amount of residual austenite and a variable share of fine lamellar pearlite (troostite) reaching up to approximately 40%.
2. Variations in quenching medium temperature showed no significant effect on hardness; however, the viscosity of the quenching oil was identified as the decisive factor. The use of a high-performance, low-viscosity quenching oil enabled the formation of a predominantly martensitic structure without inducing deformations or cracks.
3. Heat treatment Mode 3 achieved satisfactory hardness values, with minimum measured values of 52.7 HRC on the surface and 50.2 HRC in the core, fully meeting the required hardness range.
4. The results confirm that HSLA steel 38MnVS6 represents a suitable alternative to conventional carbon structural steels for automotive and engineering applications, particularly for hardening in chamber furnaces.

Acknowledgment

The research was supported by the Ministry of Education, Research, Development and Youth of the Slovak Republic supported the research by projects VEGA no. 1/0461/24, VEGA 1/0729/26, and KEGA no. 033ŽU-4/2026.

References

[1] Zhao, S., Chen, K., Wuqikun, Y., Chen, X., Wang, Z.: *Effect of heat treatment on microstructure and mechanical propesrties of high strength low alloy (HSLA) steel.* In: Research and Application of Materials Science. Vol. 5, No. 3, pp. 45–53. DOI: 10.33142/msra.v1i2.1666, 2019.

[2] www.textronsteelalloys.com/38mnvs6-round-bars-1-1303 available on-line 15.9.2025.

[3] www.steelnumber.com/en/steel_composition_eu.php?name_id=1916, available on-line 18.3.2025.

[4] Liščić, B., Tensi, H. M., Canale, L. C. F., Totten, G. E.: *Quenching Theory and Technology, 2nd edition*. Boca Raton: Taylor & Francis Group LLC. DOI: 10.1201/9781420009163, 2010..

[5] www.tegs.sk/produkty/kaliace-media/, available on-line 5.10.2025.

[6] STN EN ISO 6508-1: 2023. *Metallic materials. Rockwell hardness test. Part 1: Test method*.

[7] Dowling, N. E., 2013. Mechanical behavior of materials: engineering methods for deformation, fracture, and fatigue. ISBN 978-0-13-139506-0.

[8] www.affri.com/category/hardness-tests-theory-en/, available on-line 2.10.2025.

[9] www.aichelin.at/produkte/chargenanlagen/kammerofen available on-line 10.11.2025.

[10] Erçayhan, Y., Saklakoğlu, N.: The effect of thermomechanical process on metallurgical and mechanical properties of 38MnVS6 micro alloyed steel. In: *Materialwissenschaft und Werkstofftechnik*. Vol. 52 No. 6, pp. 644–654. DOI: 10.1002/mawe.202000235, 2021.

29th International Seminar of Ph.D. Students

SEMDOK 2026

Western Tatras – Zuberec, Slovak Republic
February, 4 to February 6, 2026

ARTIFICIAL NEURAL NETWORK BASED ESTIMATION OF WEAR TRACE WIDTH IN HARD-FACED STRUCTURAL COMPONENTS

Djordje Ivković[1], Dušan Arsić[1], Vukić Lazić[1], Ružica Nikolić[2*],
Jana Pastorková[2], Otakar Bokuvka[2], Martin Vicen[3]
[1]Faculty of Engineering, University of Kragujevac, Kragujevac, Serbia
[2] Research Centre, University of Žilina, Žilina, Slovakia
[3] Faculty of Mechanical Engineering, University of Žilina, Žilina, Slovakia
**Corresponding author: ruzica.nikolic@uniza.sk, tel. +421948610520, University of Žilina, Univerzitna 8215/1, 010 26 Žilina, Slovakia*

Abstract: In this paper is presented a study aimed at developing a predictive model for estimating the wear trace width of hard-faced and base metal samples based on their chemical composition. The research motivation arises from the need to establish a correlation between the alloying elements and tribological performance, thereby enabling early-stage evaluation of material behavior without extensive experimental testing. The dataset was formed using characteristic experimental cases obtained from block-on-disk tribological tests. The wear trace width values were measured after experimental tests, while the chemical composition data were taken from material specifications. A feed-forward ANN with Bayesian regularization was implemented in MATLAB. The proposed model demonstrated low agreement between predicted and experimental values due to small number of training data-sets.

1. Introduction

Components of construction and mining machinery are frequently exposed to severe abrasive and combined wear mechanisms, leading to rapid degradation and reduced service life. Typical examples include bucket teeth, mixer paddles, and levelling blades, operating under intensive contact with mineral aggregates (***Fig. 1***). Replacement of worn components is associated with high costs and long delivery times, making repair and production hard-facing technologies an economically justified solution. Hard-facing enables deposition of wear-resistant layers onto the new or worn components, using appropriate filler materials and welding procedures. The tribological behavior of hard-faced layers depends on a complex interaction between chemical composition, microstructure, hardness, and applied technology. Consequently, the laboratory tribological testing is widely used for preliminary evaluation and ranking of hard-facing systems. The aim of this research was to implement Artificial Neural Networks (ANN), since they have been increasingly applied in materials engineering for modelling nonlinear relationships between input parameters and material properties. When properly implemented, the ANN models can significantly reduce experimental effort by enabling early-stage prediction of material behavior. The objective of this study was to develop an ANN model for estimating wear trace width of hard-faced systems under defined tribological conditions and to validate the obtained predictions using the real exploitation data.

Fig. 1 Display of some damaged structural components

2. Experimental background and data sources

The training data consisted of chemical compositions of commonly used base and filler materials and data collected from experimental block-on-disk tribological tests performed under the same conditions on the same base and filler materials (***Fig. 2***) [1-2]. All the tests were conducted at a sliding speed of 1 m/s, normal load of 300 N, and duration of 60 min, using lubricated contact. Results for two base materials and three common applied filler materials were used

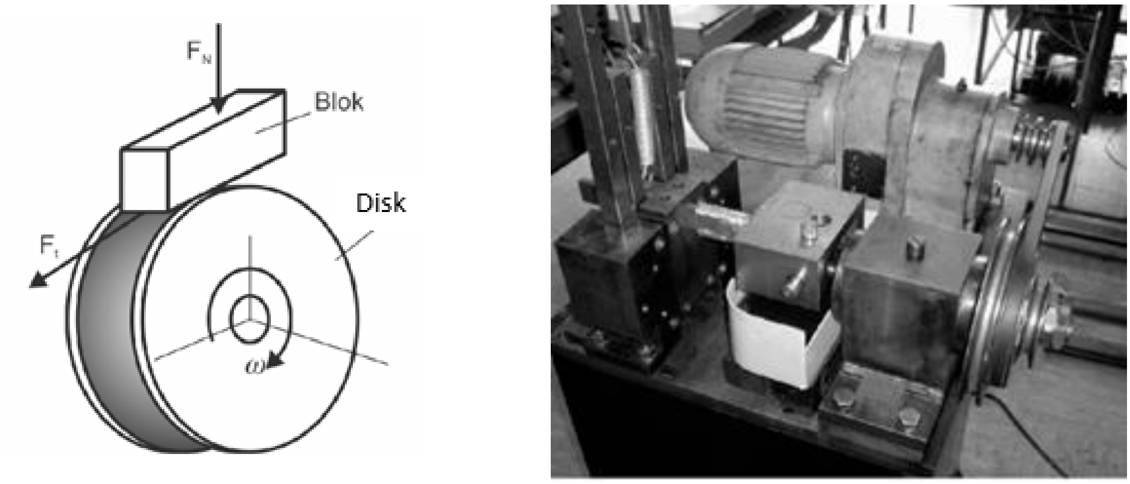

(a) **(b)**

Fig. 2 *Schematic display of block on disk contact (a) and device used for investigation (b)*

For the data prediction an ANN model was designed. Material's mass fractions were used as the input data and hard-facing configuration to the resulting wear trace width. A feed-forward neural network with one hidden layer was implemented using the Bayesian regularization to ensure the stable convergence and prevent overfitting due to the limited dataset size. Architecture of the ANN is shown in ***Fig. 3***. and network parameters are presented in ***Tab. 1***.

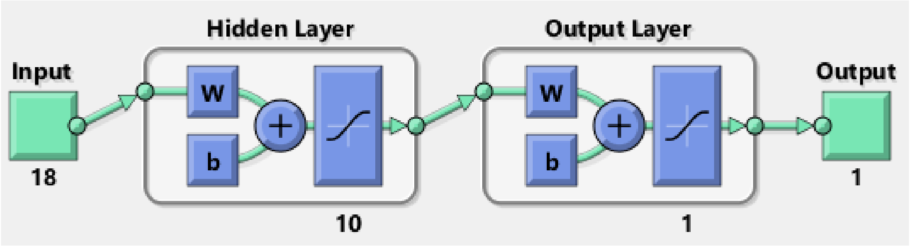

Fig. 3 *Architecture of the built ANN*

Tab. 1 *Main and training parameters of prepared ANN*

Parameter	***Description***
Network type	*Feed-forward backpropagation*
Training algorithm	*Bayesian regularization*
Learning function	*learngdm (gradient decent momentum)*
Inputt parameters	*18 chemical elements*
Output parameters	*Wear treck width, mm*
Number of hidden layers	*1*
Number of neurons	*10*
Activation functions	*Hidden layer: tansig, Output layer: tansig*
Training/ validation/ test ratio	*70/15/15%*
Momentum	*0.005*
Evaluation metrics	*R*

3. Results and Discussion

Despite the intensive work on optimization of the constructed ANN, and varying training parameters the built network did not successfully capture the complex and nonlinear relationship between the chemical composition, and wear trace width obtained under controlled tribological conditions. The regression analysis between the experimentally obtained and ANN-predicted values demonstrated a low level of agreement and lack of the model's capability to generalize the material behavior due to limited size of the dataset. The regression (R) values are shown in ***Fig. 4***. In all four cases, the R values were below 0.8, (approximately 0.6), which is insufficient for a network to provide the good prediction of wear trace width. Similar models of ANN were built earlier and they have provided good precision of ANN prediction [3-4], so the future work should include additional input parameters to improve the ANN's precision.

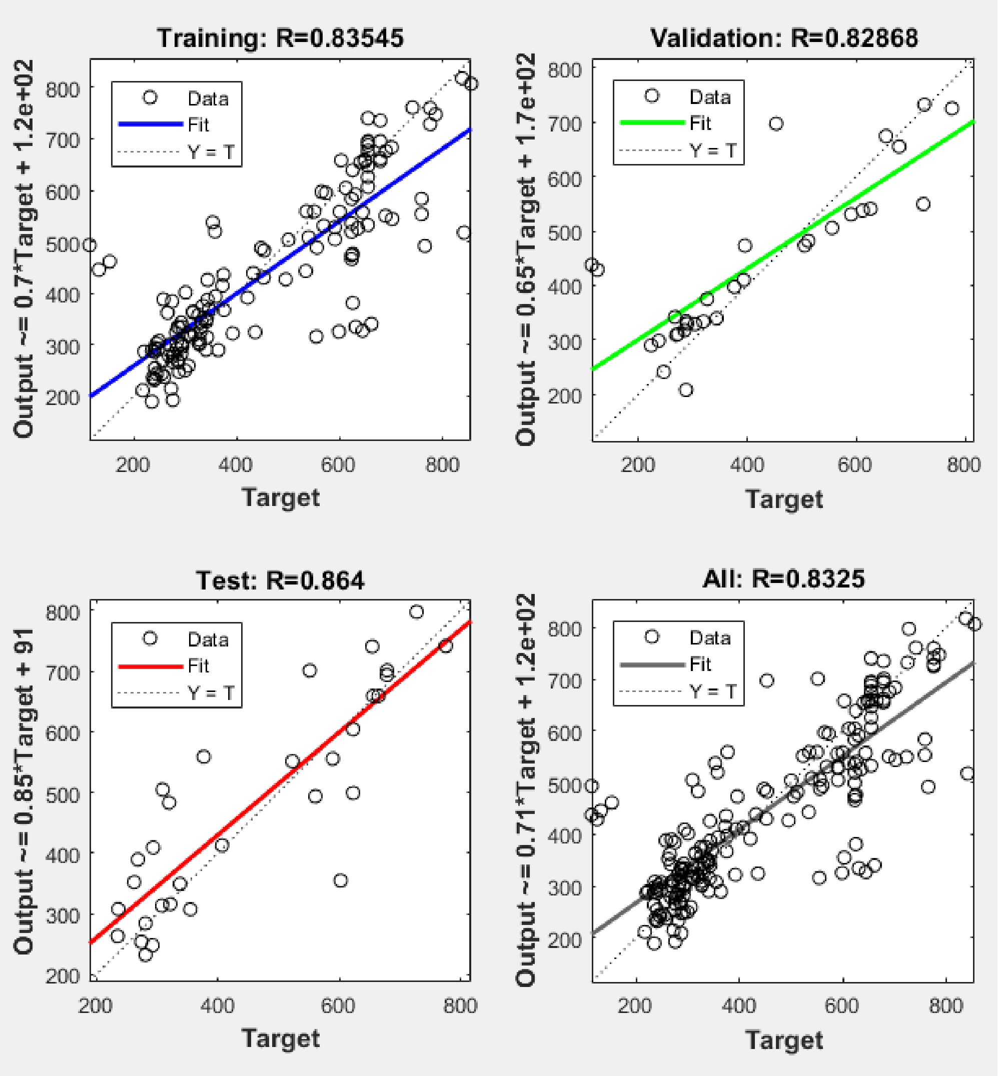

Fig. 4 *Display of R values obtained through ANN training*

4. Conclusions

The wear trace width obtained from the block-on-disk tribological tests represents a useful comparative parameter for evaluating the abrasive wear resistance of the base and hard-faced materials, under controlled laboratory conditions. In this study, an artificial neural network was developed with the aim of estimating the wear trace width based solely on the chemical composition of base and filler materials.

The implemented feed-forward ANN with Bayesian regularization demonstrated limited predictive capability, as indicated by relatively low regression coefficients between the predicted and experimentally obtained values. The obtained results suggest that chemical composition alone is insufficient to fully describe the complex wear mechanisms governing the wear trace formation in hard-faced systems, particularly when the available dataset is small.

Nevertheless, the study confirms the feasibility of applying ANN-based approaches in tribological investigations and highlights their potential as supportive tools for preliminary material assessment. The results clearly indicate that the additional input parameters, such as hardness, microstructural characteristics, layer configuration, and other variables, are required to improve the model's accuracy and generalization capability.

The future research should therefore focus on expanding the experimental database and incorporating microstructural and mechanical properties into the ANN input space. Such an approach is expected to significantly enhance the prediction reliability and contribute to development of more robust data-driven models for wear resistance evaluation of hard-faced structural components.

Acknowledgement

The research, results of which are presented here, was partially financially supported withing the project "Support of research and development capacities to generate advanced software tools designed to increase the resilience of economic entities against excessive volatility of the energy commodity market", of Operational Programme Integrated Infrastructure, number ITMS2014+ code 313011BUK9, co-funded by the European Regional Development Fund, by the Faculty of Engineering, University of Kragujevac, Serbia through funds provided by the Ministry of Science of the Republic of Serbia for project TR35024 and the project APVV SK-PL-25-0007.

References

[1] Lazić, V., Mutavdžić, M., Nikolić, R., Aleksandrović, S., Milosavljević, D., Krstić, B., Čukić, R.: Influence of various types of rock aggregates on selection of the working parts material in civil engineering, proceedings of The 13th International conference on tribology, SERBIATRIB '2013, Kragujevac, 2013, 15 – 17 May, pp. 275-280.

[2] Arsić, D., Lazić, V., Mutavdžić, M., Nikolić, R., Aleksandrović, S., Mitrović, S., Djordjević, M.: Experimental investigation of wear resistance of models hard faced with various filler metals, Proceedings of The 14th International conference on tribology - SERBIATRIB '15, Belgrade, Serbia, 2015, 13 – 15 May, pp. 170-175.

[3] Ivković, Dj., Arsić, D., Adamović, D., Nikolić, R., Mitrović, A., Bokuvka, O.: Predicting the mechanical properties of stainless steels using Artificial Neural Networks, Production Engineering Archives, Vol. 30, No.2, pp. 225-232.

[4] Ivković, Dj., Arsić, D., Adamović, D., Sedmak, A., Mandić, V., Delić, M., Mitrović, A.: A new artificial neural network model for predicting fatigue limit and fracture toughness values of some stainless steels, Proceedings of The 24th European Conference on Fracture - ECF24, Zagreb, Croatia, 2024, 26-30 August, p. 62.

ELECTROLYSIS – A METHOD FOR RUST REMOVAL FROM CORRODED OBJECTS

Justyna Janoszka[1], **Daniel Pakuła**[2], **Marcin Staszuk**[2],
[1] *Student of Silesian University of Technology, Faculty of Mechanical Engineering, Gliwice, Poland*
email: jj307256@student.polsl.pl
[2] *Professor of Silesian University of Technology, Faculty of Mechanical Engineering, Department of Engineering Materials and Biomaterials, Gliwice, Poland*
email: daniel.pakula@polsl.pl; marcin.staszuk@polsl.pl

1. Introduction

Among their interests, the passion for collecting objects such as coins, postage stamps, candlesticks, spoons, and national souvenirs is linked to the need to halt destructive processes and ensure protection. The corrosion process, a natural consequence of the laws of nature - metal tends to oxidize, which is mine ore - causes the destruction of metal objects. Therefore, the conservator's goal is to understand the process of deterioration, eliminate its effects, and protect against further deterioration [1].

The corrosion process depends on external factors, such as the type and composition of the environment, temperature, atmospheric pressure, and external polarity, as well as internal factors, such as the type of metal, its chemical composition, structure and surface condition, heat treatment, mechanical treatment, and residual stresses. Corrosion damage can be general or local. Destruction mechanisms include chemical corrosion, electrochemical corrosion, and corrosion-erosion [2, 3, 4].

The most difficult yet effective method for removing corrosion products from steel objects is the electrolytic method. This method allows for rust removal without damaging the underlying substrate. The electrolyte can be a concentrated sodium gluconate solution ($NaC_6H_{11}O_7$) at 80°C, a sodium bicarbonate solution ($NaHCO_3$), sodium carbonate (Na_2CO_3), or a sodium hydroxide solution (NaOH). The anode can be a piece of steel, graphite, or carbon rod, while the cathode is the object being derusted. Current from an external power source flows through the electrolyte, which is conductive due to the presence of sodium ions (Na^+) and carbon ions (CO_3^{2-}). Electrons are supplied from the power source, and the rust is separated from the object [1, 5, 6, 7]. The authors of study [8] subjected corroded samples to electrolysis using voltages of 10V, 15V, and 20V. A 0.78% sodium bicarbonate solution was used, and the derusting process lasted 5 hours. The mass loss at 10V was 0.15g, at 15V it was 0.16g, and at 20V it was 0.155g. XRD analysis of the corroded samples identified iron, magnetite, and wustite phases. The samples subjected to the process showed slight phase changes. The applied voltage affects the electrolysis process, and further studies are recommended [8].

2. Materials and methodology

The derusted objects are are Soviet AM-A and AM-B fuses, which were used during World War II in aerial bombs weighing up to 50 kg and in RS-82 and RS-132 rockets. The fuses consist of: arming vanes attached to a basket, aluminum foil covering the open end (preventing activation by air pressure after arming), a long firing pin attached to a thin metal (or plastic) disc, and a trigger mechanism [9].

The fuses used are completely safe. They do not contain hazardous or prohibited materials, and are therefore not subject to the Weapons and Ammunition Act. They were selected for electrolysis, which was intended to remove corrosion products. The fuses were cleaned of soil, degreased in acetone, and dried to prepare them for electrolysis.

The electrolysis process was carried out using a Unitra Unima 5351M power supply with an output voltage of 0-10V and an output current of 0-10A. Two groups of electrolytes were used: a 5% sodium bicarbonate solution (NaHCO3) and a 5% sodium hydroxide solution (NaOH). The rust removal process took place at a temperature of 20°C. The voltage and current parameters used during electrolysis are presented in Tab. 1.

Tab. 1 *Electrolytic process parameters*

Parameter V-A	*Electrolyte*	*Temperature [°C]*	*Electrode material*	*Time [h]*
9V3A	*5% $NaHCO_3$*	*20*	*Cathode: corrosion-affected object connected by a copper wire to the (-) power source* *Anode: stainless steel woven mesh connected by a copper wire to the (+) power source*	*1, 2, 3, 4, 5, 6*
9V3A	*5% NaOH*			

The loss of corrosion products was measured using the gravimetric analysis method with a Steinberg SBS-LW-200N analytical balance with an accuracy of 0.001 g. Measurements were taken after cleaning the samples and subsequently after 1, 2, 3, 4, 5, and 6 hours of electrolysis. For microscopic examinations, a Zeiss Supra 35 scanning electron microscope (SEM) was used at an accelerating voltage of EHT = 15 kV with a secondary electron (SE) detector. Additionally, a chemical composition analysis of the surface was performed using energy-dispersive spectroscopy (EDS).

3. Results

During the electrolysis process using 5% NaHCO3 and 5% NaOH solutions, the loss of corrosion products increased with each hour of the process. After 6 hours of the process, the lowest corrosion loss was recorded for the 9V3A parameter in the 5% NaHCO3 electrolyte, which was 5.29%. The highest rust loss was 9.07% for the 9V3A parameter in the 5% NaOH electrolyte. The mass loss is shown in Tab. 2 and the percentage graph in Fig. 1.

A comparison of objects cleaned in a 5% NaOH solution at a cleaning parameter of 9V3A is presented in Fig. 2. Before electrolysis, the corrosion products on the surface were light orange and light brown, which may indicate the presence of rust phase components such as orthorhombic lepidocrocite, goethite, and akagenite. After the first hour of the process, 1.19% of the rust was removed, revealing a black surface, which may indicate the presence of magnetite or wustite closest to the surface of the object. The surfaces closest to the anode were derusted first. The areas where no light orange rust was detected were the areas between the arming vane and the armin vane cup.

Tab. 2 *Mass loss*

Parameter V-A	Electrolyte	Before [g]	1h [g]	2h [g]	3h [g]	4h [g]	5h [g]	6h [g]
9V 3A	5% $NaHCO_3$	100,932	100,367	99,491	98,548	96,840	96,110	95,592
9V 3A	5% NaOH	106,082	104,812	102,156	100,550	99,133	97,733	96,463

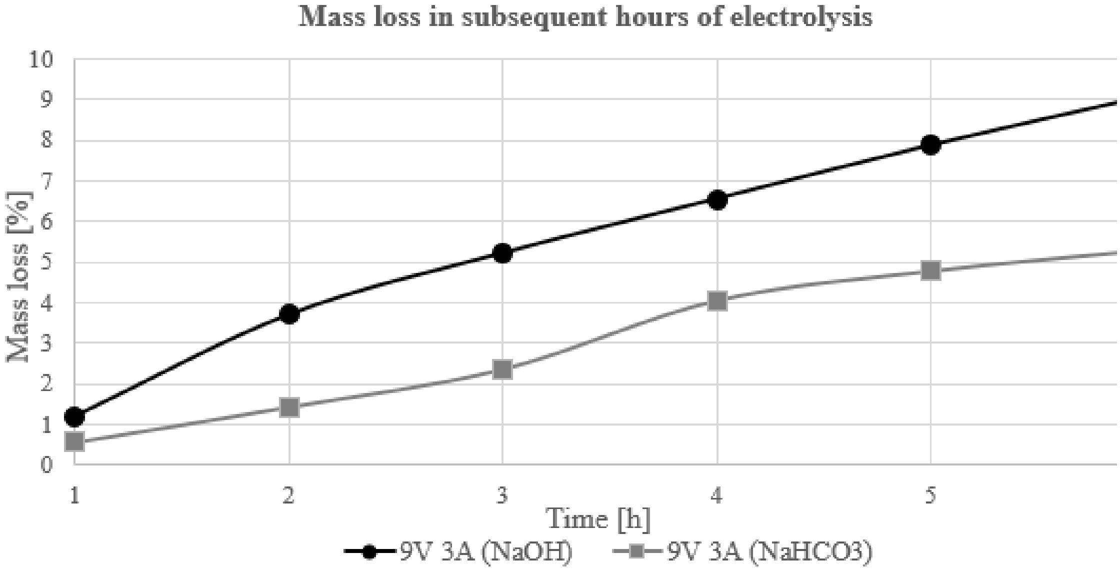

Fig. 1 *Graph of the percentage mass loss*

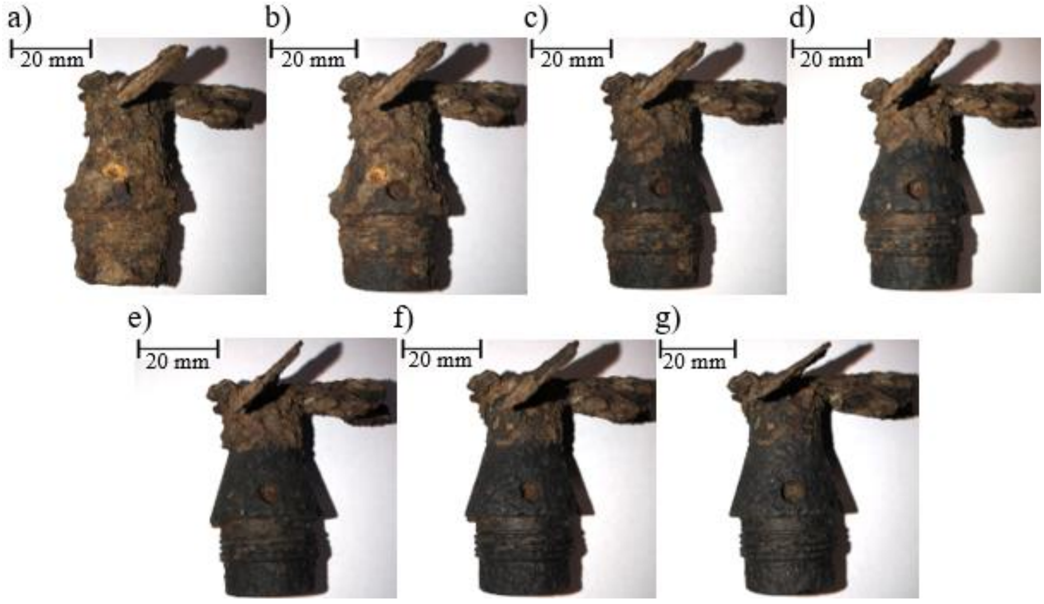

Fig. 2 *Comparison of the 9V3A rust removal parameter in NaOH electrolyte for the following time periods: a) input state, b) 1h, c) 2h, d) 3h, e) 4h, f) 5h, g) 6h*

on SEM microscopic analyses, an uneven surface topography was observed. Layered crystalline structures with a hexagonal shape, which may indicate the presence of a phase component in the form of hematite, were noticed on (Fig. 3a). EDS spectroscopy confirmed the presence of corrosion products for the NaOH electrolyte (Fig. 3b). The presence of the noble metal in EDS analysis results from the preparation of the samples for SEM examination by sputtering a thin layer of gold to ensure electrical discharge.

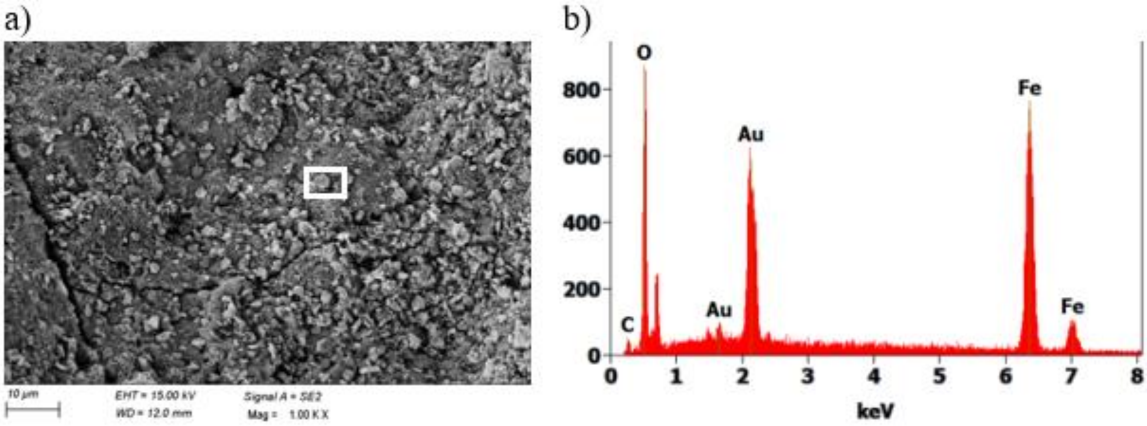

Fig. 3 Image: a) SEM of the topography of the surface derusted with NaOH electrolyte, b) EDS analysis of the area marked with a white square

3. Conclusions

Based on the conducted research, it has been determined that:

- Increasing the voltage-current parameter increases the loss of corrosion products. For the NaHCO3 electrolyte, the percentage weight loss was 5.29%, and for the NaOH electrolyte, 9.07%.
- The surface of the object derusted in the NaOH electrolyte was black. The topography was characterized by an uneven surface and the presence of corrosion products. SEM studies revealed hexagonal particles present on the object electrolyzed in sodium hydroxide solution, which may indicate the presence of hematite.

Acknowledgment

This work was carried out as part of an engineering project by Justyna Janoszka at the Faculty of Mechanical Engineering, Silesian University of Technology in Gliwice, under the supervision of Dr hab. Eng. Marcin Staszuk, Assoc. Prof. Silesian University of Technology.

References

[1] A. i. S. Sękowscy, Chemia dla kolekcjonera amatora, Nasza Księgarnia (Biblioteka Młodego Technika), Warszawa, 1989. (In Polish)

[2] J. Adamczyk, Inżynieria materiałów metalowych. Cz. 2, Wydawnictwo Politechniki Śląskiej, Gliwice, 2004. (In Polish)

[3] B. Mazurkiewicz, K. Moskwa U. Lelek-Borkowska, M. Bisztyga, Z. Szklarz , Korozja, 2015, https://www.chemia.odlew.agh.edu.pl/dydaktyka/Dokumenty/ChO_ IMiR/korozja_teoria.pdf., (available on-line: 02.12.2025). (In Polish)

[4] Z. Grzesik, Systematyka procesów korozyjnych, 2019, https://home.agh.edu.pl/~grzesik/Korozja_S/1_Systematyka%20procesów%20korozyjnych.pdf, (available on-line: 02.12.2025). (In Polish)

[5] S. Hochstettler, B. Tindall, Rust Removal Using Electrolysis, https://www.rickswood shopcreations.com/miscellaneous/rust_removal.htm, (available on-line: 16.12.2025).

[6] Magazyn Produkcja, Jak skutecznie odrdzewiać stal metodą elektrolizy: odrdzewianie elektrolityczne krok po kroku, 2023, https://magazyn-produkcja.pl/jak-skutecznie odrdzewiac-stal-metoda-elektrolizy-odrdzewianie-elektrolityczne-krok-po-kroku/, (available on-line: 16.12.2025). (In Polish)

[7] Muzeum Broni Strzeleckiej II Wojny Światowej, Niepubliczny Dom Kultury Fundacji EKSPONAT, ELEKTROLIZA - proces stosowany w Muzeum Broni Strzeleckiej II Wojny Światowej, unpublished material, 2025. (In Polish)

[8] S. A. A. Fuzi, H. Hussin, I. Izuddin, S. H. Ilias, N. R. Hamizun, Preliminary study on the effectiveness of the electrolysis process at different voltage for steel artifact conservation, AIP Conference Proceedings, 2925, 020004, 2024, https://doi.org/10.1063/5.0184381.

[9] M. Hiske, USSR – bombs and fuzes, http://michaelhiske.de/Allierte/USA/TManual/9_1985_7/Zünder/Fig_001.HTM, (available on-line: 20.12.2025).

29th International Seminar of Ph.D. Students
SEMDOK 2026
Western Tatras – Zuberec, Slovak Republic
February, 4 to February 6, 2026

EFFECTIVENESS OF IMPLEMENTATION OF MAIN PROCESSES IN THE CONDITIONS OF INFRASTRUCTURE IMPACT RISK – THE IMPORTANCE OF MAINTENANCE SUPERVISION IN A PRODUCTION ORGANIZATION

Agnieszka Jarecka[1*], Marek Roszak[2],
[1] ORLEN S.A., Warszawa, Polska
[2] Department of Engineering Materials and Biomaterials, Faculty of Mechanical Engineering, Silesian University of Technology, Gliwice, Poland, marek.roszak@polsl.pl
** agnieszka.jarecka@orlen.pl ul.Bielańska 12, 00-085 Warszawa*

1. Introduction

Organisations with a high level of invested capital operate in process systems where material and energy flows are interlinked, and infrastructural disruptions are systemic and non-linear, requiring adequate quality of maintenance supervision over the infrastructure they operate. Management standards particularly emphasise on this matter. The ISO 9001:2015 standard requires the implementation of risk-based thinking in process planning as well as the provision of infrastructure resources as a condition of process capability. Meanwhile, the updated ISO 55000:2024 standard explicitly introduces the perspective of asset management system performance (including assurance, adaptability, sustainability), maturity and ‘line of sight’ between organisational objectives and assets. In this approach, maintenance is not merely a technical function, but rather a component of asset governance and quality management system, jointly determining the predictability of core process execution [3,4,6]. Technical and organisational documentation has shown that the transition from reactive to planned and predictive (RCM/CBM) infrastructure maintenance reduces the frequency and severity of downtimes, shortens recovery times and stabilises process flows. The parallel development of integrated optimisation of production, maintenance and quality demonstrates that managing these domains separately within an organisation increases the predictability of plan execution [2, 4, 6].

2. Theoretical Foundations

The conceptual basis of this study is the integration of three perspectives:

1. A process-based approach and risk-based thinking grounded in the requirements of the ISO 9001 standard, which treats infrastructure as a resource determining product compliance and process effectiveness.
2. Asset governance based on the requirements of the ISO 55000:2024 standard, which demands linking asset related decisions to organisational objectives, lifecycle value management and the development of asset management system maturity.
3. The achievements of RCM/CBM practices and literature on manufacturing resilience, which indicate that measurable resilience loops (downtime, restart time, cascade range) determine the ability to maintain or quickly restore operational capabilities after a disruption [4, 6].

Based on the above three theoretical and normative perspectives, five interrelated categories of maintenance supervision were derived, as shown in Figure 1, which serve as the operational structure of the proposed model. The Maintenance Governance Framework for Core Process Effectiveness (MGF) was designed as a synthetic link between two approaches: process-based (ISO 9001) and asset-based (ISO 55000). Its first component – identification of infrastructure criticality in relation to value streams – corresponds to the principles of alignment and line of sight in accordance with the requirements of ISO 55000, which requires that decisions regarding assets be consistent with organisational objectives and visible 'downwards' to the asset level and 'upwards' to the system outcomes. In terms of quality, this also represents the implementation of the requirements of the ISO 9001 standard regarding the provision of resources for processes.

The second component – managing downtime risk in the asset life cycle – corresponds to RBM/RCM as well as the current approach outlined in the ISO 9001 standard, which introduces planned addressing of risks and opportunities as a part of QMS planning. In terms of methodology, this involves the optimisation of maintenance policies and CBM based on condition monitoring and degradation forecasting.

The third component – planning integration – is based on the trend of 'joint optimisation', which combines production, maintenance and quality into a unified objective function and consistent resource constraints.

The fourth component – data supervision – aligns MGF with maintenance maturity models, in which information quality and KPI consistency are key to decision predictability. It is also a practical translation of the requirements of the ISO 55000:2024 standard regarding system maturity and outcomes.

The fifth component – resilience loops – positions MGF within the resilient manufacturing literature, where shortening the time from disruption to stable operation requires standards for degradation, decoupling and restart, as well as strategies for limiting cascading effects [1, 6, 7].

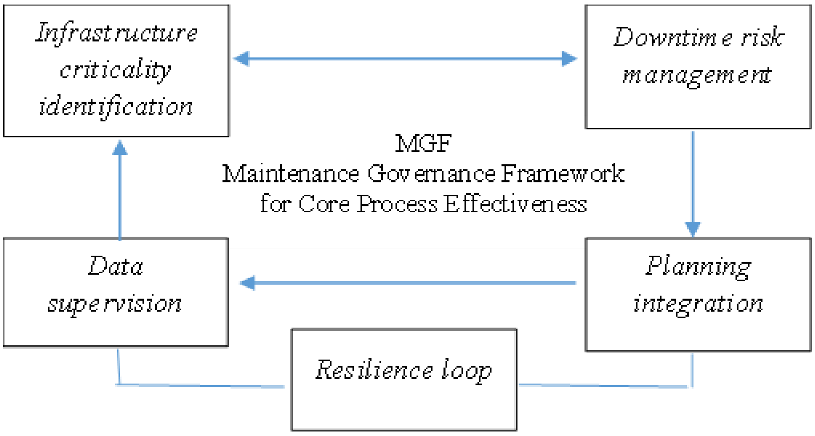

Fig. 1 *A conceptual model of maintenance supervision explaining how supervision of technical infrastructure affects the effectiveness of core processes in conditions of downtime risk. Source: own study.*

MGF consists of five categories of maintenance oversight – infrastructure criticality identification, downtime risk management, planning integration, data supervision and resilience loop – which together form a mediation mechanism between assets and the effectiveness of core process execution [4].

Infrastructure criticality identification – identifies the elements of technical resources that are key to the value streams of core processes.

Downtime risk management – includes threat analysis and assessment of their impact on operational stability.

Planning integration – indicates the link between maintenance schedules and production and demand planning.

Data oversight – refers to the quality of maintenance information, the consistency of indicators and the CMMS/EAM systems used.

Resilience loops - describe adaptive mechanisms, plant decoupling procedures, and restart rules after disruptions.

The central placement of MGF reflects the role of maintenance oversight as a systemic management component that balances performance, risk, and the stability of core processes execution.

3. Assumptions and Research Methodology

This study adopts a qualitative and conceptual analytical approach. The research material consists of ISO 9001:2015 and ISO 55000:2024 standards, literature reviews on RCM/CMB, joint optimisation, MPM and maintenance maturity, as well as publicly available documents and reports from a large industrial organisation, providing a reference context. In addition, non-public, aggregated observations of process `plant availability events were used, solely for illustrative purposes, without providing operational values of identifiers. The analysis was triangulated: normative requirements, research results and contextual observations were compared, and the conclusions were organised within the MGF framework [2, 5, 6].

4. Organisational context and illustration of events

In the analysed organisational context, maintenance is part of an integrated management system, with declared coordination of repair planning, production processes and quality requirements. Two trajectories of disruption were significant in the source observations: external disruptions resulting from the unavailability of a process factor and planned repair shutdowns. In the first case, despite the length of the episodes, the observed market effects were mainly limited to the temporary unavailability of selected product ranges, without a cascading effect on other process plants, which can be interpreted as the effect of segmentation of impact and restart standards. In the second case, the quality of co-planning and the completeness of the scope determined the time needed to reach a stable production process regime. In both cases, maintenance supervision acted as a mediator: it segmented the impact within the process structure, shortened the time to reach a stable regime, and limited the spread of disruptions through decoupling, buffering, and process restart standards. This interpretation is consistent with the assumptions presented in the literature on resilience and with the logic of the ISO 55000 standard, which emphasises ‘assurance’ and ‘adaptability’ as the results of mature asset management [7].

5. Operationalisation of MGF using MPM indicators

The transition from model to measurement requires the operationalisation of MGF categories through MPM indicators, while maintaining the principle that both internal and external (process) effectiveness are assessed, and that the indicators must maintain a line of sight to the objectives. The literature on MPM critically assesses the reduction of assessment to the OEE indicator, pointing to the need to combine multiple dimensions, including data quality and maintenance process maturity [5]. The literature on MPM points to the need to combine internal and external maintenance effectiveness and the need for data supervision, as the OEE indicator is not sufficient to assess the full effectiveness of the process. In line with this, MGF assumes that the assessment of supervision effectiveness cannot be limited to the technical parameters of assets, but should include the variability of the implementation of main process plans, restart times and trajectories, and cascading effects in the process chain [5].

Table 1 shows the relationship between the five MGF categories and the corresponding groups of MPM indicators used to assess the effectiveness and maturity of maintenance supervision. The indicators were selected on the basis of recognised standards and models: asset management (ISO 55000:2024), process and risk-based approach (ISO 9001:2015), and RCM/CBM practices and MPM reviews. The table includes: the measurement objective in a given category, example metrics and typical data sources used in maintenance and production systems.

Tab. 1 *Mapping of MGF categories to MPM indicators, source: own study*

	MGF category	***Measurement objetive***	***Sample MPM indicators***	***Data sources***	***Interpretative notes***
1.	*1. Infrastructure criticality identification.*	*Prioritise resources and align with process goals.*	*Critical asset share [%], Value at risk [PLN/h or %], Redundancy index, Qualitative impact.*	*Asset register, EAM, Process maps, FMEA/RCM, risk analysis.*	*Review criticality as product mix changes (ISO 55000, ISO 9001).*
2.	*2. Downtime risk management.*	*Prevent and limit downtime effect.*	*Unplanned events [#/period], MTBF/MTTF/MTTR [h], Unplanned downtime share [%], RPN/FMEA, CMB coverage [%], Early detection [%]*	*CMMS/EAM, CBM module, event logs, RCA reports.*	*Indicators linked to process risk and predictability.*
3.	*3. Planning integration.*	*Reduce flow variance and cost via joint planning.*	*Plan compliance [%], Scheduled work share [%], Volatility index,*	*APS/MES, CMMS maintenance plan, S&OP.*	*KPIs assessed jointly, not in silos.*

			Maintenance impact, [kg, %]		
4.	*4. Data supervision.*	*Ensure data quality and control.*	*CMMS completeness [%]; Data entry delay [h]; Correct cause classification [%]; Hierarchy errors [%]; KPI audit [YES/NO]; OEE components*	*CMMS/EAM cause dictionaries, KPI, catalogue audits.*	*Combine internal/external efficiency, ensure quality.*
5.	*5. Resilience loop.*	*Reduce disruption duration/scope, prevent cascades.*	*Downtime durations, MTRS, Propagation index, Restart coverage.*	*ESD/OSBL logs, restart procedures, MES.*	*Monitor recovery and dynamics (ISO 55000:2024).*

The following symbols and terms are used in Table 1:

- Measurement objective – explains why a specific MGF category requires monitoring and what impact a given area has on the effectiveness of core processes.
- Sample MPM indicators – include representative measures used in research and maintenance practice, e.g.: MTBF – Mean Time Between Failures, MTTF - Mean Time to Failure, MTTR/TTR - Mean Time to Repair or Repair Time, RPN – Risk Priority Number, OEE – Overall Equipment Effectiveness
- Data sources – indicate systems and repositories used in maintenance practice, e.g.: CMMS/EAM – maintenance and asset management systems, APS/MES – production planning and execution systems, RCM/FMEA – function and risk analysis tools, RCA – root cause analysis.
- Interpretative notes – refer to current international standards and research.

5. Discussion: the mediating role of maintenance supervision and process resilience

The alignment resulting from the content available in the literature on resilience indicates that MGF ‘resilience loops’ – degradation scenarios, decoupling and restart rules – are a prerequisite for reducing the time from an event to stable operation. In environments with the risk of cascading effects, managing impact boundaries and product range priorities is no less important than the time it takes to restore the medium or complete repair work. In this sense, MGF extends classic RCM/CBM with a component of governance and cross-functional coordination, consistent with the current approach of ‘outcomes and maturity’ in the ISO 55000:2024 standard [7].

The results are consistent with the findings of RCM/CBM and total optimisation reviews, which indicate that the maturity of the maintenance process enhances the predictability of the results of core processes [2, 4, 5, 6]. In practice, organisations achieve a sustained reduction in implementation variability when the supervisory decision-making path is clear, maintenance schedules are coordinated with operational plans, and maintenance and quality data are monitored in a information system. The literature on maturity and MPM suggests that development activities should be designed at the factor level (role, responsibility, plan integration, restart standards, KPI consistency) rather than as a pursuit of a single summary indicator. In areas with a high proportion of external disruptions, it is necessary to adopt criteria for allocating risk and restart costs in the logic of the asset life cycle, which is consistent with ISO 55000 and the achievements of maintenance policy optimisation. [1, 5, 6].

5. Limitations and research agenda

This study does not include quantitative validation and is based on secondary sources and confidential, aggregated operational observations. In the future, it is recommended to conduct quantitative validation of the mediating role of supervision in causal models, cross-sectional studies of the maturity of compatible MGF, and natural experiments assessing the impact of the integration of planning and data supervision on implementation variance and restart costs. It is worth combining maintenance data with quality and planning data in time panels and testing joint optimisation solutions with explicit modelling of quality variability in a degradable system [2].

5. Summary

MGF aligns with established models and standards, serving as a unified approach for maintenance oversight in organisations with complex infrastructure. In terms of the requirements of the ISO 55000:2024 standard, MGF provides a practical line of sight from objectives to assets and back to system performance; in terms of the ISO 9001 standard, it organises risk-based thinking in the design of resources for processes. In combination with RCM/CBM and joint optimisation achievements, this framework translates into planning, information and restart decisions, which, as both literature and illustrative observations show, reduces the size and operational scope of disruptions and enhances the effectiveness of core process implementation [6].

References

[1] Dekker, R. (1996). Applications of maintenance optimisation models: A review and analysis. Reliability Engineering & System Safety, 51(3), 229–240. [repub.eur.nl]

[2] Hafidi, N., El Barkany, A., & El Mhamedi, A. (2023). Joint optimization of production, maintenance, and quality: A review and research trends. International Journal of Industrial Engineering and Management, 14(4), 282–296. [link.springer.com]

[3] ISO. (2015). ISO 9001:2015 Quality management systems – Requirements. International Organization for Standardization. [iso-cert.uk]

[4] ISO. (2024). ISO 55000:2024 Asset management — Vocabulary, overview and principles (2nd ed.). International Organization for Standardization. [books.indu...lpress.com], [linkedin.com] Moubray, J. (1997/2001). Reliability-Centered Maintenance (2nd ed.). Industrial Press / Butterworth-Heinemann. [iso.org], [webstore.ansi.org]

[5] Oliveira, M. A., & Lopes, I. (2020). Evaluation and improvement of maintenance management performance using a maturity model. International Journal of Productivity and Performance Management, 69(3), 559–581. [sci-hub.st] [emerald.com]

[6] Quatrini, E., Costantino, F., Di Gravio, G., & Patriarca, R. (2020). Condition-Based Maintenance—An extensive literature review. Machines, 8(2), 31. [scholar.archive.org], [mdpi.com]

[7] Wächter, C., Beckschulte, S., Padrón Hinrichs, M., & Schmitt, R. H. (2024). Strategies for resilient manufacturing: A systematic literature review of failure management in production. Procedia CIRP, 130, 1393–1402. [publicatio...-aachen.de]

PE COMPOSITES WITH ADDITION OF HYDROGEL OBTAINED BY EXTRUSION

P. Jarka[1*], M. Bilewicz[1]
[1]*Silesian University of Technology, Faculty of Mechanical Engineering, Department of Engineering Materials and Biomaterials, Gliwice, Poland*
[*]*email: pawel.jarka@polsl.pl*

1. Introduction

Hydrogel materials belong to a group of functional materials, known in foreign nomenclature as "smart," which can be superabsorbents of water and other liquids. According to the Water Utility Journal [1], a hydrogel can absorb up to 400 times its own weight. This material property can be utilized in polymer composites [2-3]. Using different material ratios and various processing methods opens up a number of possibilities for obtaining functional composites with the ability to control moisture and water absorption [4-5]. The work in this article focuses on polyethylene composite containing hydrogel powder. Idea of composite is to absorb water particles while contacted, so material can be used in specific area, where he humidity or water content must be under control. After fast absorption of water material will release it for longer time. In this case material can be used in agriculture and gardening sector. Very specialized application for hydrogel composites can be also tissue engineering and scaffolds.

2. Results and discussion

To prepare the composite mixtures, a blend of a polymer—polyethylene (PE)—and a hydrogel material (sodium polyacrylate) in varying ratios was used. The ratios were 2% by weight, 4% by weight, 6% by weight, and 8% by weight. Two types of technologies were used: extrusion, where the masterbatch was subjected to high shear rates using a dual extruder; and injection molding, where the polymer in varying ratios was mixed with the hydrogel and injected into the mold cavity with a complex set of settings, including injection pressure, holding pressure, back pressure, and cooling temperatures. The samples after the extrusion and injection molding process were stored for 24 hours in mineral water (approximately 300 mg/l of minerals) and demineralized water (Fig. 1).

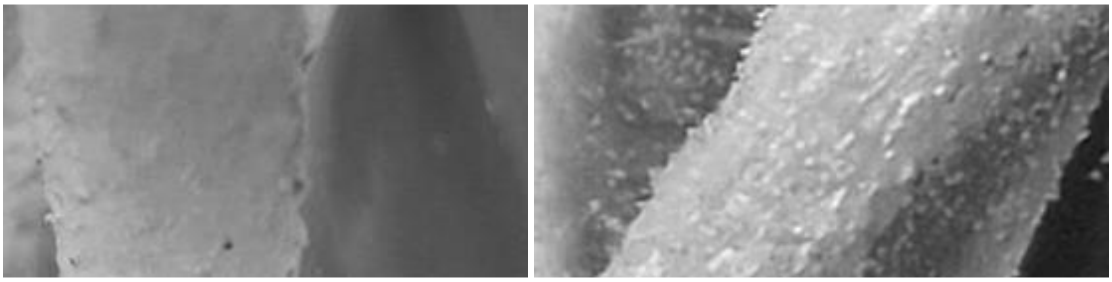

***Fig. 1** Samples kept in the water: demineralized (left), mineralized (right).*

Observation of the samples after extrusion reveals the presence of hydrogel particles coated with polymer, the particles are evenly distributed inside the polymer. It was observed that in some places due to discontinuity of the polymer coating, the hydrogel grew after storage in demineralized water. The particles are saturated with water and sometimes separate from the material (Fig. 2, right sample). Water access to the hydrogel particles within the composite is significantly more difficult in injected samples. The symmetry of the injection molding causes the particles to be confined within the sample, leaving the outer polymer layer inaccessible to the hydrogel particles (Fig. 3).

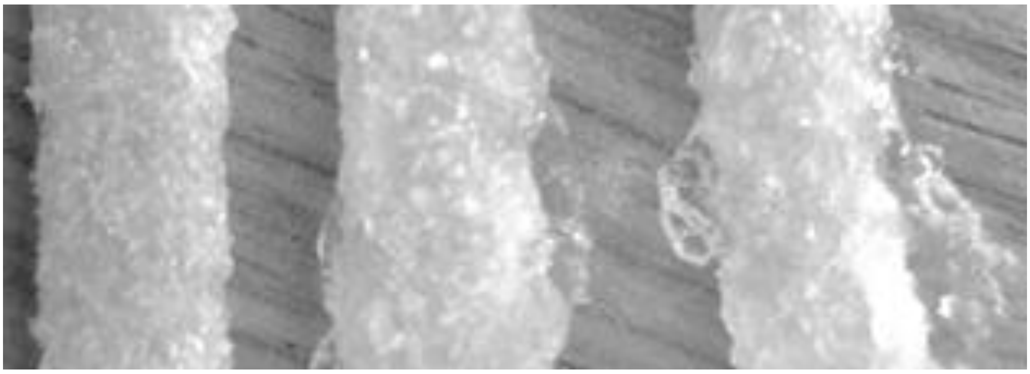

Fig.2 *Saturated particles of hydrogel after keeping in demineralized water (right sample), mineralized water (middle sample), no water (left sample).*

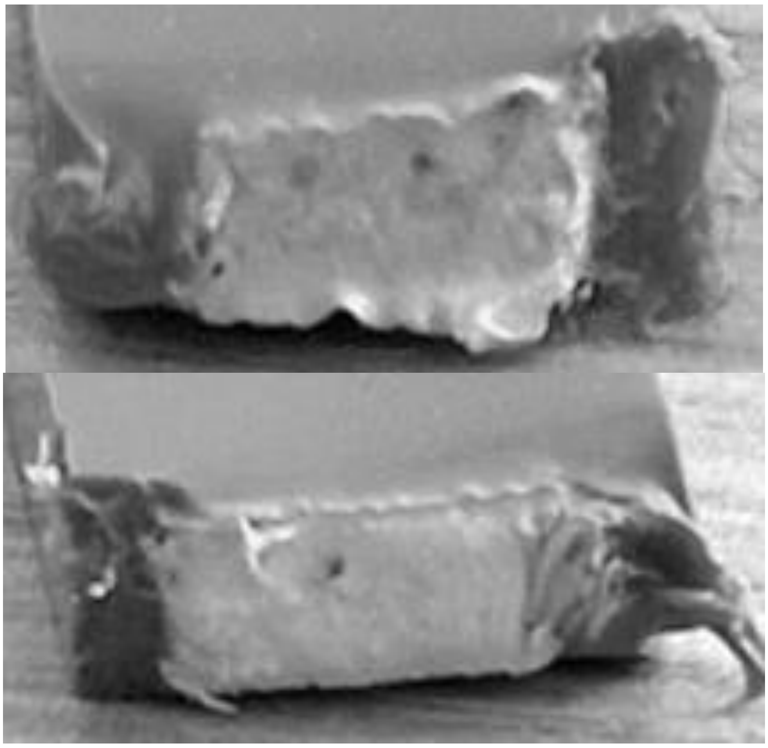

Fig.3 *Cross section of injected samples. No visible hydrogel particles in outer part of sample.*

The samples obtained after extrusion, in which the hydrogel was saturated, were examined under a stereoscopic microscope (Fig. 4). To check the strength of injection molded samples with different hydrogel particle ratios (2 ÷8 wt%), the results are shown in the following graphs (Fig. 5).

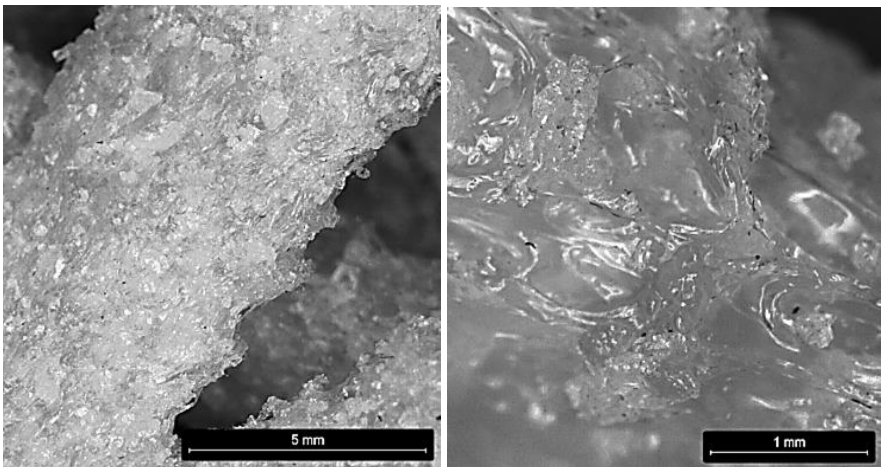

Fig.4 *Samples after extrusion observed using stereoscopic microscopy. Hydrogel particles are located along flow of polymer.*

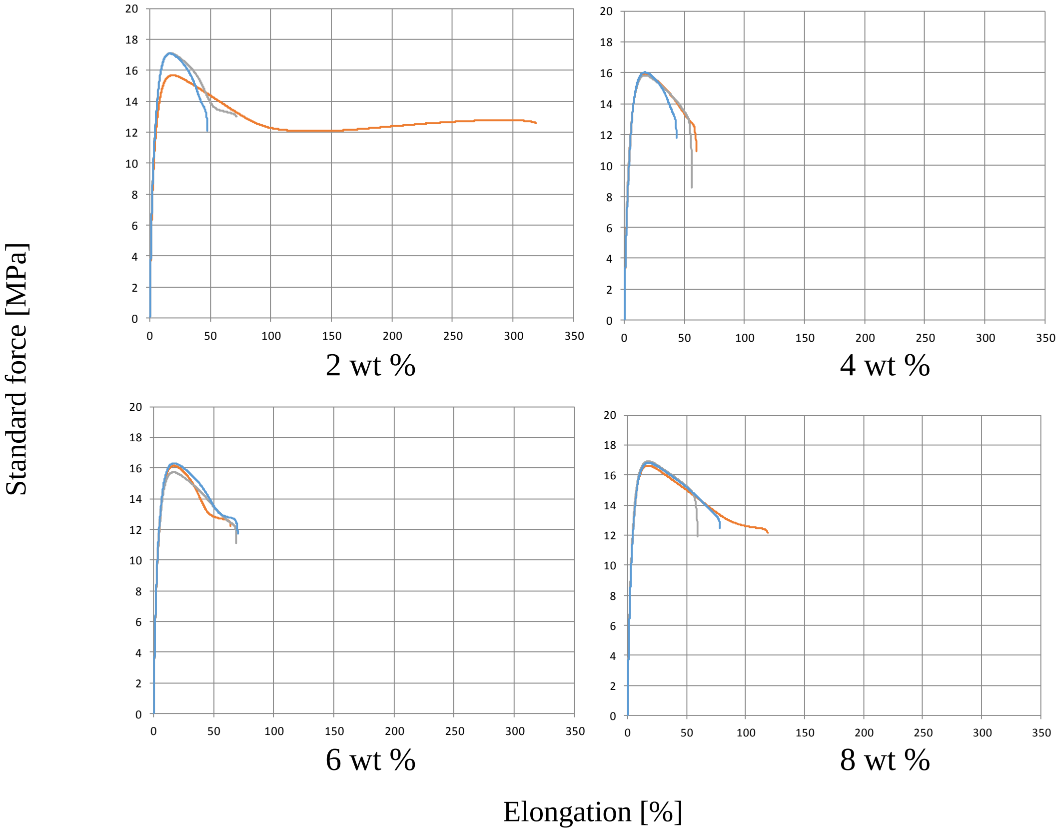

Fig. 5 *Tensile test curve of PE sample with 2-10 wt% of hydrogel particles.*

3. Conclusions

The tensile strength curves show that hydrogel particles do not significantly affect the strength. For samples with 2% wt. hydrogel particles, one sample exhibited a significantly longer tensile path. This may be due to the inhomogeneous mixing of the materials, especially in the case of the lowest hydrogel content. A slight increase in tensile path was observed with increasing hydrogel particle content. The adhesion between hydrogel particles and the polymer matrix deserves closer examination. Further work is also needed to design a porous system or other system that facilitates water access to the particles within the hydrogel composite.

4. Bibliography

[1] K. Lal, U. Singh, D. M. Denis, S. Srivastava, A. Ranjan, The role of polymers in increasing water use efficiency, E.W. Publications, Water Utility Journal 27, 2021, 15-26.
[2] K. Susheel, Polymeric Hydrogels as Smart Biomaterials, Springer International Publishing Switzerland, 2016.
[3] H. Li, V. Silberschmidt, The Mechanics of Hydrogels: Mechanical Properties, Testing, and Applications, Woodhead Publishing, 2022.
[4] J. P. Davim, Biomedical Composites: Materials, Manufacturing and Engineering, De Gruyter, 2013.
[5] M. Bilewicz, I. Zdebel, M. Rak, W. Gębska, M. Gwóźdź, Kompozyty hydrożelowe otrzymywane technologią formowania wtryskowego jako materiały typu smart, XXI Konferencja Naukowo-Techniczna Polimery i kompozyty konstrukcyjne, Wydawnictwo Katedry Mechaniki Teoretycznej i Stosowanej, 2024

29th International Seminar of Ph.D. Students
SEMDOK 2026

Western Tatras – Zuberec, Slovak Republic
February, 4 to February 6, 2026

INFLUENCE OF POWDER RECYCLING ON SURFACE AND SELECTED TECHNOLOGICAL PROPERTIES OF SLM-PROCESSED M300 MARAGING STEEL

Michal Kresta[1*], Josef Hlinka[1], Abdesselam Mechali[2], Marin Petrovic[3], Jakub Mesicek[2], Ibrahim Jahan[4], Jiri Hajnys[2], Jana Petru[2]
[1] Department of Materials Engineering, Faculty of Materials and Technology, VSB-Technical University of Ostrava, 17. listopadu 2172/15, 708 00 Ostrava-Poruba, Czech Republic
[2] Department of Machining, Assembly and Engineering Metrology, Faculty of Mechanical Engineering, VSB-Technical University of Ostrava, 17. listopadu 2172/15, 708 00 Ostrava-Poruba, Czech Republic
[3] Faculty of Mechanical Engineering, University of Sarajevo, Vilsonovo setaliste 9, 71000 Sarajevo, Bosnia and Herzegovina
[4] Libyan Authority of Science Research, Tripoli P.O. Box 80045, Libya
**Corresponding author: michal.kresta@vsb.cz*

1. Introduction

The use of additive manufacturing in industry is steadily increasing. These techniques are applied in many fields such as automotive, aerospace or healthcare. The main advantage of 3D printing is to produce complex shapes that are impossible with traditional methods. The material consumption has also been reduced. One of the most important 3D printing technologies is Selective Laser Melting (SLM). SLM method works with material's powders. Powders are melted layer-by-layer with high-powered lasers in the areas corresponding to the cross-section of each individual layer [1-3].

Maraging steels are special high-strength steels hardened by precipitation of intermetallic compounds. Maraging means martensite age hardening. These steels contain very low carbon, but many alloying elements. Grades M300 are used in many fields where strong structure is necessary. This steel finds its application in aerospace, military, medical or automotive. Unique properties are achieved by heat treatment and subsequent aging. The austenite matrix converts into the martensite. The high nickel content suppresses the formation of ferrite and pearlite, enabling martensite formation even at low cooling rates. The resulting martensite is significantly softer than that found in conventional carbon steels. The steel is then tempered. During this process of aging intermetallic particles are formed. These processes are known as precipitation hardening [4, 5].

The SLM technology enables the reuse of unused powder from the build chamber, but basic chemical composition must be maintained. Recycling reduces production costs and simplifies powder disposal. These factors reduce the environmental impact of 3D printing. There are several obstacles during powder recycling. The chemical composition is influenced by repeated recycling cycles. As result this could lead to lower mechanical and technological properties [6, 7].

This research shows how 20 recycling cycles affect selected material properties. Such as wettability, roughness and corrosion resistance, both with and without blackened surfaces.

2. Materials and Methods

Samples were made from powder of M300 maraging steel by 3D printing technique SLM. The initial powder of M300 maraging steel was from the Carpenter Technology Corporation (Renishaw plc, Wotton Under Edge, UK). The recycled powder was used after 20 cycles of printing.

The corrosive effect and analysis of the surface was performed by SEM (Scanning Electron Microscope) FEI 450 Quanta FEG (FEI Company, Brno, Czech Republic) equipped with an EDAX EDS detector (AMATEK Company, Tilburg, The Netherlands) in the secondary electron mode. The working distance was 10-15 mm.

Corrosion tests were done in three solutions on the untreated and blackened surfaces of both samples. The first solution was an acidic environment with a PH of 3. The second solution was an alkaline mixture with a pH of 11. The third solution was a 3.5 NaCl water solution. For each measurement 15 ml of each solution was used. The measurement was carried out via a potentiodynamic test, where 0.5 cm^2 of the surface was tested. Individual samples were placed in corrosion cells and were connected to the working electrode. Two electrodes were immersed in the solution. The first of them was an auxiliary one consisting of a carbon rod, and the reference electrode was a calomel electrode (SCE) with a potential of 244 mV vs. a standard hydrogen electrode (SHE) against which all listed potentials were further referenced.

The sessile drop technique was used to measure the surface contact angle to assess the wettability. Pictures of drops were evaluated by SEE (Surface Energy Evaluation) system with software Adwex Device. To measure two-dimensional surface roughness the contact profilometer Talysurf 50 (Taylor Hobson Precision) was used.

Blackening is a surface treatment, that partially protects the steel against corrosion. The name is related to the resulting colour of the surface. It can be performed cold and hot. Hydrated forms of magnetite (iron-iron oxide) form on the surface by oxidation reaction. These oxides protect surface from further oxidation. This technique is often used for protection of firearms weapons and cannons. The investigated material could be used in the arms industry. For this reason, the cold blackening solution CHEM-WELD 9310 was used. The solution contained a mixture of selenium dioxide, nickel and copper sulphate. The samples were degreased and immersed in the solution for 60 seconds.

3. Results and discussion

In the evaluation of surface roughness, *R* parameters calculated from the roughness profile were used. The parameter *Ra* represents the arithmetic mean of the absolute values of the roughness profile. *Rz* is defined as the average value of the absolute heights of the five highest peaks and the five deepest valleys of the profile.The results of roughness surface and wettability testing are in Tab.1. It can be said that neither the blackening nor the type of powder used for printing has any effect on the surface roughness. To improve the accuracy of the results and to verify the effect of recycled powder, additional measurements on a larger number of samples would be required. However, based on the study by Ryan et al. [8] on MAR 300 steel, it can be concluded that recycled powder has no effect on surface roughness parameters.

Both types of powder exhibited wetting behaviour, the contact angle was less than 90 degrees, Fig. 1a). The blackened surface behaved more hydrophobically, and the wetting angle was higher than 125 degrees, Fig. 1b). The influence of the recycled powder on wettability was negligible. On average, the recycled powder exhibited lower contact angle values than the virgin powder; however, the large measurement deviations prevented any definitive conclusions regarding the influence of powder type on surface wettability.

Tab. 1 *Values of surface roughness and surface contact angle.*

Sample	*Ra (μm)*	*Rz (μm)*	*Contact angle (°)*
Virgin untreated	*4.69±0.52*	*21.73±1.92*	*83.70±9.82*
Virgin blackened	*5.63±1.43*	*25.31±0.62*	*131.60±4.00*
Recycled untreated	*5.34±0.17*	*24.17±0.99*	*76.58±10.94*
Recycled blackened	*5.49±0.47*	*24.07±1.87*	*127.72±7.75*

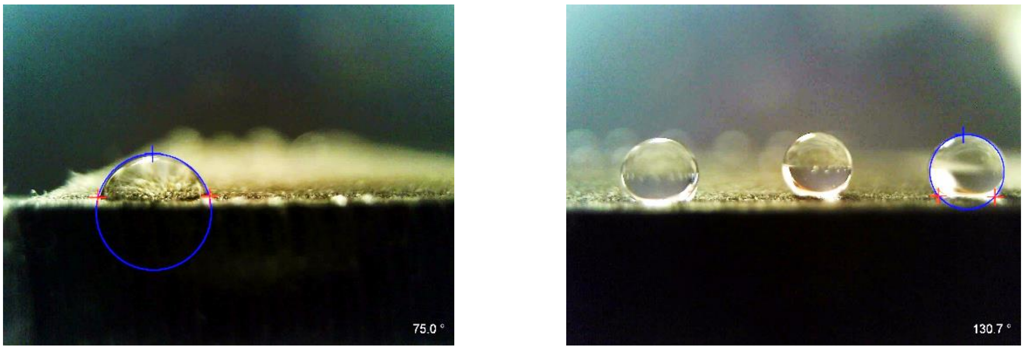

a) Untreated surface *b) Blackened surface*

Fig. 1 *Contact angles.*

The corrosion tests results are in Tab. 2-4. The following parameters were measured: corrosion potential (*E),* corrosion current, polarization resistance (*Rp)*, and corrosion rate. The results obtained at pH 3 are shown in Tab. 2. The corrosion potential of all samples ranged from −493 to −454 mV, with the lowest value measured for the untreated recycled powder. Untreated surfaces consistently exhibited lower corrosion currents than blackened ones. Blackened surfaces showed higher corrosion rates, than untreated samples. Overall, corrosion proceeded faster on blackened surfaces in the acidic environment. No clear effect of powder recycling on corrosion behaviour was observed; however, the untreated virgin powder showed slightly better corrosion resistance than the recycled powder.

The effect of an alkaline environment with pH 11 is documented by the results in Tab. 3. the corrosion potentials vary significantly, with paradoxically similar values observed for dissimilar sample pairs (untreated virgin–blackened recycled and vice versa). The lowest corrosion potential was measured on the untreated surface of the virgin sample, while a value only 4 mV higher was recorded for the blackened surface of the recycled sample. The corrosion current varied over three orders of magnitude, from tenths to tens of $\mu A/cm^2$. Blackening had a negative effect on the corrosion rate even in the alkaline environment, with higher corrosion rates observed for blackened surfaces. For the virgin powder, the difference was not so high (7 µm/year). In contrast, the recycled powder showed a two-order-of-magnitude increase in corrosion rate after blackening, from 9.7 µm/year to 202.4 µm/year.

***Tab. 2** Results of the potentiodynamic corrosion test in an acidic environment, pH 3*

pH 3	*E (i=0) (mV)*	*Corrosion Current (µA/cm^2)*	*Rp (kOhm·cm^2)*	*Corrosion Rate (µm/Year)*
Virgin untreated	*-478.6*	*12.30*	*3.46*	*144.2*
Virgin blackened	*-475.2*	*67.27*	*0.84*	*788.9*
Recycled untreated	*-493.2*	*16.97*	*3.04*	*198.9*
Recycled blackened	*-454.6*	*21.67*	*2.32*	*254.1*

***Tab. 3** Results of the potentiodynamic corrosion test in an alcalic environment, pH 11*

pH 11	*E (i=0) (mV)*	*Corrosion Current (µA/cm^2)*	*Rp (kOhm·cm^2)*	*Corrosion Rate (µm/Year)*
Virgin untreated	*-440.5*	*4.37*	*8.6*	*51.2*
Virgin blackened	*-259.7*	*5.02*	*9.6*	*58.9*
Recycled untreated	*-242.1*	*0.83*	*44.5*	*9.7*
Recycled blackened	*-436.9*	*17.26*	*2.8*	*202.4*

The results in 3.5% NaCl (Tab. 4) show higher corrosion potentials for untreated surfaces than for blackened ones, indicating improved corrosion resistance after blackening. Recycled powder samples exhibited higher corrosion currents and corrosion rates than virgin samples, without a consistent trend. Blackening improved corrosion resistance for recycled powder but caused an almost twofold deterioration for virgin powder.

***Tab. 4** Results of the potentiodynamic corrosion test in NaCl solution.*

3.5 % NaCl	*E (i=0) (mV)*	*Corrosion Current (µA/cm^2)*	*Rp (kOhm·cm^2)*	*Corrosion Rate (µm/Year)*
Virgin untreated	*-435.5*	*21.31*	*423.4*	*249.9*
Virgin blackened	*-392.3*	*39.13*	*312.3*	*458.8*
Recycled untreated	*-414.0*	*61.40*	*273.9*	*720.0*
Recycled blackened	*-391.1*	*45.90*	*277.3*	*537.9*

Based on the results of the corrosion tests, it cannot be said with certainty that recycled powder either deteriorate or improves the corrosion properties of the material. The measured data were too inconsistent, and additional measurements would be required to determine the effect. In the study of Barille et al. [9] dealing with the influence of powder recycling on the corrosion properties of AlSi10Mg alloy prints, it was concluded that recycled powder does not significantly affect the corrosion behaviour of 3D-printed parts. A SEM was also used to examine the surfaces of the samples. Set of images (Fig. 2) show the surface of the sample in the three different cases: a) before blackening and before corrosion, b) after blackening and before corrosion, c) after blackening, after corrosion. Images illustrate that blackening leads to the partial corrosion of the untreated powder particles. Before blackening the particles had a smooth surface and after blackening there are defects in the form of pits on them (Fig. 2b)). The presence of these pits indicates the initiation and development of corrosion processes that locally occurred already during the blackening process. The surfaces of these affected areas remain in an active state, as they are not protected even by a very thin oxide layer, which normally forms on free surfaces during SLM processing, and are therefore more susceptible to further corrosion attack. This observation is consistent with the results presented in this paper, where blackened surfaces exhibit significantly higher corrosion rates, lower corrosion potential values, and lower polarization resistance compared to untreated surfaces. After corrosion testing, surface changes in the form of corrosion products, small bright areas in Fig. 2b).

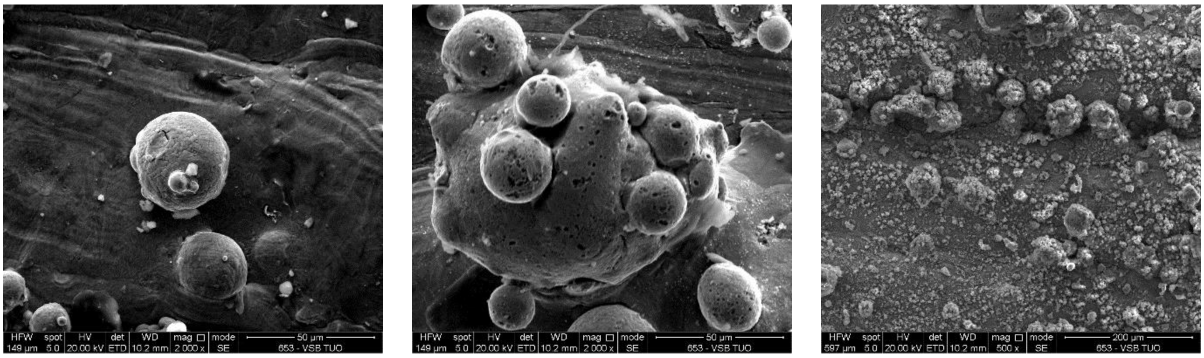

a) Unblackened, no corrosion *b) Blackened, no corrosion* *c) Blackened, corrosion*

Fig. 2 *Sample surface (SEM, in secondary electrons)*

4. Conclusion

The aim of this work was to determine whether recycled powder in SLM-based 3D printing affects the surface and selected technological properties of M300 steel. The results can be summarized in the following points.

- Roughness measurements on untreated and blackened surfaces of both sample types showed that neither the powder type nor blackening affected the surface roughness parameters.
- Blackened surfaces exhibited higher contact angles than untreated surfaces and were therefore more hydrophobic. Recycled powder did not influence surface wettability.
- Corrosion tests did not demonstrate that recycled powder affects the corrosion properties of the material. In all evaluated measurements, the data showed no clear trend, and further testing with a larger dataset would be needed to assess the

influence of powder recycling. Blackening caused partial corrosion attack on the surface of both types of samples, regardless of the powder used.

This study shows that parts made from recycled M300 maraging steel powder exhibit properties largely comparable to those of virgin powder; however, certain differences remain and require further investigation. Additional research is especially needed to evaluate practical applications of recycled powders, given the observed variations in corrosion resistance and contamination risks.

Acknowledgment

This article was created with the contribution of project **SP2026/053 "Comprehensive evaluation of the influence of production and processing technologies and degradation mechanisms on the properties of structural materials".**

References

[1] N. Khan and A. Riccio, 'A systematic review of design for additive manufacturing of aerospace lattice structures: Current trends and future directions', Prog. Aerosp. Sci., vol. 149, p. 101021, Aug. 2024, doi: 10.1016/j.paerosci.2024.101021.
[2] A. N. Aufa et al., 'Current trends in additive manufacturing of selective laser melting for biomedical implant applications', J. Mater. Res. Technol., vol. 31, pp. 213–243, July 2024, doi: 10.1016/j.jmrt.2024.06.041.
[3] J. Bochnia, T. Kozior, and J. Zyz, 'The Mechanical Properties of Direct Metal Laser Sintered Thin-Walled Maraging Steel (MS1) Elements', Materials, vol. 16, no. 13, p. 4699, Jan. 2023, doi: 10.3390/ma16134699.
[4] Y. Li et al., 'The influence of post-aging treatment on the microstructure and micromechanical behaviors of additively manufactured maraging steel investigated by in situ high-energy X-ray diffraction', J. Mater. Sci. Technol., vol. 200, pp. 1–12, Nov. 2024, doi: 10.1016/j.jmst.2024.02.044.
[5] Z. Brytan et al., 'Microstructural and Mechanical Properties of Novel Co-Free Maraging Steel M789 Prepared by Additive Manufacturing', Materials, vol. 15, no. 5, p. 1734, Jan. 2022, doi: 10.3390/ma15051734.
[6] J. Mesicek et al., 'Abrasive Surface Finishing on SLM 316L Parts Fabricated with Recycled Powder', Appl. Sci., vol. 11, no. 6, p. 2869, Jan. 2021, doi: 10.3390/app11062869.
[7] C. Lu et al., 'A comprehensive characterization of virgin and recycled 316L powders during laser powder bed fusion', J. Mater. Res. Technol., vol. 18, pp. 2292–2309, May 2022, doi: 10.1016/j.jmrt.2022.03.125.
[8] O. Rayan, J. Brousseau, C. Belzile, and A. E. Ouafi, 'Maraging steel powder recycling effect on the tensile and fatigue behavior of parts produced through the laser powder bed fusion (L-PBF) process', Int. J. Adv. Manuf. Technol., vol. 127, no. 3, pp. 1737–1754, July 2023, doi: 10.1007/s00170-023-11522-x.
[9] C. Barile, C. Casavola, V. Paramsamy Kannan, and G. Renna, 'The influence of AlSi10Mg recycled powder on corrosion-resistance behaviour of additively manufactured components: mechanical aspects and acoustic emission investigation', Arch. Civ. Mech. Eng., vol. 22, no. 1, p. 52, Jan. 2022, doi: 10.1007/s43452-022-00375-y.

29th International Seminar of Ph.D. Students

SEMDOK 2026

Western Tatras – Zuberec, Slovak Republic
February, 4 to February 6, 2026

CFD OPTIMIZATION OF POLYMER FLOW IN EXTRUSION DIES

Mariusz Król[1*], Juraj Beniak[2], Mirosław Bonek[3]
[1,3] Silesian University of Technology, Faculty of Mechanical Engineering, Department of Engineering Materials and Biomaterials, Gliwice, Poland
[2] Slovak University of Technology in Bratislava, Faculty of Mechanical Engineering, Bratislava, Slovakia
**Corresponding author: mariusz.krol@polsl.pl, Konarskiego 18A, 44-100 Gliwice, Poland*

1. Introduction

Every extrusion company strives to eliminate costly prototypes and shorten design cycles. With SolidWorks Flow Simulation, advanced physical simulations are available to virtually anyone. This intuitive and easy-to-use tool allows every engineer and designer to gain a deep understanding of the interactions between profile geometry and process variables for a specific polymer.

The implementation of SolidWorks Flow Simulation translates into real profits: from a significant reduction in product development costs to improved extrusion quality, resulting in higher production efficiency and greater customer satisfaction.

The right design decisions must be made by detecting potential defects before the die is manufactured. Even the most complex profiles can be verified for production. With built-in tools for creating and simplifying geometry, CAD models can be quickly modified directly in the program.

This allows for early elimination of problems such as:

- Unbalanced flow,
- Material overheating,
- Poor profile surface quality.

An additional advantage of this solution is the ability to test alternative materials and mixtures without interrupting actual production. Simulation allows you to accurately predict die swell and optimize cooling systems, which is crucial for maintaining dimensional tolerances. As a result, instead of conducting multiple trials on the press, you get a ready-made and proven solution the first time around (First-Time-Right). Such digitization of the process not only protects the machine park from unnecessary wear and tear, but above all builds the company's image as a technological leader, capable of completing even the most demanding orders in record time [1-13].

2. Material and design

The aim of this work is to apply computational fluid dynamics (CFD) methods to analyze and optimize polymer flow in extruder heads. The work aims to identify key geometric and process parameters affecting flow uniformity, pressure distribution, and shear stress in the flow channel. The ultimate goal is to propose extruder head design solutions that improve the quality of the final product and increase the efficiency of the extrusion process.

The scope of work includes:

- conducting CFD simulations of polymer flow in the extruder head,

- analyzing simulation results, in particular the distribution of velocity, pressure, and stress,
- optimization of selected geometric or process parameters to improve flow uniformity,
- comparison of results before and after optimization, and formulation of conclusions and design recommendations.

SolidWorks software, in particular the SolidWorks Flow Simulation module, was used in the work to perform numerical simulations of polymer flow.

The type of gasket and design of extrusion die chosen for simulation has been presented in figure 1.

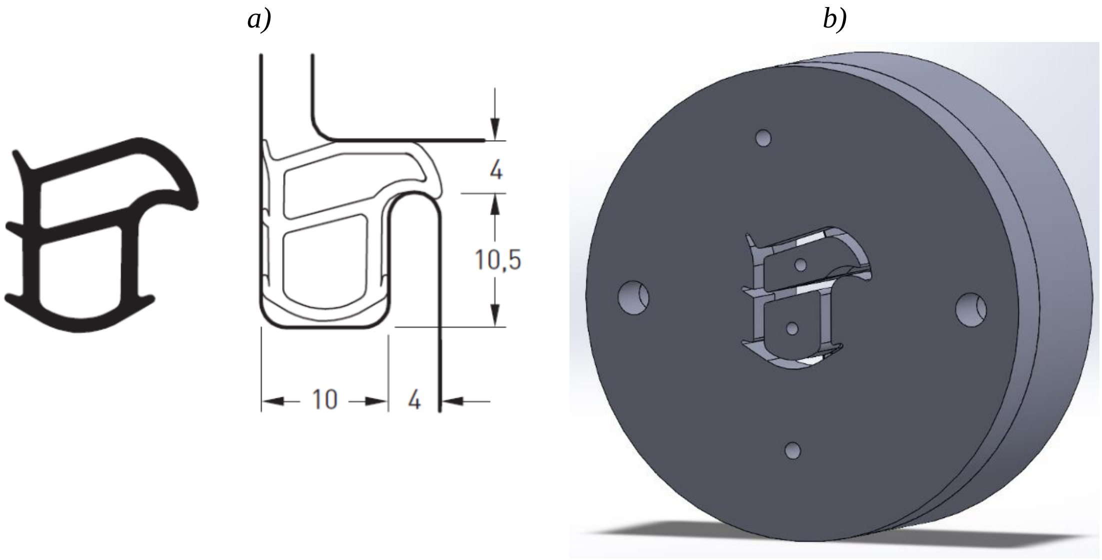

Fig. 1 *Selected type of commercially available gasket and extrusion tool design.*

The boundary conditions adopted were chosen to faithfully represent the actual operating conditions of the extrusion head while ensuring the stability and accuracy of the numerical calculations in the SolidWorks Flow Simulation environment.

A constant polymer mass flow rate was applied at the inlet to the flow channel, corresponding to the operating conditions of an extruder, where screw capacity is approximately constant for the specified process parameters. The use of this type of boundary condition enables direct linkage between the numerical simulation and the actual process data. The polymer inlet temperature was assumed constant and corresponds to the polymer melt temperature at the exit of the plasticizing zone, which is a typical assumption in CFD analyses of the extrusion process.

A static pressure condition equal to atmospheric pressure was applied at the head outlet. This assumption is justified by the fact that the molten polymer exits the head and enters an environment with a known and constant pressure. This condition allows for the correct determination of the pressure distribution throughout the computational volume.

Tab 1. *Solidworks Flow Simulation set-up*

Area	**Type of condition**	**SolidWorks Flow Simulation**
Inlet	Mass flow	*Boundary Condition → Mass Flow Rate*
	Temperature	*Inlet Temperature-200*°C
	Speed profile	*Default*
Outlet	Static pressure	*Boundary Condition →* 101 325 Pa
Channel walls	Speed condition	*Wall Condition → No Slip*
	Thermal condition	*Wall Temperature - 200*°C
	Roughness	Default
Material	Liquid model	*Non-Newtonian Fluid*
	Viscosity model	*Power Law*
Initial conditions	Velocity	0.16 m/min
	Pressure	Static pressure
	Temperature	Global Initial Condition
Type of analysis	Flow Type	*Laminar Flow*
	Time	*Steady State*

A no-slip condition was assumed on the flow channel walls, meaning that the polymer velocity at the walls is zero. This assumption is commonly used in modeling the flow of molten polymers and is consistent with the literature. The thermal condition for the walls was defined as a constant temperature, corresponding to the extrusion head temperature, allowing for the impact of heat transfer between the polymer and the tool on the rheological properties of the melt.

The simulation was conducted under steady-state and laminar flow conditions, which is justified by the nature of molten polymer flow in extrusion heads, where low Reynolds numbers dominate. Adopting these assumptions allows for a reduction in the complexity of the computational model while maintaining the appropriate accuracy of the results.

3. Results and discussion

Results of extrusion die design optimization has been presented on figure 2.

CFD simulations conducted in SolidWorks Flow Simulation enabled a detailed analysis of the velocity, pressure, and shear stress distributions within the extrusion head flow channel. Using a non-Newtonian fluid model and assuming laminar flow enabled a faithful representation of the polymer's rheological behavior under steady-state conditions. Analysis of the results presented in Figure 2 indicates that modifying the channel geometry significantly improved the uniformity of the polymer flow. Optimization eliminated areas of unbalanced flow and reduced the risk of material overheating by better matching process parameters to the profile geometry. Using built-in CAD tools for rapid model modification allowed for efficient testing of alternative design variants. As a result, a stable pressure distribution was achieved, which is crucial for maintaining dimensional tolerances and predicting die swell.

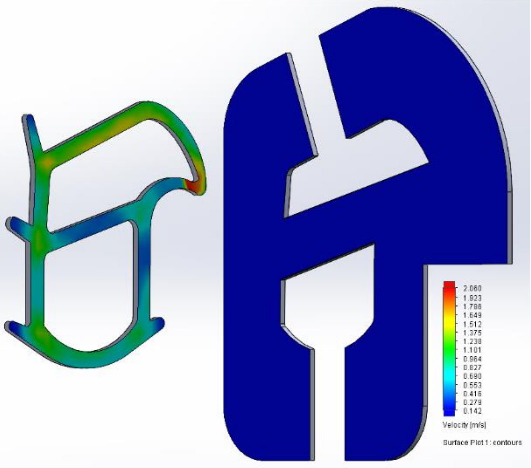

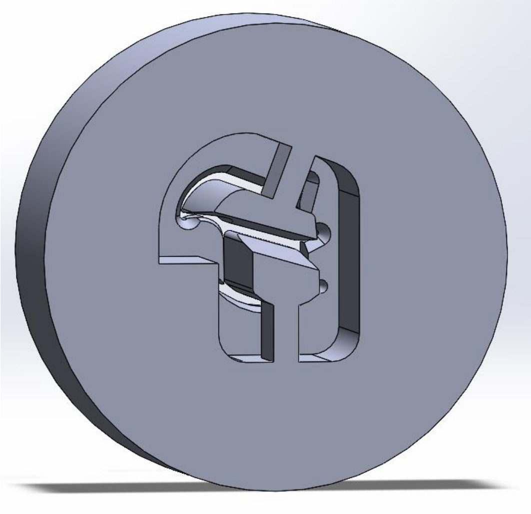

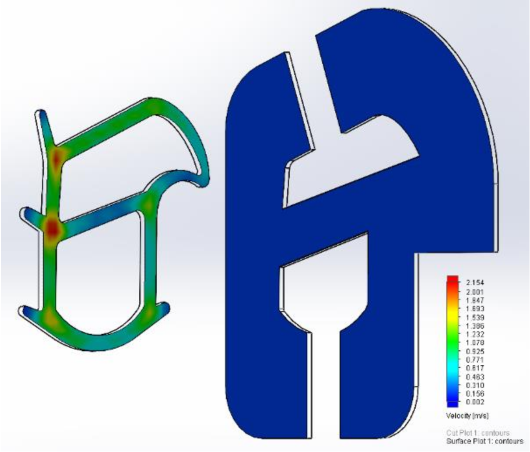

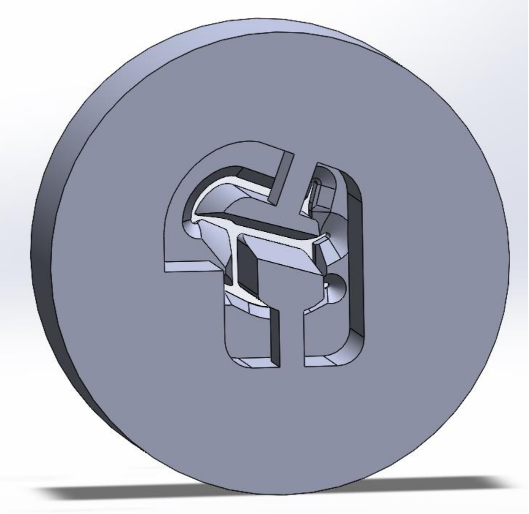

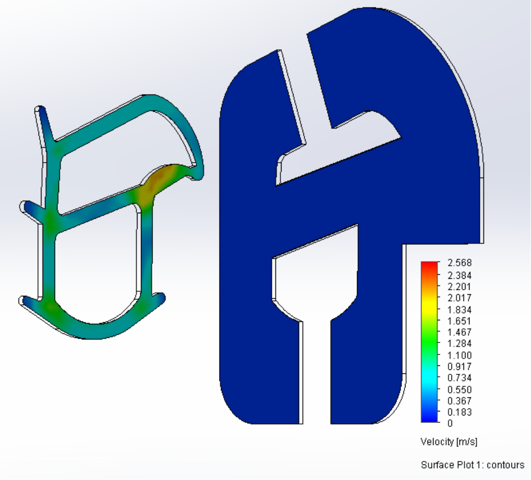

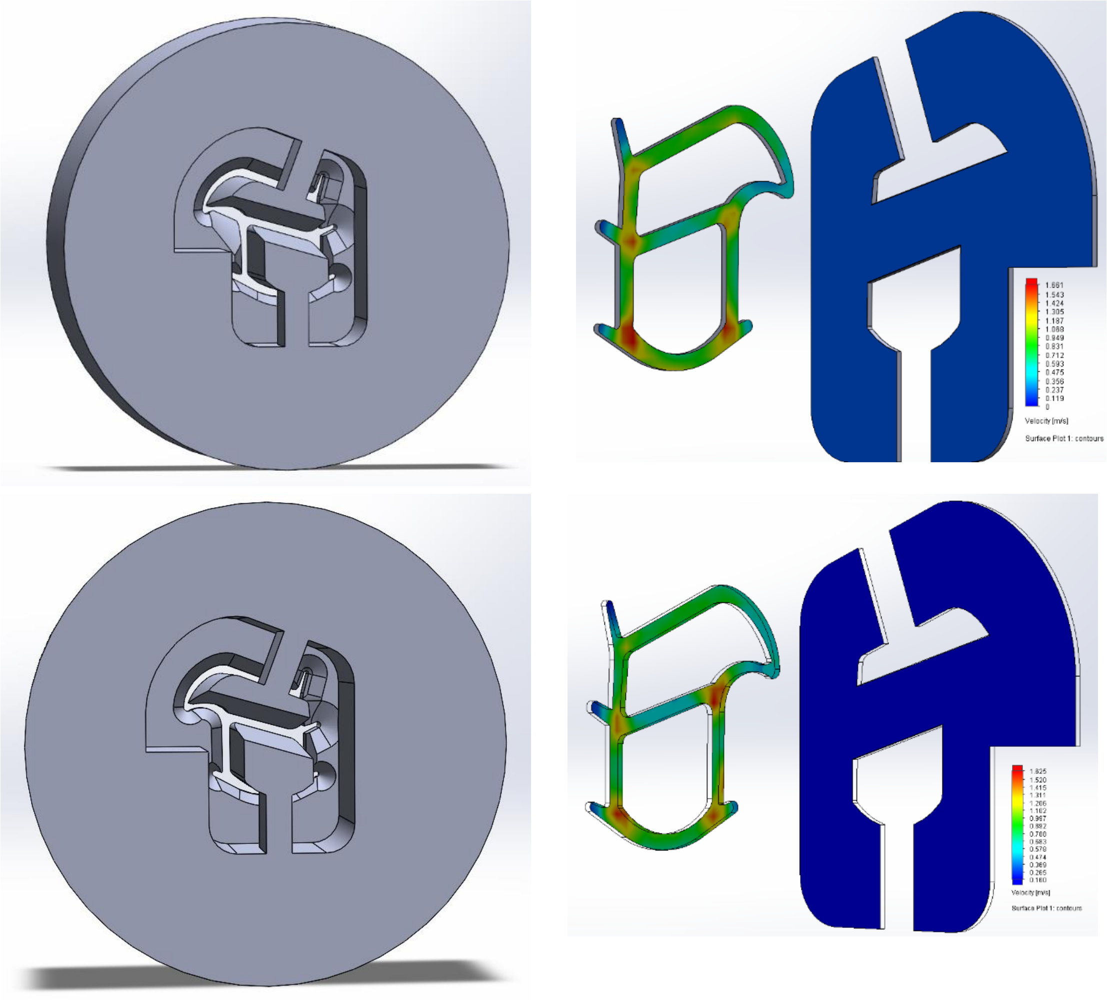

Fig 2. *Extrusion die design optimization and flow simulations results*

3. Conclusions

Based on the conducted research, the following conclusions were drawn:

- The use of computational fluid dynamics (CFD) methods allows for the effective elimination of costly prototypes and shortening of design cycles in polymer processing.
- Simulation in the SolidWorks Flow Simulation environment enables early detection of design flaws, such as unbalanced flow or material overheating, even before the tool manufacturing stage.
- A "First-Time-Right" approach, based on process digitization, significantly reduces product development costs and protects machinery from unnecessary wear.
- The adopted boundary conditions, including a constant mass flow at the inlet and a no-slip condition on the walls, ensured the stability of the calculations and a high level of model accuracy with actual operating conditions.

Acknowledgment

The scholar would like to acknowledge the International Visegrad Fund for the financial support during the realization of the research project. The most thanks are directed to prof. MSc. Juraj Beniak, PhD. from the Institute of Production Engineering and Quality, Faculty of Mechanical Engineering, Slovak University of Technology in Bratislava for friendship and invaluable help while doing the research.

Visegrad Fund

References

[1] Tadmor Z., Gogos C. G. :Principles of Polymer Processing, John Wiley & Sons, 2006.
[2] Rauwendaal C.: Polymer Extrusion, Hanser Publishers, 5th Edition, 2014.
[3] Bird R. B., Armstrong R. C., Hassager O.: Dynamics of Polymeric Liquids, Volume 1: Fluid Mechanics, Wiley-Interscience, 1987.
[4] Macosko C. W.: Rheology: Principles, Measurements and Applications, Wiley-VCH, 1994.
[5] White J. L., Potente H., Screw Extrusion: Science and Technology, Hanser Publishers, 2003.
[6] Versteeg H. K., Malalasekera W.: An Introduction to Computational Fluid Dynamics: The Finite Volume Method, Pearson Education, 2007.
[7] Ferziger J. H., Perić M., Street R. L.: Computational Methods for Fluid Dynamics Springer, 2020.
[8] Osswald T. A., Hernández-Ortiz J. P.: Polymer Processing: Modeling and Simulation, Hanser Publishers, 2006.
[9] Chiang H. H., Hieber C. A., Wang K. K.: “A unified simulation of the filling and postfilling stages in injection molding.”, Polymer Engineering and Science, 1991.
[10] Agassant J. F. et al. : “Polymer processing: modeling and simulation.”, Journal of Non-Newtonian Fluid Mechanics, 2006.
[11] Michaeli W., Hoffmann H.: “Flow balancing in extrusion dies using numerical simulation.”, Polymer Engineering and Science, 1995.
[12] Dassault Systèmes, SolidWorks Flow Simulation – Technical Reference and User Guid
[13] Design and selective laser melting manufacturing of TPE extrusion die
[14] Król M., Musiorski M., Pagac M., W: Advances in laser and surface material processing, Solid State Phenomena, 2020, vol. 308, Stafa-Zurich, Trans Tech Publications, s.51-63, ISBN 978-3-0357-1652-8.

29th International Seminar of Ph.D. Students
SEMDOK 2026
Western Tatras – Zuberec, Slovak Republic
February, 4 to February 6, 2026

EXPLOSION WELDING OF METALS, PHYSICAL ASPECTS AND APPLICATIONS

JAN LOKAJ[a,b], JAN HIVES[a] ,MIROSLAV SAHUL[c] , MARTIN SAHUL[b]
[a] *Faculty of Food and Chemical Technology, Slovak University of Technology, Bratislava, Radlinského 12, 812 37 Slovakia*
[b] *Faculty of Material Science, Slovak University of Technology, Paulínska 16, 91724 Trnava Slovakia*
[C] *Faculty od Mechanical Engineering CTU Prague, Technicka 4, 160 00 Prague*

1. INTRODUCTION

The development of science and technology is oriented towards higher useful properties of materials made by progressive technologies. One of such technologies is solid state joining of metals. Part of material production are technological processes and the materials produced by them, which are characterized by high technical parameters. In some cases, this is also their high purity, which makes even common technical metals closer in price to expensive metals. An important finding is that materials such as Al and CrNi steel (and any others) which are already known in practice, cannot be metallurgically joined together using conventional or special melting technologies. This prompted a more thorough study of special solid-state welding technologies, in which such a combination of metals could be handled also in terms of weldability at the required level. A very important conclusion from the material science point of view is that materials such as Al, NiCr steels, Cu 99.5%, CuSn6, AlMg0.7Si and many light materials such as Mg can not be metalurgically joined by classical. One of the possible special technology seems to be **welding by explosion** which can be described as **high speed welding**. But, joining materials with relatively different physico-chemical properties and with differrent crystallographic lattice, up to now did not show reliable results. Thus, the explosion welding is a method which might form stable joints between alike metals or metals with different physico- chemical properties. This technology can be used to weld one or more metal layers on the top of each other with bonding areas up to several **m^2**. Explosion welded joints have a typical currugated interface which characterises both the welding process and the quality of the joint [1,2] (Fig. 1)

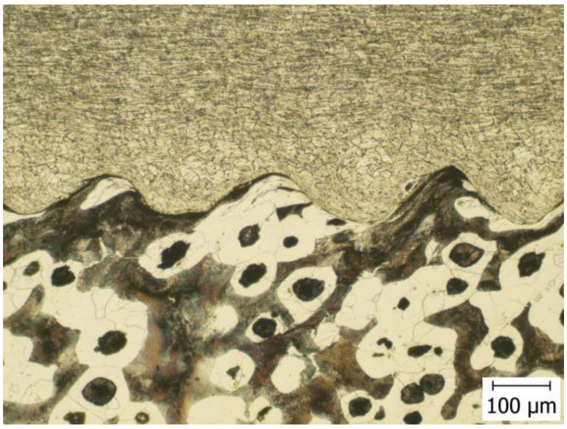

Fig. 1 *Welded interface of a bimetal*

As more and more metals of different properties are combined, the number of methods by which such metals can be combined decreaces. The most common combination and application of multiple materials are [3-5] :

a. Cladding of corrosion resistant materials (CrNi steel, Al,Cu, Ni and their alloys, Ti, Pt etc.) on common structural carbon steel and other materials. With the rule, these are double-layered materials where the carbon steel serves as the structural material and the clad layer acts as corrosion protection. These materials find their application mainly in the chemical, energy and food industries because of their advantageous price.

b. The materials to be rolled are used in similar combination to the previous group. The main advantage of blanks made in this way is the avoidance of oxidation of the surface of the rolled bimetal

c. Composites serving as structural intermediates. These materials are characterized by a large variety of welded material combination. The possible combination of materials are shown in Fig. 2

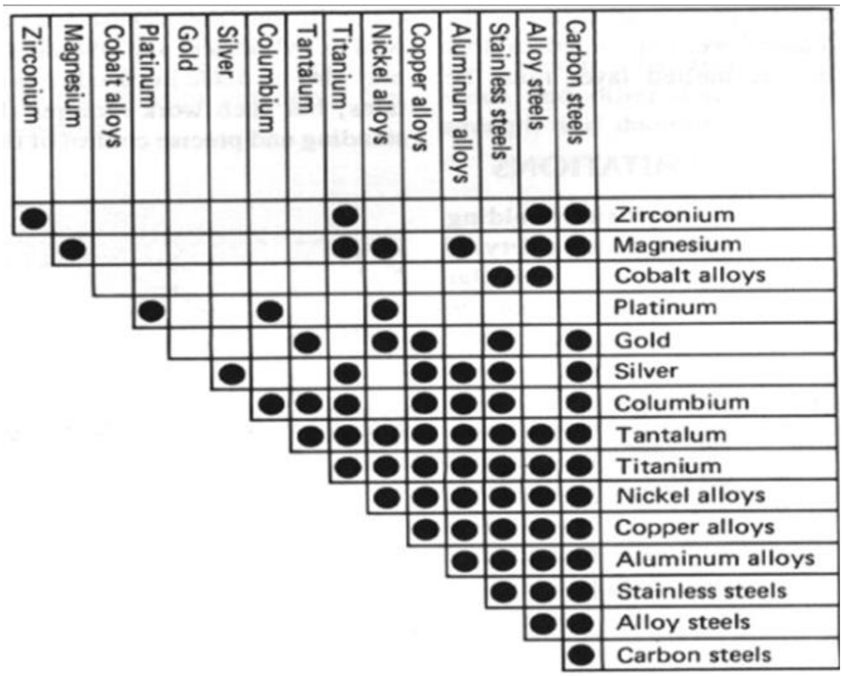

Zirconium	Magnesium	Cobalt alloys	Platinum	Gold	Silver	Columbium	Tantalum	Titanium	Nickel alloys	Copper alloys	Aluminum alloys	Stainless steels	Alloy steels	Carbon steels	
●								●					●	●	Zirconium
	●							●	●		●		●	●	Magnesium
												●	●		Cobalt alloys
			●			●			●						Platinum
							●		●	●		●		●	Gold
					●			●		●	●	●		●	Silver
						●	●	●		●	●	●		●	Columbium
							●	●	●	●	●	●	●	●	Tantalum
								●	●	●	●	●	●	●	Titanium
									●	●	●	●	●	●	Nickel alloys
										●	●	●	●	●	Copper alloys
											●	●	●	●	Aluminum alloys
												●	●	●	Stainless steels
													●	●	Alloy steels
														●	Carbon steels

***Fig. 2** Possible combination of materials*

The quality of the joints is usually assessed by ultrasonic defectoscopy, optical microscopy, microhardness measurement, EDX microanalysis and EBSD analysis.

2. *SITUATION OF WELDED MATERIALS*

Two basic ways of situating welded materials are known:

1.Angular and
2.Parallel (Fig. 3)

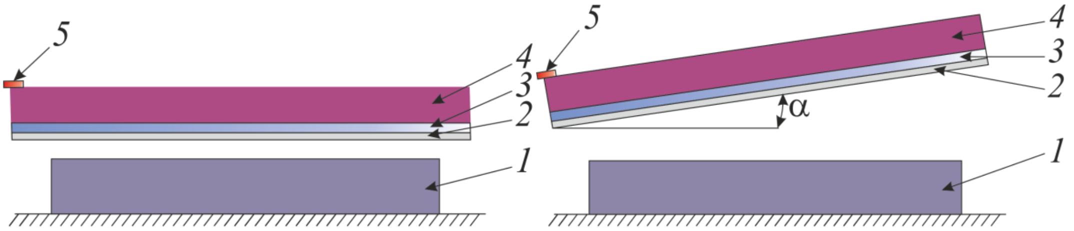

Fig.3. *Schematic of anglular and paralel positioning of welded materials, 1-stable material, 2- matarial to be accelerated, 3-protective interlayer, 4- explosive, 5-detonator, α- angle of adjustement*

In the angular positioning of welded materials, the material to be accelerated **2** is placed above the base stable material **1** at a certain setting angle. The explosive **4** is distributed in a uniforrm layer over ther entire surface of the accelerated metalic material and is initiated by a detonator which is positioned at the nearer end of the peak **α**. If the surface of the material to be accelerated needs to be protected from the effect of the detonation explosive, an intermediate layer 3 is inserted between the explosive and the material to be accelerated. The positioning of the materials prior to cladding is less demanding in this method because the explosive in the frame is similarly distributed over the sufrace of the accelerated material

3.FABRICATION OF BI (TRI) METALS

In the technological processing of metals by explosion, stable and accelerated metals are joined by the action of pressure arising from the detonation of a suitable explosive placed over the entire surface of the accelerated metal. As a result of high pressure, the welded materials are brought closer to the distance of their lattice parameters, creating the action of interatomic forces [6]. Of the two welded metals, one is usually stable, while the other is accelerated by the pressure of the gases of the detonating explosive. When welding with explosives, high pressure is created due to the high temperature and large amount of gases, and the reaction time is very short, 10^{-3} s to 10^{-4} s [7,8].

Fig. 5. Parallel welding set up

Fig. 6. Al - austenitic CrNi steel bimetal

Overlapped weld joints can also be made by explosion welding. In this case too, the main essence of the joint formation is the impact of the accelerated metal on the base metal at a suitable angle of the so-called bevel, which causes the formation of a jet at the bevel point. The jet ("Jet effect") cleans the surfaces of the welded metals. The high pressure causes the two metals to be joined in a solid state. The detonation velocity $\mathbf{v_d}$, the velocity of the accelerated metal $\mathbf{v_0}$ and the dynamic bevel angle are also in a mutual geometric relationship in this case. The flight velocity and the dynamic bevel angle are important parameters that most influence the welding process [3]. When making overlapped joints by explosion, an explosive charge of PETN (10 g/m) is used in the shape shown in Fig. 5 [9]. The initiation explosive and point of initiation was selected in such a manner that the movement direction of detonation wave front would be identical with the detonation velocity of explosive. As an example the fabricated bimetal Al-CrNi steel is shown in Fig. 6 with the final dimension 146 x 116 mm.. As initiation explosive Semtex 10SE was used, which was initiated with an electronic detonator. The distance spacing *h* and the charge parameters were designed on the basis of calculation, which authors were the specialists from VÚPCH Pardubice. Bimetal thickness was on the fringes reduced from 12 to 14 mm. The thickness in the central part was 16 mm.

4.PHYSICAL ASPECTS OF EXPLOSION WELDING

Explosion welding is a solids-state process that produces a high velocity interaction of dissimilar materials by a controlled detonation. Oxides found on the surface of welded materials must be removed by efacement or dispersion. Surface of both metal must come into intimate contact to achieve metallic bond. There several advantages of this process:

a) *no heat affected zone (HAZ),*
b) *only minor melting,*
c) *material melting temperatures and coefficients of thermal expansion differences do not affect the final product.*
d) *can bond many dissimilar, normally unweldable metals*
e) *minimum fixturing/jigs.*
f) *Simplicity of the process.*
g) *extremely large surfaces can be bonded.*
h) *wide range of thicknesses can be explosively clad together.*
i) *no effect on parent properties.*
j) *small quantity of explosive used*

There are also some limitations as for this type of welding:

1.The metals must have high enough impact resistance, and ductility
2.Noise and blast can require operator protection
3.The use of explosives in industrial areas will be restricted by the noise and ground vibrations caused by the explosion
4.The geometries welded must be simple – flat, cylindrical

The shock front compresses and heats the explosive materials which exceeds the sonic velocity of undetonated explosive. During the welding process the base component remains stationary and supported by anvil, and finaly will be joined to cladder. Cladding material is a thin plate in direct contact with explosive and can be shielded by the flying plate. Between the welded materials must be a standoff distance. Before the welded process begins one has to take into account the **bond window that includes velocity, dynamic bent and standoff that result** in successful weld and bonding operation, i.e. detonation of explosive that result in a weld. In the explosion process the cladder material can be placed either parallel or inclined to the base plate. Explosive material is distributed over top of the cladder material. Upon detonation, cladder plate collides with base plate to form weld. Explosive materials used in this proceess can be either high explosive materials (4490-7600 m/s, e.g. Semtex, TNT), or mid-low explosive (1493-4000 m/s, e.g. ammonium nitrate(V), ammonium chlorate(VII)). There are three types of detonation wave that result in good weld :

1. *shock wave develops if sonic velocity is greater than 120% of material sonic velocity (type 1),*
2. *detached shock wave results when detonation velocity is between 100-120% of materials sonic velocity (type 2),*
3. *no shock wave is produced if detonation velocity is less than material sonic velocity (type 3).*

Assuring the good weld one must take into account that detonation velocity is function of the explosive type, composition of the explosive, thickness of the explosive layer. Almost any metal with sufficient strength and ductility can be welded in this way. Explosion welding can be applied to large areas of metals, can weld outside or inside surfaces of pipes, e.g. Chemical Processing, Petroleum Refining, Hydrometallurgy, Aluminum Smelting Shipbuilding, Electrochemical, Oil & Gas, Power Generation, Cryogenic Processing, Pulp & Paper

5.METHODS OF EVALUATION OF WELDED JOINTS QUALITY

In our rapidly expanding technology, scientist and engineers are often required to observe and correctly explain phenomena occuring on a micrometer and submicrometer scale, i.e.nanoscale. One assumes the number of the methods currently used exceeds 100. Electron scanning microscope(SEM) and Electron probe microanalzyer(EPMA) are two powerfull equipments enabling to characterize heterogeneous materials on a such fine scale. Types of signals produced when the electron beam falls upon the sample comprise various signals such as secondary electrons, backscattered eletrons, characteristic X- rays, Auger electrons and photons of various energies.

6.EDX ANALYSIS

In the electron probe microanalyzer(often known as an electron microprobe) the primary signal of our interest is the characteristic X-rays which is emitted as a result of bombardment of the sample by electrons. Analysis of the characteristic X-rays which is emitted from the area where the electron probe falls upon the sample povides compositional information of both quali -and quanti-tative character. In all cases one may find compositional and topographical pictures of samples together with the concentration profiles along the welding zone and element distribution over that surface (Fig. 7).

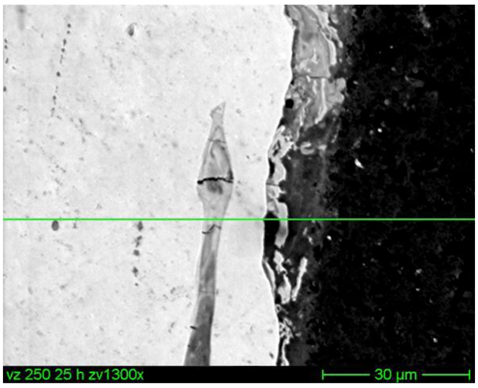

Fig. 7 *Concentration line profile using EDX analysis*

7. 2 EBSD ANALYSIS

Electron Backscattered Diffraction (EBSD) is a technique which allows crystallographic information to be obtained from samples in the scanning electron microscope (SEM). In EBSD a stationary electron beam strikes a tilted crystalline sample and the diffracted electrons form a pattern on a fluorescent screen. This pattern is characteristic of the crystal structure and orientation of the sample region from which it was generated. The diffraction pattern can be used to measure the crystal orientation, measure grain boundary misorientations, discriminate between different materials, and provide information about local crystalline perfection. When the beam is scanned in a grid across a polycrystalline sample and the crystal orientation measured at each point, the resulting map will reveal the constituent grain morphology, orientations, and boundaries. This data can also be used to show the preferred crystal orientations (texture) present in the material. A complete and quantitative representation of the sample microstructure can be established with EBSD. In the last ten years EBSD has become a well established technique for the SEM, and obtaining crystallographic information from samples is now both routine and easy. This scattering forms a divergent source of electrons close to the surface of the sample, and some of these electrons are incident on atomic lattice planes at angles which satisfy the Bragg equation(1):

$$\mathbf{n\lambda = 2d\sin\theta} \quad \mathbf{(1)}$$

where $\mathbf{n}$ is an integer, $\boldsymbol{\lambda}$ is the wavelength of the electrons, $\mathbf{d}$ is the spacing of the diffracting plane, and θ the angle of incidence of the electrons on the diffracting plane. These electrons are diffracted to form a set of paired large-angle cones that correspond to each diffracting plane, such as the green and blue cones in the image above, corresponding to a single (110) lattice plane (red disc). The image produced on the EBSD detector (usually using a phosphor screen to convert the electrons to light) contains characteristic Kikuchi bands (Fig. 8) which are formed where the regions of enhanced electron intensity intersect the screen, as shown both in the schematic image and the example EBSD pattern (left). The pattern imaged by the EBSD detector is a gnomonic projection of the diffracted cone, making the band edges appear hyperbolic.

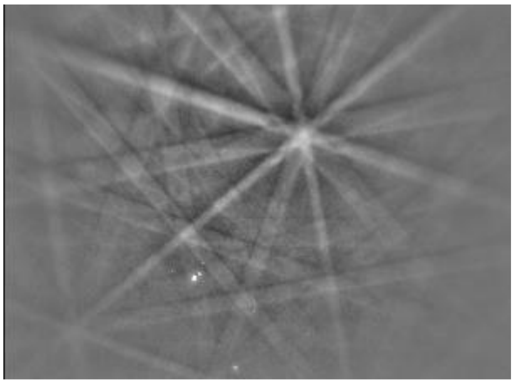

Fig. 8 *EBSP attained from Al 99.5*

8. CONCLUSIONS

The aim of this paper was to present possibilities and application of explosion welding, its advantages and limits. The authors also presented part of their long term studies performed on several bi(tri)mertals. Also, some methods for evaluating the quality of welded joints were pointed out. EDX microanalyses of boundary zones (line analyses of individual elements of welded metals) was applied to evaluate the quality of joints. EBSD analyses of boundaries in some bimetals showed that the structural situation in the boundary zone tends to converge to amorphous states of metals participating in the welding process .It is supposed that the mentioned bimetals can play a significant role in the field of construction of vacuum equipment for special technological processes and for other industrial fields. It can be stated that the fabricated welded joints (bimetals) exert a good quality, both from the viewpoint of their mechanical properties and the structural stability as well.

ACKNOWLEDGMENTS

The contribution was prepared under the support of GA VEGA MŠ SR and SAV project No. 1/0436/23

References

[1] TURŇA, M. Špeciálne metódy zvárania. Bratislava: ALFA, 1989. ISBN 80-05 00097-9.

[2] CHLÁDEK, L., NĚMEČEK, J., VACEK, J.: Výbuchové svařování kovů a příbuzné procesy. Praha 1979.

[3] YOUNG, G.: Explosion Welding, Technical Develompment and Historical Comercional Application [online]. 2009. [cit. 2009-01-22].

[4] EXPLOSIA a.s. firemné stránky. [online], 2008. [cit. 2008-01-13], Dostupné na internete: http://www.explosia.cz

[5] BRIEN A.O. Welding Handbook. 9th ed.,Volume 3 Welding Processes, Part 2. Miami : AWS, 2007. 303 p. ISBN 978-0-87171-053-6

[6] TNO Prins Maurits Laboratory: Defence Research and Explosive Processing of Materials [online]. Holland (Lisse): EPNM, 2008 [cit. 2009-11-01

[7] BUSCHOW, K. H. a kol.: Encyclopedia of Materials Science and Technology. vol. 5. Kidlington (UK): Oxford Elsevier, 2001. s. 4338. ISBN 0-08-043152-6

[8] UHENG L., DEMING S., TUNCER M. K. Explosion Bonding of Dissimilar Materials for Fabricating APS Front End Components [online]. 2009 [cit. 2009-11 01]. Dostupné na internete: http://www.aps.anl.gov/Facility 2005.

[9] MATSUI, Y., OTSUKA M., HINATA T., CARTON, E., ITOH, S. Explosive Welding of Light Weight Metal Sheets. In 8th International LS-DYNA Users Conference [online]. 2005 [cit. 2005-03-01], pp. 59-66. Dostupné na internete: < http://www.dynalook.com/international-conf-2004/08-5.pdf >.

29th International Seminar of Ph.D. Students
SEMDOK 2026
Western Tatras – Zuberec, Slovak Republic
February, 4 to February 6, 2026

DESIGNING OF EXPERIMENTAL TEST SETUP FOR STRESS CORROSION CRACKING OF ADDITIVELY MANUFACTURED MATERIALS

Matúš Murín[1,2*], Filip Osička[3,4], Marek Doubrava[4], Simona Hutařová[4], Michal Jambor[3], Libor Trško[2,5]

[1]*Faculty of Electrical Engineering and Information Technology, University of Žilina, Univerzitná 8215/1, 010 26 Žilina, Slovak Republic*
[2]*Research Centre of the University of Žilina, Univerzitná 8215/1, 010 26 Žilina, Slovak Republic*
[3]*Institute of Physics of Materials, Czech Academy of Sciences, Zizkova 22, Brno, Czech Republic*
[4]*Institute of Materials Science and Engineering, Faculty of Mechanical Engineering, Brno University of Technology, Technická 2896/2, 616 69 Brno, Czech Republic*
[5]*VSB-TU Ostrava, CPIT – Centre for Advanced Innovation Technologies, 17. listopadu 2172/15, 708 00 Ostrava, Czech Republic*
**Corresponding author: matus.murin@feit.uniza.sk, Tel. 0944 938 054, Univerzitná 8215/1, 010 26 Žilina, Slovak Republic*

1. Introduction

Stress corrosion cracking (SCC) is a highly specific degradation mechanism that occurs only when several conditions are met such as a material with a susceptible chemical composition, the presence of tensile stress (applied or residual), and an aggressive environment [1, 2]. SCC is dangerous and difficult to detect, and it can lead to sudden and catastrophic material failure even under stresses well below the yield strength. In recent years, several experimental setups have been developed to evaluate the susceptibility of materials to SCC. The most common approach uses U-bend specimens – samples cut from metal sheets and bent into a U-shape, where the outer-surface strain is calculated. A droplet of saturated chloride solution is then applied to the surface, and the specimens are exposed in climatic chambers under controlled temperature and humidity [3-5]. In other study, Ornek et al. [6] chose different approach and designed a miniature tensile fixture for SCC testing. The deformation of the specimen was measured using a strain gauge, and droplets of salt solution were deposited on the surface before placing the entire setup inside a climatic chamber. Spencer et al.[7] proposed a similar configuration, using self-made test jigs in which a compression spring applied the load. The final curvature of the specimen was measured with a differential variable reluctance transducer to achieve the required bending moment and corresponding surface stress.

Austenitic stainless steels are among the most susceptible materials to SCC. Despite this, they are widely used in many industrial applications due to their favourable properties, including high ductility, excellent corrosion resistance, good weldability, and overall manufacturability. These steels are commonly utilized in nuclear and conventional power plants, as well as in the food and chemical industries, thanks to their durability and health-safe characteristics [8, 9]. However, SCC remains one of the most critical degradation mechanisms leading to failures in components made from austenitic stainless steels. Numerous studies have investigated their susceptibility to SCC [10, 11]. For example, Prosek et al. [3] carried out extensive research summarizing specific conditions – such as:

temperature, relative humidity, and chloride ion concentration – under which SCC or pitting corrosion occurs in various stainless steel grades. Thanks to their contribution next research can be performed, because their results and conclusions can be considered as referential values for next experiments. Nowadays additive manufacturing has become increasingly popular due to its efficiency and time-saving potential. Nevertheless, additively manufactured materials often exhibit different properties compared to conventionally produced materials [12, 13]. Therefore, it is important to investigate properties of such materials and in the case of austenitic stainless steels, this includes verifying their resistance to SCC. Given these facts, there is a clear need to design reliable and reproducible experimental methods for evaluating SCC susceptibility in additively manufactured materials. For this reason, the present work focuses on developing an experimental test setup specifically tailored to study the relation between microstructure characteristics and SCC susceptibility in additively manufactured austenitic stainless steels.

2. Design of experimental test setup

As a first step in this study, it was necessary to design an appropriate fixture for loading the specimens for SCC testing. The main purpose was to investigate the resistance to SCC of additively manufactured stainless steel and compare it with the performance of conventional stainless steel. Therefore, the fixture design had to be adapted for additively manufactured specimens, as their size and shape had to be constrained for economic reasons. Fig.1 presents the final design of the fixture for SCC testing. Sheet metal specimens with a width of 20 mm and a length of 45 mm are subjected to four-point bending in a fixture made of stainless steel, using a loading screw.

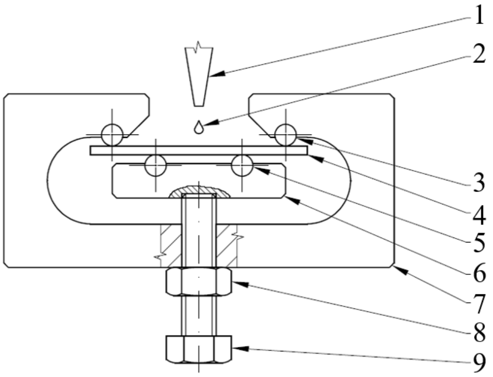

Fig. 1 *Drawing of the fixture for four point bending SCC tests (1-Pipette, 2-Droplet, 3-Support pin, 4-Specimen, 5-Loading pin, 6-Pressing plate, 7-Frame, 8-Locking nut, 9-Loading screw)*

Before the specimen is placed in the loading fixture, the surface in the region of highest stress is electrochemically polished to allow observation of the microstructure and any cracks after testing. The bent displacement of the gauge length is measured with a digital dial indicator. The corresponding surface stresses were previously calibrated using strain-gauge measurements (Fig. 2). For the calibration, material constants of conventionally manufactured 304 stainless steel were used. This calibration eliminates the need to measure the surface stress using strain-gauge measurements for every specimen, as the required tensile stress can be determined directly from the final curvature measured by the digital dial indicator. For the first experiments, three specimens of AISI 304 stainless-steel were used: a conventional and an additively manufactured cold-sprayed specimen in the as-built condition and after heat treatment (900°C/1h). A displacement of 0.2 mm was applied, resulting in a tensile stress of 146 MPa.

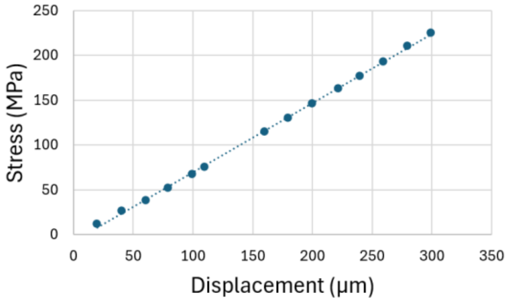

Fig. 2 *Displacement vs. stress calibration of the SCC fixtures*

After loading the specimen to induce SCC, it must be exposed to an aggressive chloride environment. This can be achieved either by boiling the entire specimen in a saturated chloride solution or by applying a droplet of saturated chloride solution to the specimen surface [3, 14]. On the central part of the loaded shim a 5 µl droplet of 1M $MgCl_2$ was created with a micropipette. The diameter of the initial droplet Fig. 3a was 2.7 mm, however after breaking the surface tension during the test, the liquid covered a circle with diameter of approx. 4.2 mm (Fig. 3b). This resulted in Chlorine exposure of 2.6×10^{-5} g□mm^{-2}. Consequently, the fixtures are inserted in a climate chamber set up to certain temperature and relative humidity. For initial experiments, the samples were exposed to temperature of 50 °C and 35% relative humidity. The total test duration was 45 days after which the specimens were released from the fixtures and the $MgCl_2$ deposition was cleaned with citric acid and alcohol.

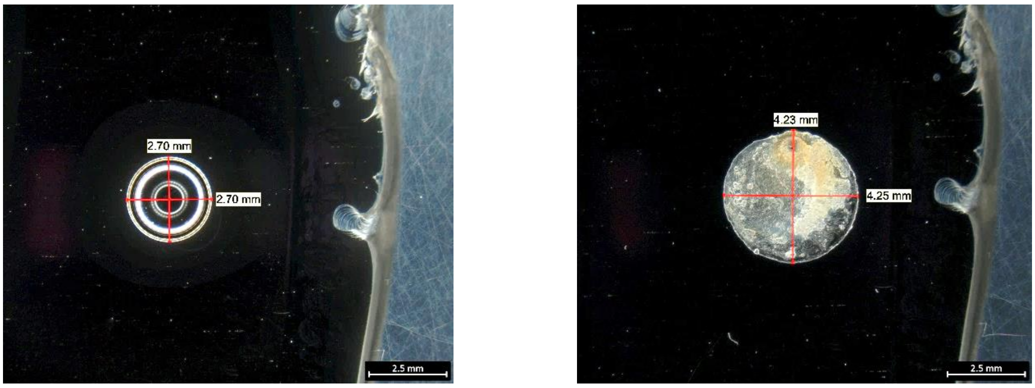

a) Initial droplet
b) Droplet after breaking surface tension

Fig. 3 *Droplet of 1M solution of* $MgCl_2$

Based on the literature, the main criteria to evaluate the resistance of the material to SCC is the total length of the cracks combined in selected area. Different rules for SCC evaluation and crack counting in selected areas have been introduced in the literature, depending on the material, as each material exhibits different SCC resistance. For example, Zhang et al. [2] was counting cracks in conventional AISI 304 samples while micro-cracks shorter than 50 µm were excluded and micro-cracks originating from main cracks were classified as crack branches and therefore not counted. Afterwards, the crack density was calculated as the total crack length per unit area (µm/mm^{2}). In the first experiments, due to the breakup of the chloride droplet during exposure, it was not possible to define a unique evaluation area. Therefore, the initial results are presented only as the total length of all cracks formed on the specimens. The area subjected to chlorides was observed by scanning electron microscopy and the total length of the cracks was measured and counted. To avoid ambiguity in distinguishing short cracks from discontinuities on the grain boundaries in the cold sprayed samples, only cracks longer than 300 µm were considered.

3. Experimental results and discussion

In the conventionally manufactured AISI 304 stainless steel (Fig. 4a), only one SCC crack was present in the exposed area with length of 1.58 mm. In detail observation of the crack revealed that the propagation path was neither fully transcrystalline nor intercrystallite. In the as-built condition of the material contained in total 7 cracks with cumulative length of 7.01 mm (Fig. 4b). In detail crack observation was unable to reveal the microstructure relationship with the crack propagation path as the cold sprayed microstructure is highly deformed and does not possess a typical polyhedral microstructure. However, it can be observed that the crack in certain locations propagated through the intergranular discontinuities frequently present in the microstructure. After heat treatment (Fig. 4c), only two cracks were present with cumulative length of 5.9 mm, and both were deviated for approximately 20° from the direction of the maximal tensile loading. Due to the partial microstructure recovery caused by the heat treatment, the in-detail crack path analysis revealed that cracks were propagating through both, grain volume and grain boundaries.

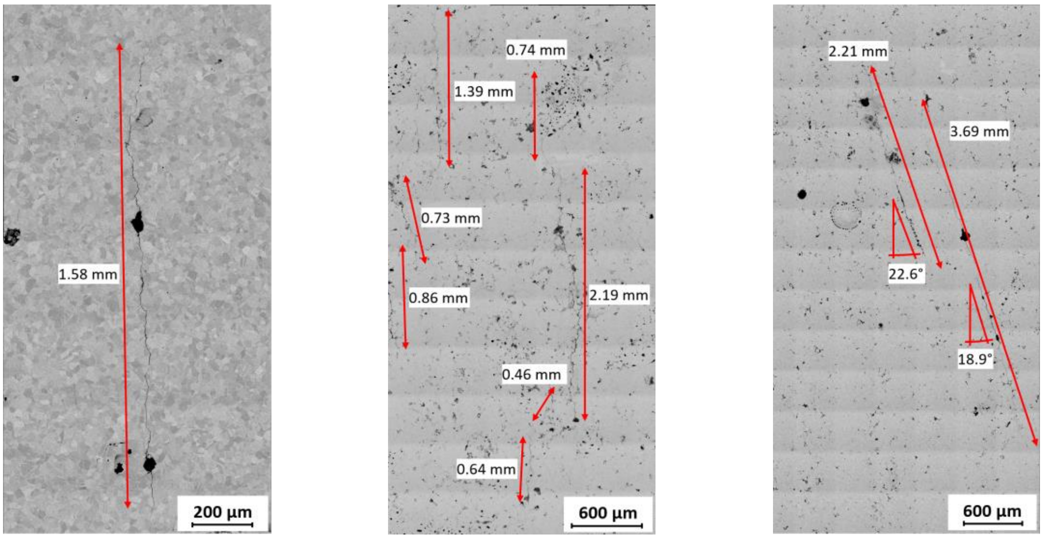

(a) *(b)* *(c)*

Fig. 4 *Evaluation of the stress corrosion cracks in conventional (a), as-built additively manufactured (b) and heat treated additively manufactured (c) AISI 304 stainless steel.*

Manufacturing the AISI 304 stainless steel via cold spray coating technology caused higher susceptibility of the material to stress corrosion cracking. The reason lies most likely in the microstructure heterogeneity, bonding discontinuities and expected higher values of residual stresses as a result of the high velocity deposition process. In the as-built condition, material contained highest number of cracks among all the tested specimens. Even when the following heat treatment of the material was able to cause material recovery and partial recrystallization to a typical polyhedral microstructure, the resistance to stress corrosion cracking was not significantly improved. The total number of cracks decreased to two, but their cumulative length was very close to the as-built condition while the conventional material showed much superior SCC resistance. It is important to note that the SCC tests were performed with constant strain loading. This means that crack formation reduces the loading stress thus decreasing the energy for crack initiation and propagation and at a certain point it reaches the threshold value, where no new cracks are formed and the existing ones stop to propagate. Therefore, prolonging the test duration would most likely not emphasize the difference in the material properties but possibly end up by identical cumulative crack length.

4. Conclusions

The main purpose of this study was to design experimental test setup for stress corrosion cracking of additively manufactured materials. The self-made fixture was developed for loading additively manufactured specimens, and initial experiments were subsequently performed. The first results were obtained, and SCC-induced cracks were recorded in both conventional AISI 304 stainless steel and additively manufactured specimens. The results indicated that additively manufactured stainless steel produced by cold spraying exhibits significantly higher susceptibility to SCC, even after heat treatment. In conventional stainless steel, only a single SCC crack with a length of 1.58 mm was observed. In the as-built condition, a total of seven cracks with a cumulative length of 7.01 mm were detected, while in the heat-treated specimen, two cracks with a cumulative length of 5.9 mm were present. Nevertheless, further experiments are required to investigate how individual additive manufacturing parameters influence SCC resistance. In addition, several improvements to the experimental setup are necessary, for example to ensure the stability of the saturated chloride solution droplet, to define a well-defined area selectively exposed to chloride ions, and consequently to enable evaluation of SCC susceptibility based on crack density per unit area.

References

[1] S. Nuthalapati, K. E. Kee, S. R. Pedapati, and K. Jumbri, “A review of chloride induced stress corrosion cracking characterization in austenitic stainless steels using acoustic emission technique,” *Nuclear Engineering and Technology*, vol. 56, no. 2, pp. 688–706, Feb. 2024, doi: 10.1016/j.net.2023.11.005.

[2] W. Zhang, K. Fang, Y. Hu, S. Wang, and X. Wang, “Effect of machining-induced surface residual stress on initiation of stress corrosion cracking in 316 austenitic stainless steel,” *Corros Sci*, vol. 108, pp. 173–184, Jul. 2016, doi: 10.1016/j.corsci.2016.03.008.

[3] T. Prosek, A. Iversen, and C. Taxén, “Low Temperature Stress Corrosion Cracking of Stainless Steels in the Atmosphere in Presence of Chloride Deposits,” in *CORROSION 2008*, NACE International, Mar. 2008, pp. 1–17. doi: 10.5006/C2008-08484.

[4] W. N. L. W. Zakaria, K. E. Kee, and M. C. Ismail, “The effect of sensitization treatment on chloride induced stress corrosion cracking of 304L stainless steel using U-bend test,” *Mater Today Proc*, vol. 29, pp. 75–81, 2020, doi: 10.1016/j.matpr.2020.05.697.

[5] Z. Y. Liu *et al.*, “Field experiment of stress corrosion cracking behavior of high strength pipeline steels in typical soil environments,” *Constr Build Mater*, vol. 148, pp. 131–139, Sep. 2017, doi: 10.1016/j.conbuildmat.2017.05.058.

[6] C. Örnek and D. L. Engelberg, “Toward Understanding the Effects of Strain and Chloride Deposition Density on Atmospheric Chloride-Induced Stress Corrosion Cracking of Type 304 Austenitic Stainless Steel Under MgCl2 and FeCl3:MgCl2 Droplets,” *Corrosion*, vol. 75, no. 2, pp. 167–182, Feb. 2019, doi: 10.5006/3026.

[7] D. T. Spencer, M. R. Edwards, M. R. Wenman, C. Tsitsios, G. G. Scatigno, and P. R. Chard-Tuckey, “The initiation and propagation of chloride-induced transgranular stress-corrosion cracking (TGSCC) of 304L austenitic stainless steel under atmospheric conditions,” *Corros Sci*, vol. 88, pp. 76–88, Nov. 2014, doi: 10.1016/j.corsci.2014.07.017.

[8] D. Xu, X. Wan, J. Yu, G. Xu, and G. Li, “Effect of Cold Deformation on Microstructures and Mechanical Properties of Austenitic Stainless Steel,” *Metals (Basel)*, vol. 8, no. 7, p. 522, Jul. 2018, doi: 10.3390/met8070522.

[9] P. Dong, G. G. Scatigno, and M. R. Wenman, “Effect of Salt Composition and Microstructure on Stress Corrosion Cracking of 316L Austenitic Stainless Steel for Dry Storage Canisters,” *Journal of Nuclear Materials*, vol. 545, p. 152572, Mar. 2021, doi: 10.1016/j.jnucmat.2020.152572.

[10] G. G. Scatigno, M. P. Ryan, F. Giuliani, and M. R. Wenman, “The effect of prior cold work on the chloride stress corrosion cracking of 304L austenitic stainless steel under atmospheric conditions,” *Materials Science and Engineering: A*, vol. 668, pp. 20–29, Jun. 2016, doi: 10.1016/j.msea.2016.05.037.

[11] G. Hinds, L. Wickström, K. Mingard, and A. Turnbull, “Impact of surface condition on sulphide stress corrosion cracking of 316L stainless steel,” *Corros Sci*, vol. 71, pp. 43–52, Jun. 2013, doi: 10.1016/j.corsci.2013.02.002.

[12] H. Dai *et al.*, “Stress corrosion cracking behavior of 316 L manufactured by different additive manufacturing techniques in hydrofluoric acid vapor,” *J Mater Sci Technol*, vol. 191, pp. 33–48, Aug. 2024, doi: 10.1016/j.jmst.2023.12.041.

[13] X. Lou, M. Song, P. W. Emigh, M. A. Othon, and P. L. Andresen, “On the stress corrosion crack growth behaviour in high temperature water of 316L stainless steel made by laser powder bed fusion additive manufacturing,” *Corros Sci*, vol. 128, pp. 140–153, Nov. 2017, doi: 10.1016/j.corsci.2017.09.017.

[14] S. Pal, S. S. Bhadauria, and P. Kumar, “Studies on Stress Corrosion Cracking of F304 Stainless Steel in Boiling Magnesium Chloride Solution,” *J Bio Tribocorros*, vol. 7, no. 2, p. 62, Jun. 2021, doi: 10.1007/s40735-021-00498-4.

29th International Seminar of Ph.D. Students

SEMDOK 2026

Western Tatras – Zuberec, Slovak Republic
February, 4 to February 6, 2026

Structural and physicochemical characterization of single-layer TiO2 and ZnO and bilayer TiO2/ZnO and ZnO/TiO2 coatings deposited by ALD

Antonina Olszewska[1*], Weronika Smok[1], Anna Taratuta[2], Łukasz Reimann[1], Jakub Gwóźdź[3], Vladyslav Makar[3], Marcin Staszuk[1]

[1] *Silesian University of Technology, Faculty of Mechanical Technology, Gliwice, Poland*
[2] *Silesian University of Technology, Faculty of Biomedical Engineering, Zabrze, Poland*
[3] *Students of the 5th Secondary School named after Andrzej Struga in Gliwice, Górnych Wałów 29, 44-100 Gliwice, Poland*
**antonina.olszewska@polsl.pl, tel.: 32 237 26 0, address: Stanisława Konarskiego 18A, 44-100 Gliwice, Poland*

1. Introduction

Biomaterial-associated infections represent a major clinical challenge in modern implantology due to the dynamic development and increasing use of implantable medical devices. Their severity is further intensified by the rise of antibiotic resistance, classified by the WHO as one of the most critical global public health threats [1,2]. As a result, such complications negatively affect patient outcomes, prolong treatment and reduce implant lifetime.

One of the dominant mechanisms responsible for implant failure is biofilm formation on the surface of metallic implants, as the biofilm matrix protects microorganisms against immune response and antibiotic therapy [1]. Therefore, biomaterial surface modification strategies increasingly aim not only to ensure chemical and mechanical stability in physiological environments but also to introduce functional properties that inhibit microbial adhesion or promote self-sterilization [3]. Antimicrobial coatings may operate through ion release, contact-mediated inactivation, photocatalytic generation of reactive oxygen species (ROS) or anti-adhesion mechanisms, depending on the material and application environment [1,3].

Stainless steel 316L remains one of the most widely used metallic biomaterials for surgical and orthopedic implants due to its mechanical strength, durability and biocompatibility. However, despite its inherent passivity, the electrochemical stability of 316L may deteriorate in chloride-containing media, leading to localized pitting or crevice corrosion and ultimately compromising implant performance [4]. For this reason, the development of protective and functional thin films deposited on 316L steel is considered a promising approach to enhance surface stability in simulated physiological environments.

Metal oxide coatings, particularly TiO_2 and ZnO, have attracted considerable interest due to their chemical stability, biocompatibility and ROS generation capability. Technologies enabling precise control of coating thickness, composition and morphology – such as Atomic Layer Deposition (ALD) – therefore play an increasingly important role in biomedical surface engineering [4]. ALD offers atomic-scale thickness control, excellent uniformity and conformality, making it suitable for complex implant geometries.

This work investigates the structure and selected physicochemical properties of single-layer TiO_2 and ZnO coatings as well as double-layer TiO_2/ZnO and ZnO/TiO_2 coatings deposited by ALD on 316L stainless steel.

2.Materials and Methods

Disks of 316L stainless steel (Ø 10 mm, height 5 mm) were used as substrates. Surface preparation involved grinding and polishing followed by ultrasonic cleaning in a water–detergent solution to remove abrasive residues and contaminants.

Four oxide coating configurations were fabricated using Atomic Layer Deposition (ALD): TiO_2, ZnO, TiO_2/ZnO and ZnO/TiO_2. $TiCl_4$ and diethylzinc (DEZ) served as metal precursors with H_2O as the oxidizing reagent. Deposition was carried out at 200 °C under vacuum with high-purity nitrogen as the purge gas. The process parameters are summarized in Table 1. Silicon wafers were coated as reference samples for photocatalytic analysis.

Tab. 1 *ALD deposition parameters of the coating*

Parameter	***TiO_2***	***ZnO***
Process temperaturę	*200 °C*	*200 °C*
Numb of cycles	*2000*	*800*
Metal precursor	*$TiCl_4$*	*DEZ*
Oxidixing reagent	*H_2O*	*H_2O*
Precursor dosing time	*0,1 s*	*0,1 s*
Go time with inert gas	*4,5 s*	*6 s*

Surface morphology was examined using Scanning Electron Microscopy (SEM) and chemical composition was assessed using Energy-Dispersive X-ray Spectroscopy (EDS). Surface topography and roughness parameters were evaluated via Atomic Force Microscopy (AFM) in tapping mode.

Wettability was analyzed by static water contact angle measurements using the sessile drop method. Coating adhesion was evaluated using microscratch testing in accordance with PN-EN ISO 20502:2016-05.

Photocatalytic activity was examined based on the UV-induced degradation of methylene blue (5 ppm). Electrochemical characterization included open circuit potential (OCP) and potentiodynamic polarization with Tafel analysis. Tests were conducted in Ringer's solution at room temperature using coated samples and uncoated 316L steel as reference.

3. Results and Discussion

3.1 Surface morphology and chemical composition

SEM observations revealed a strong influence of both coating type and layer sequence on the microstructure. Single-layer ZnO exhibited a fine-grained and irregular morphology, whereas TiO_2 formed larger grains and a more uniform surface. In double-layer systems, the TiO_2/ZnO configuration resulted in reduced granularity and a denser structure compared to the more irregular ZnO/TiO_2 system, indicating that the layer sequence affects nucleation and growth behavior (Figure 1a).

EDS spectra confirmed the expected elemental composition for all coatings. In TiO_2 /ZnO, dominant Zn signals with trace Ti confirmed effective coverage of the underlying TiO_2 layer, while ZnO/TiO_2 displayed simultaneous signals from Zn, Ti and O, suggesting partial interdiffusion or nanoscale non-uniformity (Figure 1b).

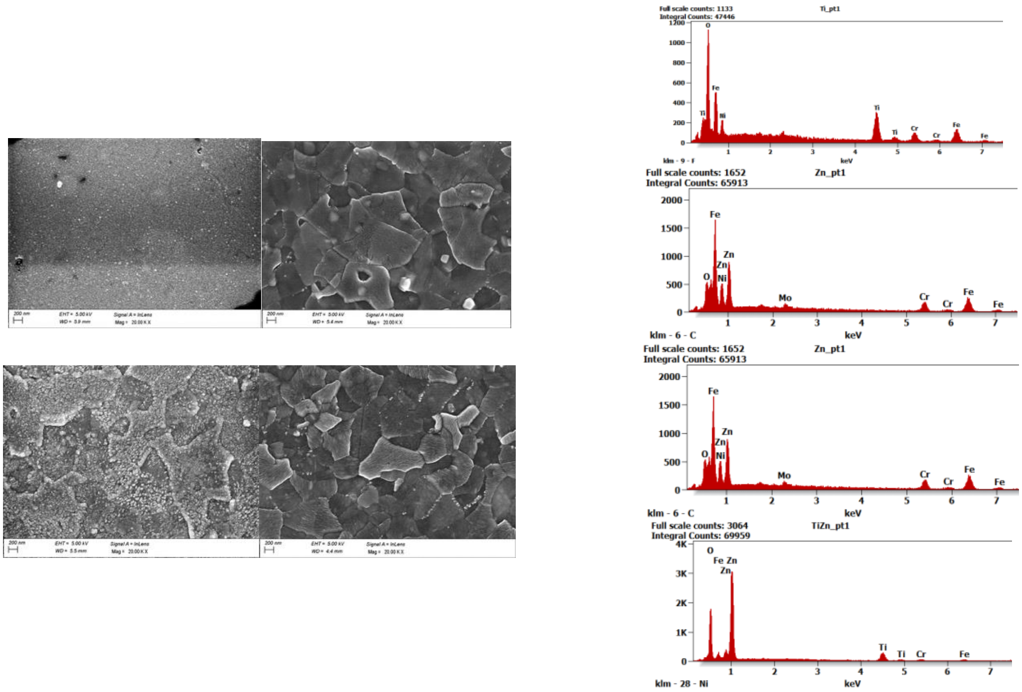

a) ZnO coating microstructure; TiO_2 coating microstructure; TiO_2 /ZnO coating microstructure; ZnO/TiO_2 coating microstructure — magnification 20Kx

b) EDS spectrum of the TiO_2 coating; EDS spectrum of the ZnO coating; EDS spectrum of the ZnO/TiO_2 coating; EDS spectrum of the TiO_2 /ZnO coating.

***Fig. 1** SEM microstructure a) and EDS spectra b)*

3.2 Surface topography

AFM analysis demonstrated distinct differences in surface topography. ZnO exhibited the highest roughness parameters (Ra, Rq, Rpv), whereas TiO_2 showed lower values and a more ordered height distribution. In double-layer coatings, TiO_2 /ZnO displayed moderate roughness and an ordered structure, while ZnO/TiO_2 exhibited pronounced granular features and the broadest height distribution range (Figure 2, Table 2).

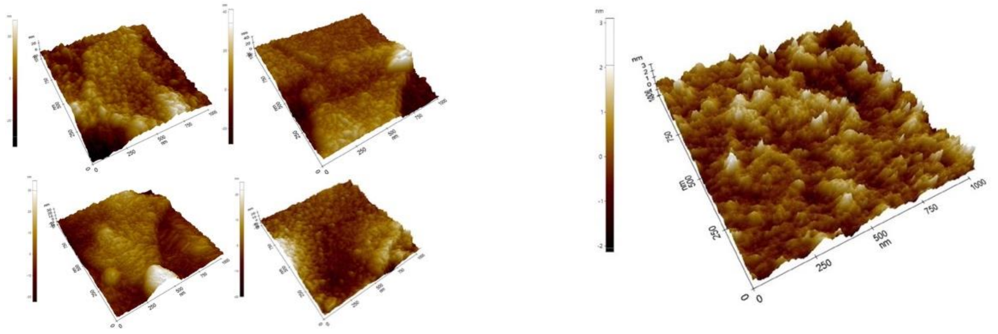

a) ZnO coating; TiO_2 /ZnO coating; ZnO/TiO_2 coating; TiO_2 coating

b) Surface topography image of the 316L stainless steel substrate

***Fig. 2** Surface topography image — 3D surface reconstruction (1000 × 2000 nm).*

***Tab. 2** Surface roughness parameters*

Sample	*Min (nm)*	*Max (nm)*	*Rpv (nm)*	*Rq (nm)*	*Ra (nm)*	*Rz (nm)*	*Rsk*	*Rku*
316L stainless	*–2,129*	*3,104*	*5,234*	*0,616*	*0,483*	*5,069*	*0,326*	*3,479*
TiO_2	*–20,047*	*24,785*	*44,833*	*5,724*	*4,420*	*43,525*	*0,611*	*3,779*
ZnO	*–32,505*	*27,721*	*60,226*	*8,057*	*6,195*	*59,626*	*0,388*	*4,129*
TiO_2 /ZnO	*–27,947*	*41,201*	*69,148*	*9,072*	*6,347*	*68,533*	*0,164*	*5,102*
ZnO/TiO_2	*–22,366*	*34,536*	*56,902*	*8,372*	*6,706*	*56,222*	*0,477*	*3,830*

3.3 Electrochemical performance

OCP measurements in Ringer's solution showed that TiO_2 /ZnO reached the highest and most stable potential (≈−0.07 V), suggesting enhanced passivation, while ZnO and ZnO/TiO_2 exhibited more negative potentials and local fluctuations. Single-layer TiO_2 displayed the lowest and least stable values (≈−0.36 V), indicating limited corrosion protection capability (Figure 3 a).

Potentiodynamic polarization and Tafel analysis confirmed the barrier function of oxide coatings, although performance varied with configuration (Table 3). Improvements were observed in selected parameters such as corrosion current density (Jcorr), corrosion potential (Ecorr) and polarization resistance (Rpol). No single system outperformed others across all metrics, indicating configuration-dependent trade-offs.

Post-corrosion SEM analysis (Figure 3 b) revealed surface degradation in all oxide systems. TiO_2 top layers exhibited cracking, crater formation and partial delamination, while ZnO top layers showed microporosity, erosion and flaking without complete detachment. Residual TiO_2 grains in TiO_2 /ZnO indicated partial retention of barrier functionality.

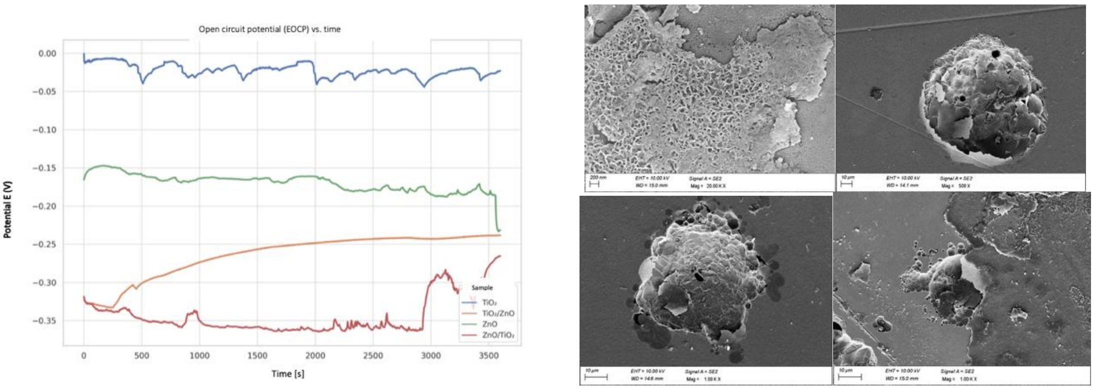

a) OCP response recorded in Ringer's solution for TiO_2 , ZnO, TiO_2 /ZnO and ZnO/TiO_2 coatings deposited on 316L stainless steel.

b) ZnO coating microstructure, ZnO/TiO_2 coating microstructure, TiO_2 coating and TiO_2 /ZnO coating microstructure - after electrochemical testing

Fig. 3 *OCP response in Ringer's solution and SEM micrographs after corrosion test*

Tab.3 *Tafel analysis result*

sample	*Jcorr [μA/cm²]*	*Ba [V]*	*Bc [V]*	*Ecorr [V]*	*Rpol [kΩ·cm²]*
316L	*0,000802*	*0,404*	*0,069*	*-0,072*	*31900*
ZnO/TiO₂	*0,0406*	*0,338*	*0,019*	*-0,317*	*19*
ZnO	*0,0863*	*0,790*	*0,057*	*-0,267*	*269*
TiO₂ /ZnO	*0,0160*	*0,817*	*0,043*	*-0,347*	*112*
TiO₂	*0,0556*	*0,184*	*0,072*	*-0,070*	*40300*

4. Conclusions

1. ALD enabled the fabrication of single-layer (TiO_2 , ZnO) and double-layer (TiO_2 /ZnO, ZnO/TiO_2) oxide coatings on 316L stainless steel with controlled microstructure and chemical composition.
2. The surface morphology and wettability strongly depended on the external oxide layer, with ZnO exhibiting the highest roughness and contact angle values.
3. Electrochemical tests in Ringer's solution confirmed improved corrosion protection for coated samples compared to bare 316L steel, with the ZnO/TiO_2 configuration showing the most favorable barrier performance.
4. No significant photocatalytic activity was observed for the ALD coatings under the applied test conditions, indicating the need for further optimization of the oxide architecture.

Acknowledgments

This work was produced as part of the project implemented within the framework of project-oriented education - PBL project implemented with secondary school students, in the VI competition under the Excellence Initiative - Research University program, at the Silesian University of Technology.

References

[1] D. Nazarov, I. Ezhov, N. Yudintceva, M. Shevtsov, A. Rudakova, V. Kalgonov, V. Tolmachrv, Y. Zharova, O. Lutakov, L. Kraeva, E. Rogocheva i M. Maximov, „Antibactirial and Osteogenic Properties of Ag Nanoparticles and Ag/TiO2 Nanostructures Prepared by Atomic Layer Deposition," *J.Funct.Biomater,* tom 13, nr 66, pp. 1-16, 2022.

[2] „Antybiotykooporność: zagrożenia dla zdrowia publicznego - materiał prasowy EDWA i ŚTWA," Narodowy Program Ochrony Antybiotyków, 2016.

[3] A. Rabajczyk, M. Zielecka, W. Klapsa i A. Dziechciaż, „Self-Cleaning Coating and Surfaces of Modern Building Materials for the Removal of Some Air Pollutants," *Materials,* tom 14, nr 2161, pp. 1-13, 2021.

[4] A. Giedriaitine, M. Rauzuskas, R. Siugzdiniene, S. Tuckute, K. Grigonis i D. Milcius, „ZnO Nanoparticles Enhance the Antimicrobial Properties of Two - Sided - Coated Cotton Textile," *Nanomaterials,* tom 1264, nr 12, pp. 1-11, 2024.

29th International Seminar of Ph.D. Students
SEMDOK 2026
Western Tatras – Zuberec, Slovak Republic
February, 4 to February 6, 2026

ZMENA VLASTNOSTÍ AUSTENITICKEJ OCELE AISI 304 PO PLASTICKEJ DEFORMÁCII TLAKOM

Martin Slezák[1*], Peter Palček[1], Milan Uhríčik[1], Melisa Šnircová[1], Edita Illichmanová[1], Silvia Hudecová[1], Kamila Hrabovská[2]

[1]Strojnícka fakulta, Katedra materiálového inžinierstva, Žilinská univerzita v Žiline, Univerzitná 8215/1, 010 26 Žilina, Slovenská republika

[2]Fakulta elektrotechniky a informatiky, Katedra fyziky, VŠB – Technická univerzita Ostrava, 17. listopadu 2172/15, 708 00 Ostrava-Poruba, Česká republika

**martin.slezak@fstroj.uniza.sk, +421 41 513 2632, Strojnícka fakulta, Katedra materiálového inžinierstva, Žilinská univerzita v Žiline, Univerzitná 8215/1, 010 26 Žilina, Slovenská republika*

1. Úvod

Nehrdzavejúce ocele sú železné zliatiny s obsahom minimálne 10,5 % chrómu, ktoré sa vyznačujú priaznivou kombináciou mechanických vlastností a vysokej koróznej odolnosti. Podľa kryštalografickej štruktúry pri izbovej teplote sa rozlišujú na austenitické, feritické, duplexné, martenzitické a precipitáciou tvrdené ocele. Austenitické nehrdzavejúce ocele majú medzi nimi dominantné postavenie vďaka dobrej koróznej odolnosti, zvariteľnosti a tvárnosti, čo umožňuje ich široké využitie v konštrukčne náročných priemyselných aplikáciách [1]. Typickým zástupcom je oceľ AISI 304, ktorá patrí medzi metastabilné austenitické zliatiny. Pri plastickej deformácii môže u nej dochádzať k deformačne indukovanej martenzitickej transformácii, vedúcej k zvýšeniu pevnosti pri zachovaní tvárnosti (TRIP efekt). Keďže austenitické ocele nie je možné spevňovať tepelným spracovaním, ich spevnenie je primárne dosahované plastickou deformáciou spojenou s nízkou energiou chyby vrstvenia a tvorbou martenzitu [2, 3]. Austenitické nehrdzavejúce ocele sú za normálnych podmienok paramagnetické, avšak intenzívna plastická deformácia môže ich magnetické správanie výrazne modifikovať. V metastabilnej oceli AISI 304 deformácia podporuje vznik deformačne indukovaného α′-martenzitu, ktorý je feromagnetický a vedie k nárastu magnetickej odozvy [4–6].

Súčasne dochádza k zvýšeniu hustoty dislokácií, ktoré ovplyvňujú magnetické aj elektrické vlastnosti materiálu prostredníctvom lokálnych napäťových polí a interakcie s magnetickými doménami [4–6]. Experimentálne štúdie ukazujú, že rastúca deformácia alebo únavové poškodenie sú spojené s poklesom elektrickej vodivosti a zosilnením magnetickej odozvy, pričom rozhodujúcu úlohu zohráva kombinovaný účinok dislokácií a martenzitickej transformácie [5–7].

2. Experimentálny materiál a metodika experimentov

Na tento experiment bola použitá austenitická nehrdzavejúca oceľ AISI 304. Materiál bol dodaný vo forme kruhových tyčí s dĺžkou 3000 mm a priemerom 12 mm. Z týchto tyčí boli mechanickým rezaním pripravené valcové skúšobné vzorky s výškou 15 mm a priemerom 12 mm. Následne bola na pripravených vzorkách vykonaná chemická analýza pomocou emisného iskrového spektrometra SPECTROMAXx za účelom overenia ich chemického zloženia. Priemerné hodnoty piatich meraní sú uvedené v Tab. 1. S cieľom získať ideálny referenčný stav pred realizáciou experimentálnych postupov bolo na austenitickej nehrdzavejúcej oceli AISI 304 vykonané rozpúšťacie žíhanie (RZ). Tepelné spracovanie bolo realizované v spoločnosti Rübig SK. Pred samotným procesom boli vzorky očistené izopropylalkoholom a následne vložené do pece. Rozpúšťacie žíhanie prebiehalo pri teplote 1030 °C po dobu 30 minút vo vákuovej atmosfére. Po uplynutí výdrže boli vzorky rýchlo ochladené pomocou plynného dusíka, čím sa zabezpečilo zachovanie austenitickej mikroštruktúry.

Tab. 3 *Chemické zloženie experimentálneho materiálu*

Typ ocele	***Koncentrácia chemických prvkov [hmot. %]***									
	C	***Cr***	***Ni***	***Mn***	***Si***	***Mo***	***S***	***P***	***N***	***Fe***
AISI 304	*0,02*	*18,87*	*8,18*	*1,35*	*0,40*	*0,40*	*0,03*	*0,03*	*0,08*	*zv.*

Po rozpúšťacom žíhaní sa vykonala hlavná časť experimentu. V tomto kroku boli vzorky vystavené plastickej deformácii tlakom. Aplikované zaťaženie sa pohybovalo v rozsahu od 5 do 25 ton, pričom každá nasledujúca vzorka bola deformovaná pri postupne vyššom zaťažení so stupňom 5 ton. Pre oceľ AISI 304 bolo celkovo pripravených šesť vzoriek – jedna referenčná vzorka po rozpúšťacom žíhaní a päť vzoriek s rôznymi stupňami plastickej deformácie (obr. 1).

Rozmery vzoriek po deformácii, ako aj vypočítané percentuálne zníženie výšky, sú uvedené v Tab. 2. S cieľom zabezpečiť spoľahlivú charakterizáciu mikroštruktúry boli všetky vzorky v jednotlivých stavoch podrobené štandardnej metalografickej príprave. Tá zahŕňala postupné brúsenie, leštenie a následné chemické leptanie. Na leptanie sa použilo leptadlo Kallings 2, ktoré pozostávalo zo zmesi 5 g $CuCl_2$, 100 ml HCl a 100 ml etanolu, pričom priemerný čas leptania bol približne 15 sekúnd.

Po metalografickej príprave bola mikroštruktúrna analýza vykonaná pomocou optického mikroskopu NEOPHOT 32. Fotodokumentácia sa vyhotovila pomocou programu NIS Elements 4 pri zväčšení 400×. Okrem toho bolo realizované meranie mikrotvrdosti podľa Vickersa na zariadení Zwick/Roell ZHμ pri zaťažení HV 0,5 s dobou pôsobenia 10 sekúnd pri izbovej teplote približne ± 20 °C. Schéma metalografického odberu a následného merania mikrotvrdosti je znázornená na obr. 2.

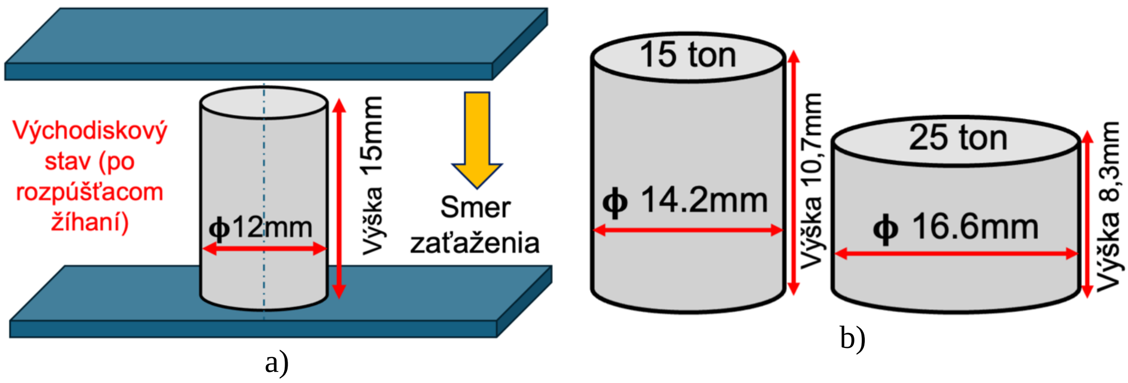

Obr. 1 *Tvar a rozmery vzoriek pred a po plastickej deformácii; a) referenčná vzorka po rozpúšťacom žíhaní a pred deformáciou, b) deformované vzorky*

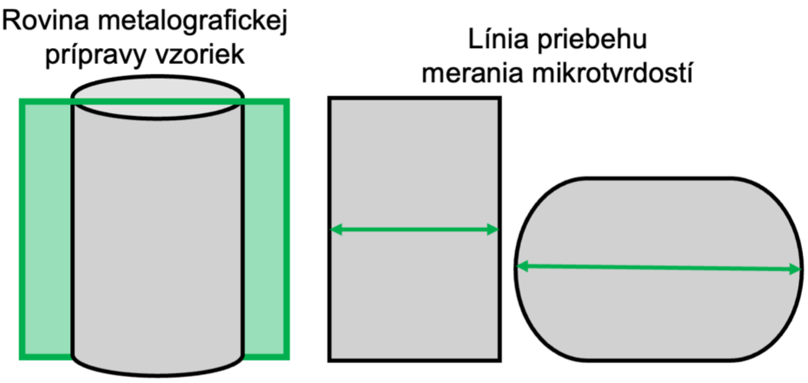

Obr. 2 *Schematické znázornenie miesta odberu vzoriek a poloha merania mikrotvrdosti*

Magnetické merania boli vykonané na Katedre fyziky VŠB – Technickej univerzity v Ostrave. Vzorky určené na meranie objemovej magnetizácie boli pripravené elektroerozívnym rezaním s cieľom zabezpečiť presnú geometriu a zároveň eliminovať tepelný vplyv na mikroštruktúru materiálu. Výsledné vzorky mali valcový tvar s priemerom 4 mm a hrúbkou 2 mm. Magnetizačné krivky boli zaznamenané pri izbovej teplote pomocou vibračného magnetometra (VSM, MicroSense EZ9) v externom magnetickom poli ±1600 kA/m.

Tab. 2 *Rozmery a úrovne deformácie vzoriek ocele AISI 304*

AISI 304			
Číslo vzorky	***Použité zaťaženie [t]***	***Výška vzroky po deformácii [mm]***	***Deformácia [%]***
1	*0 (RZ)*	*15,0*	*0*
2	*5*	*14,1*	*6,67*
3	*10*	*12,2*	*19,33*
4	*15*	*10,7*	*30*
5	*20*	*9,3*	*40*
6	*25*	*8.3*	*47,33*

3. Výsledky a diskusia

Po rozpúšťacom žíhaní pozostávala mikroštruktúra ocele AISI 304 z polyedrických austenitických zŕn s rôznou veľkosťou zŕn. V celej matrici bolo možné jasne identifikovať početné žíhacie dvojčatá (označené červenými šípkami). Neboli pozorované žiadne oblasti obsahujúce δ-ferit, čo potvrdzuje plne austenitický charakter mikroštruktúry po rozpúšťacom žíhaní. Okrem toho boli v mikroštruktúre detegované aj nekovové inklúzie s pretiahnutou morfológiou. Tento stav je preto považovaný za referenčný pre následné porovnania. Reprezentatívne mikroštruktúry sú znázornené na obrázku 3a. Pretiahnuté nekovové inklúzie pozorované v mikroštruktúre ocele AISI 304 boli podrobne analyzované pomocou rastrovacej elektrónovej mikroskopie metódou EDX a identifikované ako sulfide mangánatý (MnS) (obr. 3b). Inklúzie MnS sa typicky tvoria už počas odlievania a tuhnutia materiálu v dôsledku nízkej rozpustnosti síry v železnej matrici a vysokej afinity mangánu k síre.

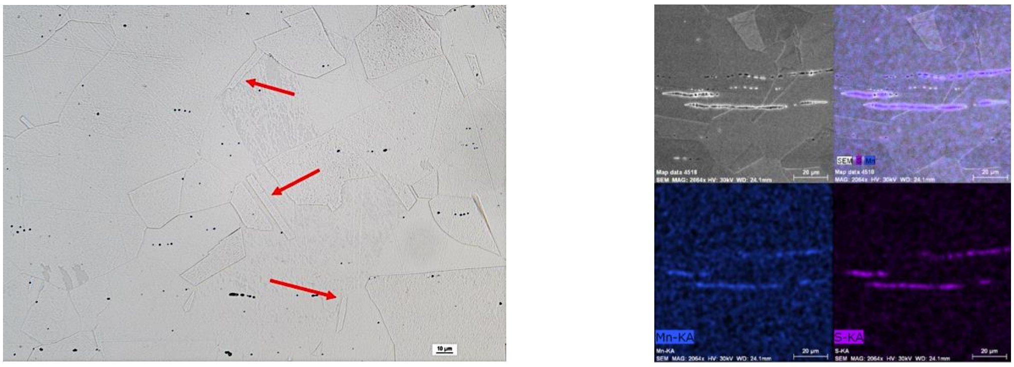

a) b)

***Obr. 3** Mikroštruktúra AISI 304 po rozpúšťacom žíhaní a identifikácia vtrúseniny; a) mikroštruktúra AISI 304 na optickom mikroskope, b) EDX analýza sulfidu mangánatého*

Po plastickej deformácii boli v mikroštruktúre ocele AISI 304 pozorované výrazné zmeny (obr. 4). Austenitické zrná vykazujú rastúcu mieru deformácie so zvyšujúcim sa stupňom zaťaženia, pričom pôvodne dobre vyvinuté žíhacie dvojčatá sa dajú tahšie rozlíšiť od pôvodnej čisto austenitickej štruktúry. Inklúzie MnS strácajú pôvodnú orientáciu a v deformovanej matrici sa vyskytujú náhodnejšie.

Pri vyšších stupňoch deformácie je zreteľný nástup deformačne indukovanej transformácie γ-austenit → α′-martenzit, pričom šmykové pásy a prekrývajúce sa siete dvojčatových a sklzových pásov predstavujú preferenčné miesta jej nukleácie, v súlade s pozorovaniami [9].

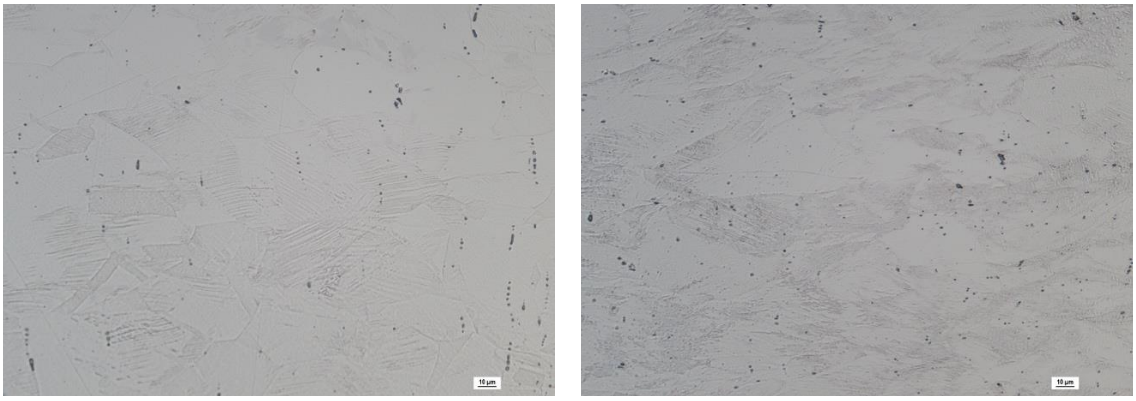

a) b)

***Obr. 4** Príklad mikroštruktúry ocele AISI 304 po plastickej deformácii; a) mikroštruktúra po 10t, b) mikroštruktúra po 25t, zväčšenie 400x, lept.*

Obrázok 5 sumarizuje výsledky merania mikrotvrdosti ocele AISI 304 po plastickej deformácii pri rôznych úrovniach tlakového zaťaženia. Najnižšie hodnoty mikrotvrdosti boli zaznamenané v stave po rozpúšťacom žíhaní, s rovnomerným rozložením približne 146 HV0,5. So zvyšujúcim sa stupňom deformácie dochádza k výraznému nárastu mikrotvrdosti, čo poukazuje na intenzívne deformačné spevnenie materiálu. Najvyššie hodnoty, dosahujúce až 409 HV0,5, boli namerané pri vzorke deformovanej zaťažením 25 ton. Rozloženie tvrdosti v priereze vzorky je nehomogénne, pričom vyššie hodnoty boli zaznamenané v centrálnej oblasti v porovnaní s okrajmi, čo potvrdzuje nerovnomernú distribúciu plastickej deformácie typickú pre tlakové skúšky. Pozorované spevnenie je výsledkom súbežného pôsobenia dvoch mechanizmov: akumulácie dislokácií v austenitickej matrici a tvorby deformačne indukovaného α′-martenzitu. Ako je uvedené [8, 9], rastúca hustota dislokácií zvyšuje napätie potrebné na pohyb dislokácií, zatiaľ čo čiastočná transformácia metastabilného austenitu (γ) na α′-martenzit poskytuje dodatočný spevňovací príspevok.

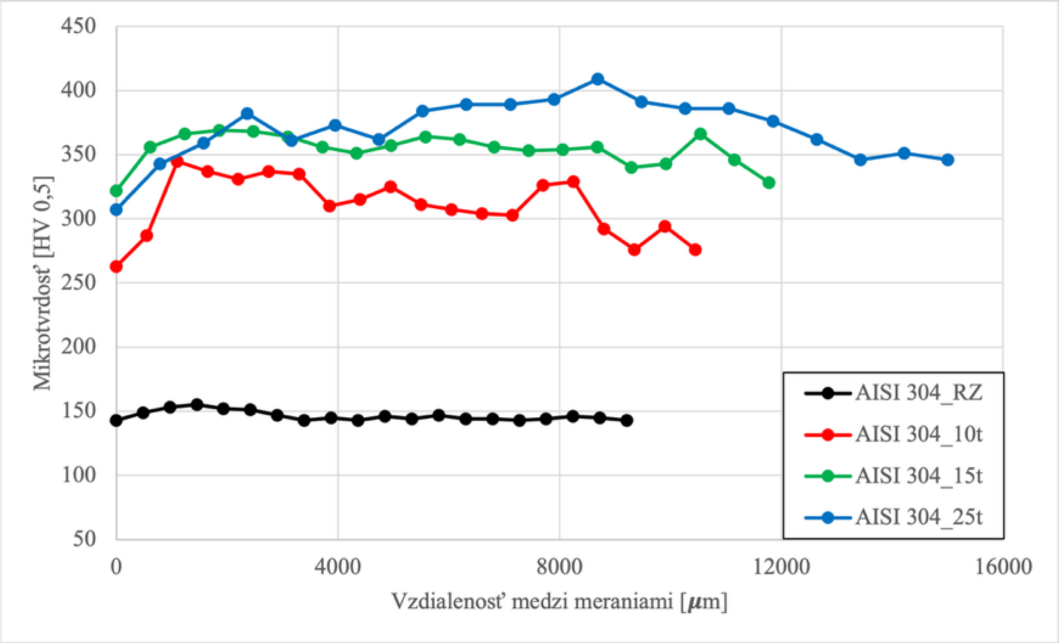

Obr. 5 *Priebeh mikrotvrdosti austenitickej ocele AISI 304*

Obrázok 6 zobrazuje hysterézne slučky ocele AISI 304 po rôznych stupňoch tlakovej plastickej deformácie. Počiatočné vzorky v stave po rozpúšťacom žíhaní vykazovali čisto paramagnetické správanie s zanedbateľnou magnetizáciou. So zvyšujúcim sa stupňom plastickej deformácie sa postupne objavovala výrazná feromagnetická odozva, čo potvrdzuje vznik deformačne indukovaného α′-martenzitu.

V prípade ocele AISI 304 bol nárast magnetizácie výrazný, pričom saturačná magnetizácia dosiahla približne 25 Am²/kg pri vzorke deformovanej zaťažením 25 ton. Koercitívne pole (H_c) sa znížilo z 13,97 na 4,97 kA/m, zatiaľ čo remanentná magnetizácia (M_r) vzrástla z 0,01 na 4,21 Am²/kg. Tento trend naznačuje postupnú tvorbu α′-martenzitu so zvyšujúcou sa deformáciou a stabilizáciu feromagnetických domén. Súčasný pokles koercitivity poukazuje na ľahší pohyb doménových stien v silne deformovanej mikroštruktúre.

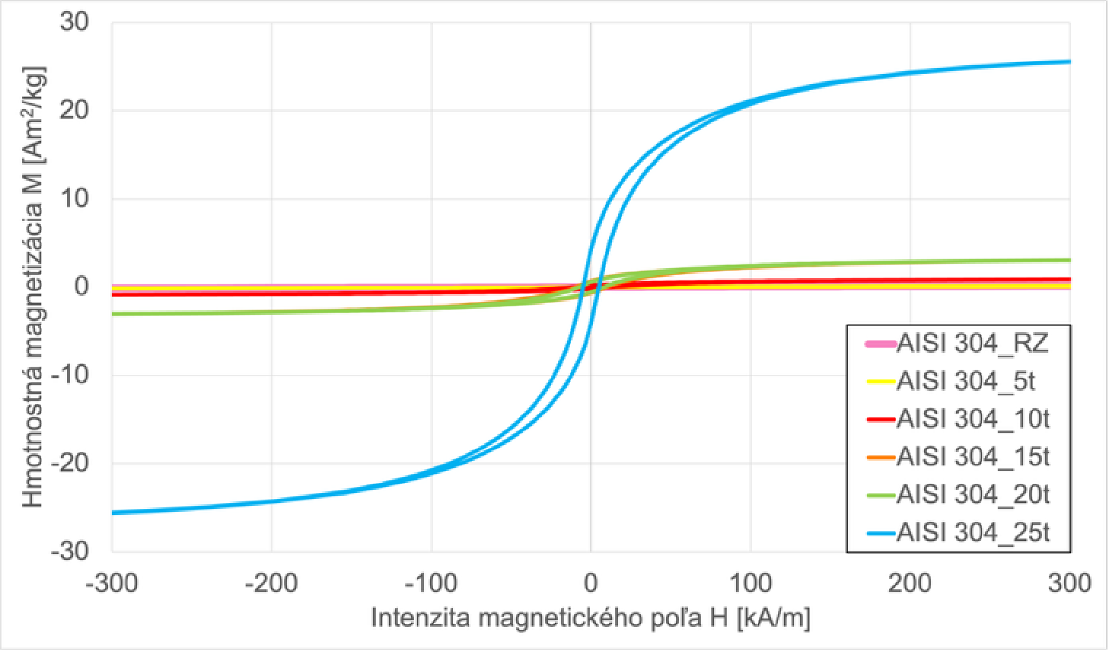

Obr. 6 *Hysterézne slučky ocele AISI 304*

4. Záver

Táto práca experimentálne hodnotila vplyv tlakovej plastickej deformácie na štruktúrne, mechanické a magnetické vlastnosti austenitickej nehrdzavejúcej ocele AISI 304.

- Mikroštruktúrna analýza preukázala, že plastická deformácia vedie k výraznej deformácii austenitických zŕn, k vzniku deformačne indukovaného α′-martenzitu, najmä v oblastiach šmykových pásov a prekrývajúcich sa sklzových systémov.
- Merania mikrotvrdosti potvrdili výrazné deformačné spevnenie materiálu so zvyšujúcim sa stupňom deformácie, pričom nárast tvrdosti bol spôsobený kombináciou akumulácie dislokácií v austenitickej matrici a tvorbou α′-martenzitu. Nerovnomerné rozloženie tvrdosti v priereze vzoriek odráža nehomogénnu distribúciu plastickej deformácie typickú pre tlakové zaťaženie.
- Magnetická merania ukázali prechod z pôvodného paramagnetického správania do výraznej feromagnetickej odozvy v dôsledku tvorby deformačne indukovaného α′-martenzitu. Intenzita magnetizácie rástla so stupňom deformácie, čo potvrdzuje úzku koreláciu medzi mikroštruktúrnymi zmenami, mechanickým spevnením a magnetickými vlastnosťami ocele AISI 304.

Acknowledgment

Tento výskum bol podporený Vedeckou grantovou agentúrou Ministerstva školstva, výskumu, vývoja a mládeže Slovenskej republiky VEGA, č. 1/0831/25 and VEGA 1/0729/26.

References

[1] Jia, S., Tan, Q., Ye, J., Zhu, Z., Jiang, Z.: Experiments on dynamic mechanical properties of austenitic stainless steel S30408 and S31608. Journal of Constructional Steel Research, Vol. 179, 2021.

[2] Shen, Y. F., Li, X. X., Sun, X., Wang, Y. D., Zuo, L.: Twinning and martensite in a 304 austenitic stainless steel. Materials Science and Engineering: A, Vol 552, pp 514-522. 2012.

[3] Nkhoma, R. K., Siyasiya, C. W., & Stumpf, W. E.: Hot workability of AISI 321 and AISI 304 austenitic stainless steels. Journal of Alloys and Compounds, Vol 595, pp 103-112. 2014.

[4] Xie, S., Wu, L., Tong, Z., Chen, H. E., Chen, Z., Uchimoto, T., Takagi, T.: Influence of plastic deformation and fatigue damage on electromagnetic properties of 304 austenitic stainless steel. IEEE Transactions on Magnetics, Vol 54(8), pp 1-10. .2018.

[5] Takahashi, S., Echigoya, J., Ueda, T., Li, X., Hatafuku, H.: Martensitic transformation due to plastic deformation and magnetic properties in SUS 304 stainless steel. Journal of Materials Processing Technology, Vol 108(2), pp 213-216. 2001.

[6] Liu, Y., Hu, B., Lan, X., Fu, P.: Micromagnetic characteristic changes and mechanism induced by plastic deformation of 304 austenitic stainless steel. Materials Today Communications, Vol 27, . 2021.

[7] Lan, X., Hu, B., Wang, S., Luo, W., Fu, P.: Magnetic characteristics and mechanism of 304 austenitic stainless steel under fatigue loading. Engineering Failure Analysis, Vol 136. 2022.

[8] Sohrabi, M. J., Naghizadeh, M., Mirzadeh, H.: Deformation-induced martensite in austenitic stainless steels: A review. Archives of Civil and Mechanical Engineering, Vol 20 (4). 2020.

[9] Talonen, J., & Hänninen, H.: Formation of shear bands and strain-induced martensite during plastic deformation of metastable austenitic stainless steels. Acta materialia. Vol 55(18), pp 6108-6118. 2007.

29th International Seminar of Ph.D. Students
SEMDOK 2026
Western Tatras – Zuberec, Slovak Republic
February, 4 to February 6, 2026

INFLUENCE OF IN_2 O_3 NANOPARTICLE INCORPORATION ON THE MORPHOLOGY AND OPTICAL PROPERTIES OF PVP NANOFIBERS

Weronika Smok[1*], **Antonina Olszewska**[1], **Wiktoria Wanczura**[1], **Marcin Staszuk**[1], **Jarosław Mikuła**[1]

[1] Department of Engineering Materials and Biomaterials, Silesian University of Technology, Gliwice, Poland

**Corresponding author: weronika.smok@polsl.pl, e-mail, +48 32 237 16 53, Konarskiego 18A, 44-100 Gliwice, Poland*

1. Introduction

Nanofibrous mats produced by solution electrospinning have attracted considerable interest in the scientific community due to the simplicity of their fabrication, the possibility of tailoring their properties, their high application potential, and the wide range of materials that can be employed [1–3].

One of the most commonly and successfully used polymers in electrospinning is polyvinylpyrrolidone (PVP). This is primarily attributed to its good solubility in various solvents, low toxicity, and ease of fiber formation over a broad range of electrospinning parameters [3]. Consequently, PVP constitutes an excellent matrix for the fabrication of composite nanofibers incorporating metal oxide nanoparticles such as TiO_2, ZnO, SnO_2, or In_2O_3. Particular attention should be paid to the latter, as indium oxide exhibits outstanding chemical and thermal stability. It is a typical wide-bandgap *n*-type semiconductor (3.5-4.0 eV), characterized by high transparency in the visible range, a high electron concentration, and good electrical conductivity [4].

These properties make In_2O_3 widely applicable in technologies requiring advanced optical and electrical performance, including screens and displays, gas sensors, transistors, LEDs, and photovoltaic cells [4–7]. Therefore, the incorporation of semiconducting metal oxide nanoparticles into PVP nanofibers can beneficially influence both their morphology and physicochemical properties, enhancing their functionality and expanding their potential application scope.

Hence, the aim of this work was to prepare PVP-based polymer nanofibrous mats and composite mats with the addition of In_2O_3 nanoparticles by electrospinning from a solution and to analyze the effect of nanoparticles addition on the morphology and optical properties of PVP nanofibers.

2. Materials and methods

In the first stage, four solutions with a constant PVP concentration (10 wt.%) in ethanol and varying In_2O_3 concentrations (0 wt.%, 2 wt.%, 5 wt.%, and 12.5 wt.% relative to the polymer mass) were prepared.

Immediately after two hours of homogenization, the homogeneous solutions were successively transferred to the syringe pump of a FLOW Nanotechnology Solutions Electrospinner 2.2.0-500, using the parameters listed in Table 1.

The morphology of the In_2O_3 nanoparticles used as an additive to PVP, as well as the electrospun PVP and PVP/In_2O_3 nanofibers, was characterized using a Zeiss Supra 35 scanning electron microscope (SEM). The analysis included evaluation of the effect of nanoparticles on the nanofiber morphology and measurement of the diameters of the obtained nanostructures.

The final stage of the study involved analysis of electromagnetic radiation absorption in the UV-Vis range using a Thermo Scientific Evolution 220 UV-Vis spectrophotometer, followed by determination of the optical band gap based on the recorded spectra.

Tab. 1 *Parametres of electrospinning process*

Parameter	*Distance [cm]*	*Voltage [kV]*	*Flow rate [ml/h]*
PVP	*15*	*21*	*3*
PVP/In_2O_3 2 %			*3*
PVP/In_2O_3 5 %			*5*
PVP/In_2O_3 12.5 %			*6*

2. Results and discussion

The morphology of In_2O_3 nanoparticles was analyzed based on SEM images shown in Fig. 1. The images revealed that the nanoparticles exhibit irregular shapes and a tendency to form micrometer-sized agglomerates, which is a typical phenomenon for nanomaterials with high surface energy [8].

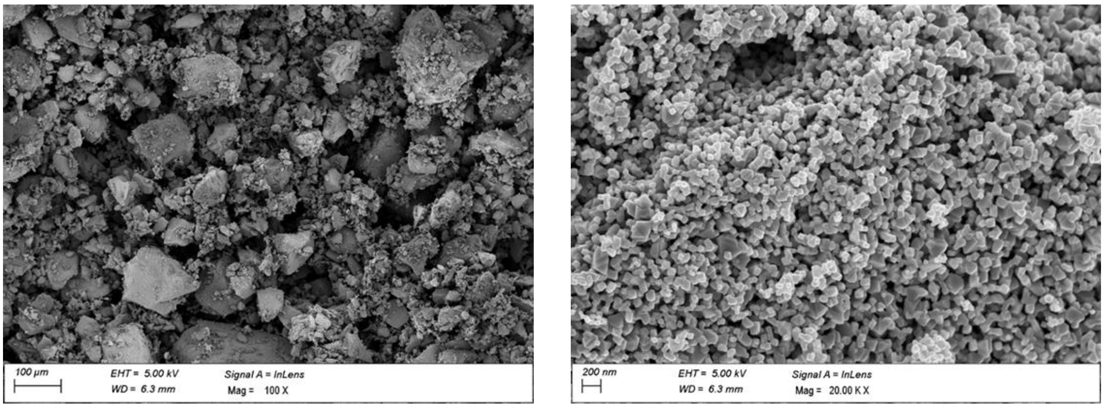

a) 100X *b) 20 000X*

Fig. 1 *SEM images of In_2O_3 nanoparticles with different magnification*

Figure 2 presents SEM images of PVP nanofibers and PVP nanofibers containing different concentrations of In_2O_3 nanoparticles. Observation of the morphology of PVP and PVP/In_2O_3 2% nanofibers indicated that the obtained nanofibers were homogeneous;

however, the presence of fused nanofibers was observed. This may indicate excessively slow solvent evaporation during electrospinning, which consequently leads to the deposition of wet fibers on the collector with a high tendency to adhere to each other [9]. As expected, SEM image analysis of PVP/In_2O_3 nanofibers confirmed the presence of uniformly dispersed agglomerates of In_2O_3 nanoparticles within the PVP nanofibers (marked with circles).

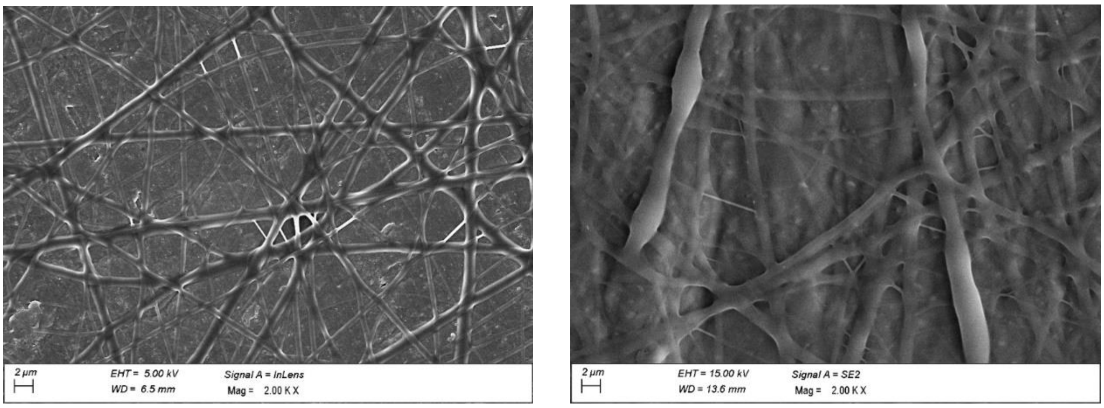

a) InLens *b) SE*

Fig. 2 *SEM images of pure PVP nanofibers in different mode*

Furthermore, it was observed that with increasing nanoparticle concentration in the PVP matrix, the nanofiber diameter increases, however, the sample with the highest nanoparticle concentration presented the smallest diameter and the best dispersion of nanoparticles in the nanofiber volume (Tab. 2). This effect can be attributed to changes in the electrical conductivity of the spinning solution and improved stretching of the nanofibers during the electrospinning process [9].

UV–Vis spectroscopy was performed to analyze the optical properties of pure PVP nanofibers and PVP/In_2O_3 composite nanofibers with three different In_2O_3 concentrations. Figure 4a shows the absorption spectra in the wavelength range of 250–800 nm for all investigated samples. It was observed that the absorption maximum of all samples lies in the middle ultraviolet region and shifts slightly toward the visible range with increasing concentration of inorganic nanoparticles.

Subsequently, the energy band gap (Eg) of the fabricated nanostructures was determined based on Tauc plots [10]. The Eg value determined for the thin PVP nanofibrous layer was similar to that presented so far in the literature (Tab. 2) [11]. The similar value of Eg of all samples indicates that indium oxide nanoparticles do not significantly affect the band structure of the material, and that the observed changes in the band gap width are purely optical in nature (Tab. 2). This suggests that In_2O_3 didn't introduce new energy levels into the PVP structure; instead, it acts as a local morphology modifier or as a light-scattering center. Nevertheless, doping with indium oxide may influence the ordering of polymer chains.

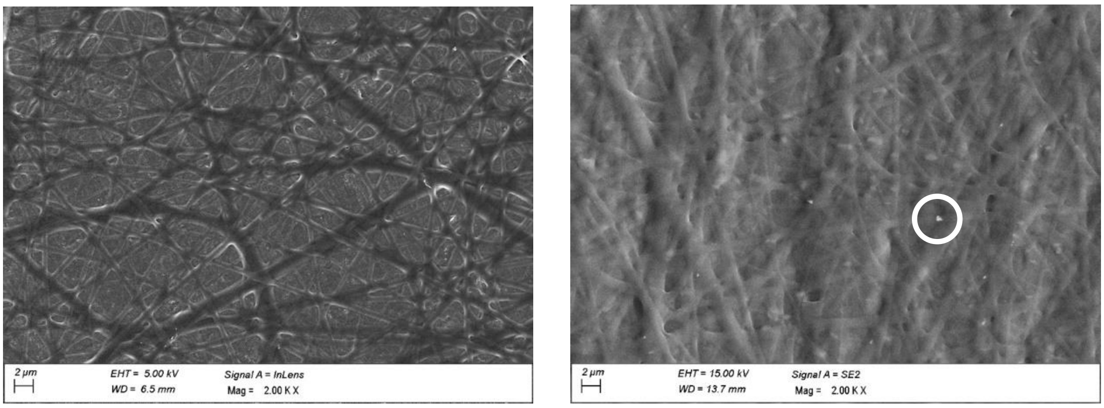

a) 2 %, InLens mode *b) 2 %, SE mode*

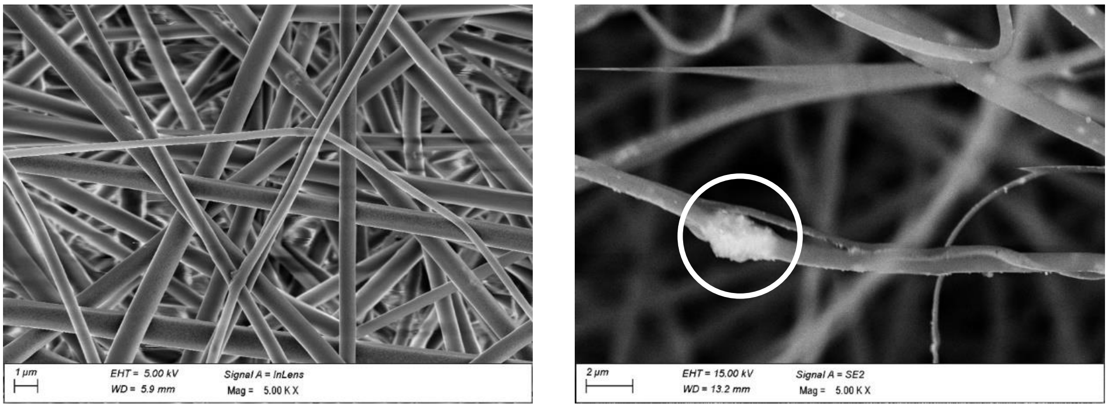

c) 5%, InLens mode *d) 5 %, SE mode*

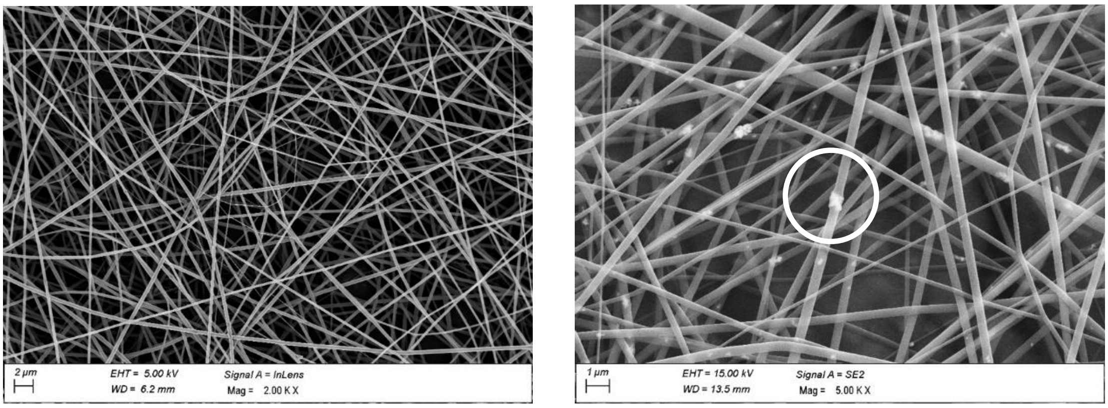

e) 12.5 %, InLens mode *f) 12.5 %, SE mode*

Fig. 3 *SEM images of PVP/In_2O_3 nanofibers with different nanoparticles concentration*

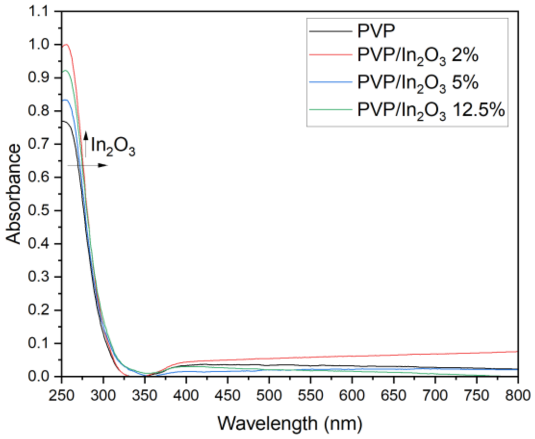

***Fig. 4** UV-Vis spectra of PVP and PVP/In_2O_3 nanofibers*

***Tab. 2** Mean diameter and optical band gap of the obtained PVP and PVP/In_2O_3 nanofibers*

Parameter	***Diameter [nm]***	***Band gap [eV]***
PVP	*489*	*4.30*
PVP/In_2O_3 2 %	*638*	*4.30*
PVP/In_2O_3 5 %	*697*	*4.28*
PVP/In_2O_3 12.5 %	*256*	*4.29*

3. Conclusions

The work demonstrated that electrospinning enables the fabrication of uniform PVP and PVP/In_2O_3 nanofibers with controlled morphology. SEM analysis confirmed that In_2O_3 nanoparticles exhibit a tendency to agglomerate; however, their agglomerates were uniformly distributed within the PVP nanofibers. An increase in In_2O_3 content resulted in a reduction of nanofiber diameter, which was attributed to enhanced electrical conductivity of the spinning solution and improved fiber stretching during electrospinning. UV-Vis spectroscopy revealed that all samples exhibit absorption maxima in the middle ultraviolet region, with a slight red shift observed at higher nanoparticle concentrations. The optical band gap remained nearly constant, indicating that In_2O_3 nanoparticles do not alter the electronic band structure of PVP. Instead, indium oxide acts primarily as a morphological modifier and light-scattering center, while potentially influencing the ordering of polymer chains.

References

[1]Nobakht, A., Natouri, O., Barzegar, A.: PCL/Collagen Micro/Nanofiber–Nanonets Loaded with Malva Extract for Infected Wound Healing. Journal of Drug Delivery Science and Technology, Vol. 116, No. 107854, 2026.

[2]Cheriyan, S., Karthega, M.: In Vitro Studies on Bioactive Senna Auriculata Flower Extract Incorporated PCL - Cellulose Acetate Electrospun Nanofiber for Wound Dressing Application. Journal of Drug Delivery Science and Technology, Vol. 113, No. 107357, 2025.

[3]Li, Z., Zhou, J., Xu, Y., Chen, C., Ran, T., Wang, S.: Preparation of PVDF/PVP Blend Polymer Nanofiber Films and Application on Screen-Printed Flexible Electrodes. European Polymer Journal, Vol. 206, No. 112740, 2024.

[4]Smok, W., Zaborowska, M., Tański, T., Radoń, A.: Novel In2O3/SnO2 Heterojunction 1D Nanostructure Photocatalyst for MB Degradation. Optical Materials, Vol. 139, No. 113757, 2023.

[5]Feng, C., Li, X., Ma, J., Sun, Y., Wang, C., Sun, P., Zheng, J., Lu, G.: Facile Synthesis and Gas Sensing Properties of In2O3-WO3 Heterojunction Nanofibers. Sensors and Actuators B: Chemical, Vol. 209, pp. 622–629, 2015.

[6]Alves, M., Brito, D., Carneiro, J., Teixeira, V., Sadewasser, S.: Radio-Frequency Magnetron Sputtering Deposition Process for In2O3:H Transparent Conductive Oxide Films for Application in Cu(In,Ga)Se2 Solar Cells. Thin Solid Films, Vol. 774, No. 139840, 2023.

[7]Xie, R., Fang, K., Liu, Y., Chen, W., Fan, J., Wang, X., Ren, Y., Song, Y.: Z-Scheme In2O3/WO3 Heterogeneous Photocatalysts with Enhanced Visible-Light-Driven Photocatalytic Activity toward Degradation of Organic Dyes. Journal of Materials Science, Vol. 55, pp. 11919–11937, 2020.

[8]Vollath, D.: Agglomerates of Nanoparticles. Beilstein Journal of Nanotechnology, Vol. 11, pp. 854–857, 2020.

[9]Cho, Y., Beak, J.W., Sagong, M., Ahn, S., Nam, J.S., Kim, I.D.: Electrospinning and Nanofiber Technology: Fundamentals, Innovations, and Applications. Advanced Materials,Vol. 37, No. 2500162, 2025.

[10] Zaborowska, M., Smok, W., Tański, T.: Electrospinning Synthesis and Characterization of Zirconia Nanofibers Annealed at Different Temperatures. Applied Surface Science, Vol. 615, No. 156342, 2023.

[11] Mahmoud, K.H., Alsubaie, A.S., Elsayed, K.A.: Modulation of Optical Properties of PolyvinylPyrrolidone via Doping with Praseodymium (III) Nitrate Salt. Optik, Vol. 231, No. 166383, 2021.

29th International Seminar of Ph.D. Students

SEMDOK 2026

Western Tatras – Zuberec, Slovak Republic
February, 4 to February 6, 2026

OPTIMIZATION OF THE GMA WELDING PROCESS OF A CAR HEADLIGHT HOLDER ELEMENT

Marek SROKA*[1], Ewa JONDA[1], Michał ŚLIWIŃSKI[1]
[1]Silesian University of Technology, Department of Engineering Materials and Biomaterials, S. Konarskiego 18A, 44-100 Gliwice, Poland
**Corresponding author: marek.sroka@polsl.pl , tel: +48 32-237-18-47, Silesian University of Technology, Department of Engineering Materials and Biomaterials, S. Konarskiego 18A, 44-100 Gliwice, Poland*

1. Introduction

The contact tips are the smallest as well as the most important consumable parts in the welding torch (Fig. 1), no matter if it is manual, automatic or robotic one. They are one of the most frequently replaced parts because, due to their function in the welding process, they are exposed to the greatest energy. The purpose of the contact tips is to transfer current to the electrode wire and ensure a stable and well-directed electric arc. In order to strike the arc, the wire must pass through the contact tip, which can cause abrasion of the walls because the large amounts of welding wire pass through the contact tip during the process [1-3].

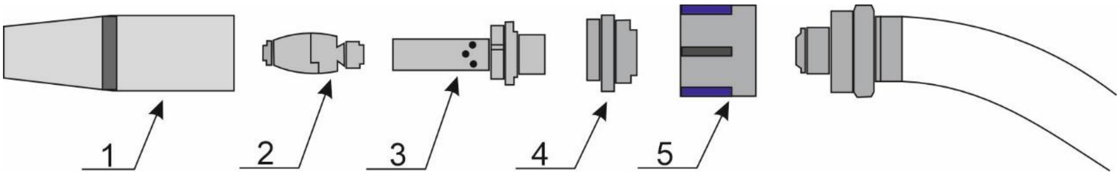

Fig. 1 Scheme of the welding torch: 1 - gas nozzle, 2 – contact tip, 3 – current connector, 4 – mounting the contact tip, 5 – anti-splinter cover [4]

Depending on the material, design and torch neck, the intensive abrasive wear may occur during wire feeding. It results in that metal particles are transferred to the contact tip and it could cause clogging of the contact tip outlet. In case of the straight-neck welding torches which are often used in robotic stations, the problems with contact tips are related to the small contact area as well as short contact time. This leads to the formation of micro arcs in the contact tip which causes more intensive material wear. Depending on the process, wire quality and contact tip material, the functional properties are getting worse and worse. It has to be quickly replaced before the welding process becomes unstable and the tip will be destroyed. The wear degree of the contact tips significantly affects the quality of the process, the service life and the work efficiency as well as the welded joints quality [5-7].
The fastest and most commonly used method to determine the weld joints quality is their visual assessment and macroscopic examinations. It allows to detect materials imperfections e.g. cracks, undercuts. On the other hand, the analysis of the structure and chemical composition allows checking and assessing other parameters of the tested material, such as sulfur or phosphorus contamination, grain size, hardening depth, structure directionality and crack characteristics. Moreover, in order to check the efficiency of the

use of equipment, the overall equipment effectiveness (OEE) indicator is calculated. This factor shows the degree of utilization of machines and equipment in the percentage way [8,9].

The aim of the investigations and analyzes carried out in the current article was to optimize the welding process of a car headlight holder element, using the gas metal arc welding (GMAW) method with two types of current tips: (i) M6x24x1.2 - Cu (Fronius) and (ii) M6x24x1.2 - CuCrZr (B2B). This was achieved by determining the service life of the used contact tips, the weld joints quality and reducing the number of downtimes as well as minimizing production defects that appeared during the process [10-12].

2. Materials and methods

The objective of the investigations and analysis were weld joints of the car headlight holder element manufactured by GMAW method. Tested joint were made by two types of the contact tips: (i) M6x24x1.2 - Cu (Fronius) and (ii) M6x24x1.2 - CuCrZr (B2B). Within one month, Fronius tips were used to manufacture weld joints were replaced with B2B ones.

In the production of Cu tips, pure electrolytic copper (E-Cu) is used, with a hardness of c.a. 115 HV and a softening temperature of c.a. 260°C. The purity of copper ensures very good electrical and thermal conductivity, but unfortunately it is characterized by a low service life. In the case of CuCrZr tips, the addition of chromium and zirconium, which are characterized by high hardness, ensures high thermal resistance. However, the electrical and thermal transfer is lower than in the case of tips made of pure copper (E-Cu). The hardness of CuCrZr tips is c.a. 170 HV and the softening temperature is c.a. 500°C which increases their resistance to thermal loads and low wear with a correspondingly high process load.

Visual examination of the weld joints consisted of examining its before and after replacing the contact tips and checking whether their quality had improved after the change. The assessment was performed in accordance with the PN-EN ISO 5817 standard.

The structure of the weld joints was assessed based on macroscopic examinations performed with a phase contrast microscope Zeiss Axilo Lab A1 (Zeiss Microscopy GmbH, Germany). The test samples were cut and ground with 320µm SiC sandpapers and then etched at room temperature with Alder I reagent. After etching, the samples were rinsed with water and then with ethyl alcohol. Finally, it was dried with a stream of warm air.

In order to check the efficiency of the machine before and after changing the contact tips, the OEE index was calculated, determining the percentage of machine utilization and parameters such as availability, efficiency and quality (eq. 1).

$$OEE = A \cdot E \cdot Q \cdot 100\% \tag{1}$$

Availability (A) is an indicator informing about the ratio of time planned for the implementation of production tasks to the actual time dedicated to production. In this case, availability is calculated based on the contact tip replacement time (eq. 2).

$$A = \frac{t_1 - t_2}{t_1} \tag{2}$$

where:
t_1 – change time, min

t_2 – downtime, min

Efficiency (E) is an indicator of the ratio of time to actual work. It is calculated by dividing the number of parts produced by capacity (eq. 3).

$$E = \frac{p_c}{p_t} \tag{3}$$

where:
p_c – production completed, pieces
p_t – production target, pieces

Quality (Q) is calculated as the ratio of good products to the total number of contact tips produced per month (eq. 4).

$$Q = \frac{P-L}{P} \tag{4}$$

where:
P – production, pieces
L – lack, pieces

3. Results

Analysis of the process efficiency before and after changing contact tips

Figures 2 and 3 show the machine operating time before and after changing the contact tips in relation to other errors occurring in the process. As it could be seen, before changing the contact tips, the machine's operating time was equal to 67 % and the time for changing the tips was equal to 741 minutes. After replacing the Cu tips with a substitute (CuCrZr), the machine operation time increased to 74%, while the replacement time of the tips was reduced to 421.2 minutes. Based on the observation data, it was also found that after changing the contact tips, the average number of replaced contact tips per working day decreased from 15.9 to 7.1 pieces. In the first month, 334 Cu tips were used, while in the second month only 156 CuCrZr tips were used.

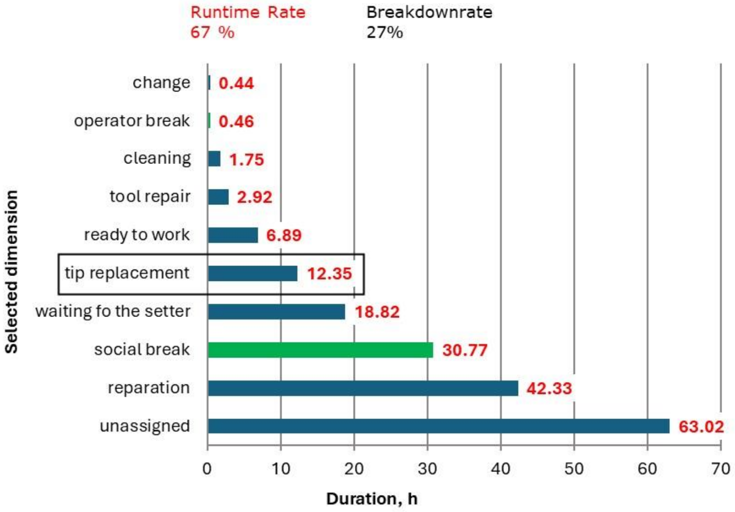

Fig. 2 *Machine operating time before changing contact tips*

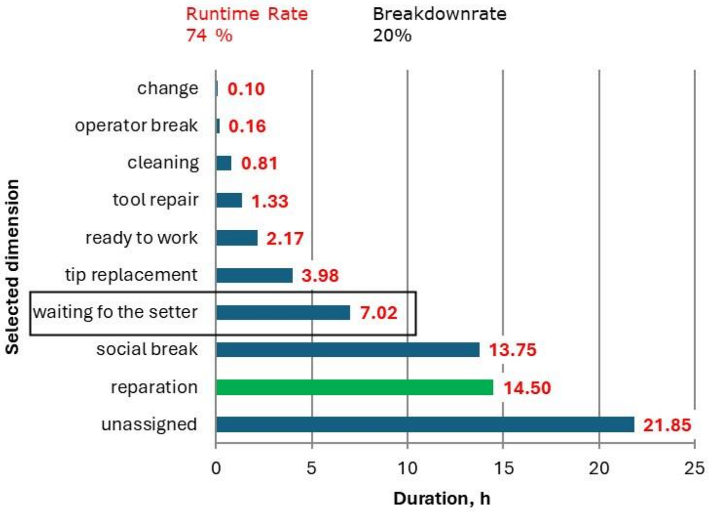

Fig. 3 *Machine operating time after changing contact tips*

Visual testing of the weld joints

The most common defects occurring in welds made using Cu tips are craters, sticking of the weld, incomplete fusion and metal spatter on free surfaces (Figs. 4a and 4b). After changing the tips to CuCrZr ones, an improvement in the quality of welded joints was visible. The number of craters and weld spatters significantly decreased (Figs. 4c and 4d).

Fig. 4 *View of the welds before replacing the contact tip (a and b) with visible craters and after replacing the contact tips (c and d) with a correctly manufactured joints.*

Macroscope examinations

Based on analyzes performed using a phase contrast microscope type, size and distribution of internal imperfections occurring in the tested weld joints were obtained. After changing the contact tips, the number of craters and welding imperfections per month decreased and the welds became symmetrical and more repeatable in shape. As a result of the analysis of the obtained test results, it can be concluded that the chemical composition of the contact tip influences the quality of the welding process (Figs. 5a-5d).

Fig.5 *View of welds made before changing the contact tips with visible voids (a and b) and view of welds made correctly after replacing the contact tips (c and d), mag. 17x*

OEE indicator

Based on the obtained results of the OEE indicator calculations in relation to the machine's operation, a significant difference can be noticed in the time of replacing contact tips between the month in which Cu tips were used and the operating time using CuCrZr tips. Before the tip change, the OEE factor was equal to 87.5 % and after the change it increased to 93.1 %. The indicator after changing Cu to CuCrZr tips increased by 5.6%. Figure 6 shows a comparison of the OEE indicator values before and after changing the contact tips.

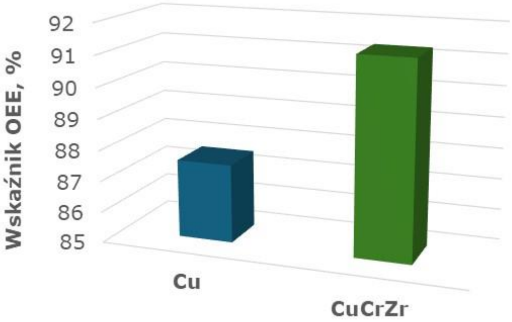

Fig.6 *Comparison of the OEE indicator before and after changing contact tips*

Based on the analyzes performed, it is possible to notice the influence of the chemical composition on the number of replacements, because tips made of electrolytic copper have worse results in terms of service life than tips containing CuCrZr. Over 21 working days, Cu tips were replaced 334 times, while CuCrZr tips were replaced 156 times over a 22-day period. Averaging the results before changing the contact tips, their replacement was necessary on average 16 times a day, while after the modification it was necessary 7 times during the working day. After the replacement, the demand for tip substitution decreased by 43.75%.

4. Conclusions

The investigations of the contact tips were carried out over a period of two months, in the first one the welding machine worked with Fronius M6x24x1.2 Cu contact tips for 21 working days, while in the second one the tips were changed to B2B M6x24x1.2 CuCrZr and they were used for 22 working days. Then, visual and macroscopic testing as well as analyzes of the weld joints quality were carried out. The OEE indicator was calculated for the GMAW process before and after changing the contact tips. Based on the results obtained, it was clearly stated that the process had improved. Process optimization involving the use of replacement contact tips had a positive impact on the stability of the process: the machine's operating time increased, the number of machine stops decreased, the cycle became more repeatable, and the quality of the weld joints improved.

References

[1] Ferenc, K.:Spawalnictwo, Wydawnictwo Naukowo-Techniczne. Warszawa, 2007.
[2] Pilarczyk, J.: Poradnik inżyniera. Tom 1. Spawalnictwo. Wydawnictwo Wydawnictwo Naukowo-Techniczne. Warszawa, 2017.
[3] Pilarczyk, J.: Poradnik inżyniera. Tom 2. Spawalnictwo. Wydawnictwo Wydawnictwo Naukowo-Techniczne. Warszawa, 2017.
[4] https://blog.perfectwelding.fronius.com/pl/palniki-mig-mag-jakie-moga-byc/, available on-line 5.01.2026.
[5] Czuchryj, J., Sikora, S.: Niezgodności spawalnicze w złączach spawanych z metali i termoplastycznych tworzyw sztucznych. Instytut spawalnictwa. Gliwice, 2016.
[6] Mizierski, J.: Spawanie w osłonie gazów metodami MAG i MIG. Podręcznik dla spawaczy i personelu nadzoru spawalniczego. Wydawnictwo REA, 2005.
[7] Kou, S.: Welding Metallurgy. Second Edition. University of Wisconsin, 2003.
[8] Tasak, E.: Metalurgia Spawania wydanie 1, Wydawnictwo JAK. Kraków, 2008.
[9] Mazur, M.: Podstawy spawalnictwa. Gliwice, 1993.
[10] Ambroziak, A.: Techniki wytwarzania spawalnictwo. Oficyna Wydawnicza Politechniki Wrocławskiej. Wrocław, 2010.
[11] Houldcroft, P.T.: Submerged-arcwelding. Woodhead Publishing Limited. Abington, 1989.
[12] Wyszyński, D.: Spawanie laserowe – wybrane metody. Przegląd spawalnictwa, Vol. 88, pp. 28-32, 2016.

29th International Seminar of Ph.D. Students
SEMDOK 2026
Western Tatras – Zuberec, Slovak Republic
February, 4 to February 6, 2026

SEKUNDÁRNE HLINÍKOVÉ ZLIATINY A356 V AUTOMOBILOVOM PRIEMYSLE: PREHĽAD

Zuzana Straková[1*], Lenka Kuchariková[1], Eva Tillová[1]
[1]*Strojnícka fakulta, Katedra materiálového inžinierstva, Žilinská univerzita v Žiline, Univerzitná 8215/1, 010 26 Žilina, Slovenská republika*
**zuzana.strakova@fstroj.uniza.sk, +421 41 513 2612, Strojnícka fakulta, Katedra materiálového inžinierstva, Žilinská univerzita v Žiline, Univerzitná 8215/1, 010 26 Žilina, Slovenská republika.*

1. Potreba odľahčovania konštrukcií

Automobilový priemysel prechádza výraznou transformáciou, ktorá je poháňaná elektrifikáciou, požiadavkami na efektívne využívanie zdrojov a prechodom ku cirkulárnej ekonomike. Hliníkové zliatiny zohrávajú v tomto procese kľúčovú úlohu, a to vďaka svojej dobrej zlievateľnosti, koróznej odolnosti a vysokej miere recyklovateľnosti. Tieto vlastnosti robia z hliníka jeden z najvýznamnejších materiálov pre ľahké konštrukcie v automobiloch so spaľovacím motorom aj v elektrických vozidlách [1-7].

Hoci sa s rozvojom pozornosť presúva za hranice emisií výfukových plynov, znižovanie hmotnosti vozidla zostáva zásadným konštrukčným princípom. Nižšia hmotnosť hliníka vedie k nižšej spotrebe energie, vyššiemu dojazdu a efektívnejšiemu dimenzovaniu batérií. Sprísňovanie emisných limitov CO_2, napríklad cieľ EÚ 96,6 g CO_2/km, urýchlilo zavádzanie ľahkých materiálov do sériovej výroby [8-10].

V elektrických vozidlách má hliník osobitý význam aj z hľadiska životného cyklu, keďže hmotnosť vozidla ovplyvňuje spotrebu surovín, veľkosť batérie a environmentálnu stopu počas prevádzky. Tieto faktory viedli k zvýšenému využívaniu hliníkových odliatkov najmä v krytoch batérií, elektromotorov a nosných konštrukčných prvkoch [6,12-15].

Z hľadiska udržateľnosti je hliník výnimočný jeho schopnosťou byť opakovane recyklovaný bez straty základných vlastností. Výroba sekundárneho hliníka spotrebuje len približne 5 % energie potrebnej na primárnu výrobu, čo výrazne znižuje náklady a emisie skleníkových plynov. Zliatina A356 (AlSi7Mg0,3) patrí medzi najpoužívanejšie hliníkové zliatiny na odliatky v automobilovom priemysle. Vyznačuje sa výbornou zlievateľnosťou, priaznivým pomerom pevnosti k hmotnosti a možnosťou tepelného spracovania [16-19].

Napriek rozsiahlemu výskumu recyklácie hliníka a železitých intermetalických fáz stále chýba ucelený prehľad, ktorý by prepájal metalurgiu sekundárnej zliatiny A356 s požiadavkami elektrických vozidiel. Preto je cieľom tejto prehľadovej práce poskytnúť kritický prehľad recyklácie hliníkových zliatin pre automobilové aplikácie so zameraním na sekundárne zliatiny A356, vplyv recykláciou indukovaných nežiadúcich sprievodných prvkov na mikroštruktúru a vlastnosti a účinnosť mitigačných stratégií, ako je legovanie mangánom.

2. Recyklácia hliníka a cirkulárna ekonomika

Recyklácia hliníka (Obr. 1) predstavuje vysoko efektívny materiálový cyklus priemyslu a je kľúčovou súčasťou cirkulárnej ekonomiky v kovospracujúcom sektore. Na rozdiel od keramických alebo polymérnych materiálov si hliník počas opätovného tavenia zachováva svoju kovovú štruktúru, čo umožňuje jeho recykláciu na nové produkty bez straty kľúčových vlastností. Táto jeho schopnosť robí z hliníka a jeho zliatin ideálny materiál pre dlhodobé udržateľné využitie v automobilovej výrobe [16–18].

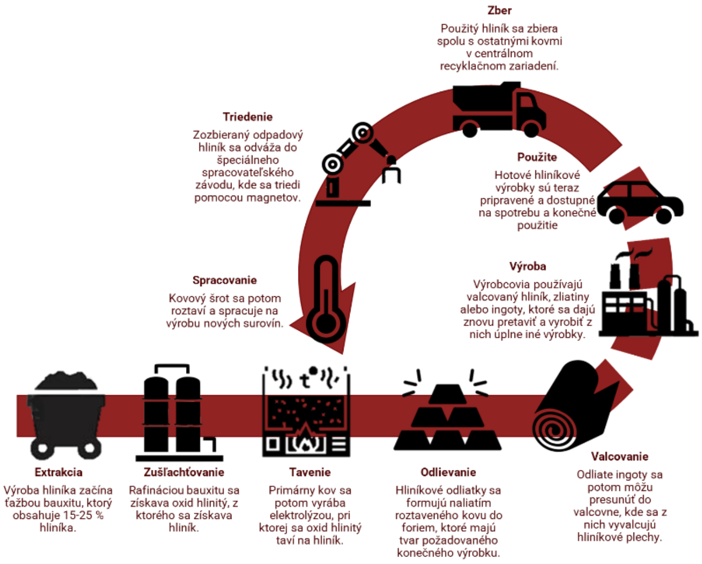

Obr. 7 *Životný cyklus hliníka*

Z energetického a environmentálneho hľadiska prináša hliník výrazné výhody. Výroba sekundárneho hliníka spotrebuje približne 5–10 % energie potrebnej na primárnu výrobu, čím sa významne znižujú emisie skleníkových plynov a celkový environmentálny dopad. Zvyšovanie podielu recyklovaného hliníka vo výrobkoch ako sú vozidlá, je dôležitým nástrojom na znižovanie dopadov počas životného cyklu, najmä keďže v elektrických vozidlách rastie podiel „zabudovaných“ emisií spojených s materiálmi a batériami [9,10,12–14,16].

V automobilovom sektore je recyklácia hliníka podporená vysokou mierou zberu a zavedenou infraštruktúrou tohto zberu. Vyradené vozidlá predstavujú významný zdroj hliníkového šrotu, pričom dôležitým zdrojom je aj pred-spotrebiteľský šrot z výroby, ktorý je možné recyklovať priamo. V Európe je značná časť hliníka používaného v automobiloch recyklovaná po ukončení životnosti vozidla a podiel recyklovaného hliníka v nových zliatinách na odliatky postupne rastie. Z ekonomického hľadiska je recyklovaný hliník atraktívny, keďže znižuje náklady a zmenšuje závislosť od výkyvov na trhu primárneho hliníka [16,17,19].

Recyklácia hliníka však prináša aj metalurgické výzvy. Pri využívaní zmiešaného a post-spotrebiteľského šrotu sa do zliatin dostávajú nežiadúce sprievodné prvky, ako železo, meď či zinok, ktoré je počas tavenia ťažké alebo ekonomicky nevýhodné odstrániť. Tvárnené zliatiny vyžadujú prísnu kontrolu zloženia a sú výrazne závislé od primárneho hliníka. Naopak, zliatiny na odliatky sú tolerantnejšie voči odchýlkam zloženia a predstavujú hlavný „nositeľ“ recyklovaného hliníka, najmä v zliatinách Al–Si–Mg v automobilovom priemysle [20-23].

Hodnotenia životného cyklu ukazujú, že environmentálne prínosy závisia nielen od množstva recyklovaného materiálu, ale aj od účinného zberu, triedenia a recyklačných postupov zohľadňujúcich konkrétny typ zliatiny. Uzavretá slučka recyklácie (closed-loop), pri ktorej sa šrot vracia do rovnakých alebo príbuzných zliatin, prináša najväčšie výhody vďaka nižším požiadavkám na spracovanie. V praxi však často prevažuje otvorená recyklácia (open-loop), pri ktorej sa šrot pretavuje do „generických" zliatin, čo síce maximalizuje materiálové využitie, no zároveň zhoršuje problém nežiadúcich sprievodných prvkov [18,22,23].

S pokračujúcou implementáciou princípov cirkulárnej ekonomiky sa očakáva ďalší nárast využívania recyklovaného hliníka. Elektrické vozidlá vo veľkej miere využívajú hliníkové odliatky pre konštrukčné a funkčné diely, ktoré často nevyžadujú ultračisté zliatiny, no musia spĺňať prísne mechanické požiadavky. Správne navrhnuté sekundárne zliatiny môžu vyvážiť udržateľnosť, náklady a výkonnosť, pokiaľ sú obmedzenia spôsobené recykláciou jasne pochopené a riadené [6,11,15].

3. Sekundárne zliatiny A356 pre automobily a elektrické vozidlá

Spomedzi zliatin na odliatky je A356 (AlSi7Mg0,3) jednou z najrozšírenejších v automobilovom priemysle vďaka priaznivej kombinácii vlastností, ako sú zlievateľnosť, pevnosť, korózna odolnosť a recyklovateľnosť. Z hľadiska recyklácie je A356 významná najmä preto, že zliatiny Al–Si–Mg predstavujú hlavný zdroj sekundárneho hliníka zo zmiešaných tokov šrotu (pred- aj post-spotrebiteľských) [20-23].

Rozsiahle priemyselné využitie zliatiny A356 súvisí s jej vlastnosťami a možnosťou tepelného spracovania. Kremík zlepšuje tekutosť taveniny a znižuje zmršťovanie, čo umožňuje výrobu zložitých odliatkov s dobrou rozmerovou presnosťou. Horčík umožňuje vytvrdzovanie (precipitačné spevnenie) pri tepelnom spracovaní typu T6. Táto kombinácia umožňuje prispôsobiť mechanické vlastnosti požiadavkám konkrétnej aplikácie, čo robí A356 vhodnou pre automobilové diely vyžadujúce kompromis medzi pevnosťou a výrobnou efektívnosťou [20,21].

Prechod na elektrické vozidlá ešte viac zvýraznil význam zliatiny A356 a jej recyklácie. Elektrické vozidlá využívajú hliník napríklad v krytoch batérií, odliatkoch pre invertory a v podvozkových konštrukciách. Tieto komponenty (Obr. 2) vyžadujú dobrú zlievateľnosť, tepelnú stabilitu a koróznu odolnosť [6,11,15].


a) b)

Obr. 8 *Príklady využitia sekundárnej zliatiny A356: a) Konektor nabíjacej pištole pre elektrické vozidlá; b) Kryt batérie elektromobilu [25,26]*

Zvýšené využívanie recyklovaného hliníka v A356 však prináša výzvy spojené s prítomnosťou nežiadúcich sprievodných prvkov v sekundárnych zliatinách. Zvyškovým prvkom, ako železo a meď, sa v sekundárnom hliníku nedá vyhnúť a výrazne ovplyvňujú mikroštruktúru a mechanické vlastnosti, a tým aj prevádzkovú spoľahlivosť. Tieto recykláciou indukované zmeny materiálu stanovujú praktické limity na podiel recyklovaného materiálu v odliatkoch A356 a vyžadujú cielený návrh zliatiny a technologických podmienok, aby sa zabezpečil spoľahlivý výkon v automobiloch a elektrických vozidlách [11,15,24].

4. Nežiadúce sprievodné prvky a mitigačné stratégie v zliatinách A356

Rastúce využívanie recyklovaného hliníka v zliatinách A356 nevyhnutne vedie k akumulácii nežiadúcich sprievodných prvkov (nečistôt). Spomedzi nich je najkritickejšie železo. Do zliatiny sa dostáva najmä zo zmiešaných tokov šrotu (pred- aj post-spotrebiteľských) a počas opätovného tavenia ho nie je možné ekonomicky odstrániť. Keďže hliník je možné recyklovať opakovane, obsah železa má tendenciu narastať, čím sa kontrola nežiadúcich sprievodných prvkov stáva kľúčovým obmedzením pri využití sekundárnej zliatiny A356 v aplikáciách elektrických vozidiel [22,23].

V zliatinách Al–Si–Mg má v hliníkovej matrici železo obmedzenú rozpustnosť a počas tuhnutia vytvára krehké železité intermetalické fázy, napríklad β-Al_5 FeSi, ktoré znižujú únavovú životnosť a pôsobia ako koncentrátory napätia podporujúce iniciáciu trhlín. Okrem toho môžu železité fázy vytvárať mikrogalvanické články s hliníkovou matricou, čo urýchľuje lokálnu koróziu (najmä v prostredí obsahujúcom chloridy). Tieto efekty sú kritické pre konštrukčné diely vystavené cyklickému zaťaženiu a požiadavkám na dlhú životnosť [20,26].

Na zmiernenie negatívneho vplyvu železitých fáz sa skúmajú a využívajú legovacie stratégie, najmä pridávanie mangánu. Mangán mení morfológiu železitých intermetalických fáz a podporuje tvorbu kompaktnejších, menej škodlivých fáz typu α-Al_{15} $(Fe,Mn)_3$ Si_2 , ktoré môžu mať kostrovitú alebo tzv. „Chinese-script“ morfológiu. Tieto fázy preukázateľne znižujú účinok koncentrácie napätia a sú menej nepriaznivé pre mechanické vlastnosti [26,27].

Účinnosť mangánu však závisí od pomeru Mn/Fe, celkovej úrovne nežiadúcich sprievodných prvkov a podmienok tuhnutia. Nadmerné pridávanie mangánu môže zvýšiť celkový objem intermetalických fáz, čo negatívne ovplyvňuje zlievateľnosť a húževnatosť. Navyše, úplná neutralizácia negatívnych účinkov železa pri výrobe sekundárnych zliatin nie je dosiahnuteľná. Priemyselná prax sa preto zameriava na optimalizáciu chemického zloženia zliatiny tak, aby sa dosiahla prijateľná rovnováha medzi obsahom recyklovaného materiálu, mikroštruktúrnou stabilitou a požiadavkami na výkon [23,26,27].

Celkovo predstavujú železité intermetalické fázy v sekundárnych hliníkových zliatinách hlavné obmedzenie pre využitie sekundárnej A356 v náročných automobilových a elektrických aplikáciách. Ak sú však recykláciou indukované nežiadúce sprievodné prvky riadené prostredníctvom návrhu zliatiny a technologickej kontroly, zliatiny A356 zostávajú ekonomicky aj environmentálne výhodným materiálom pre konštrukčné komponenty.

5. Záver

Rastúci dôraz na odľahčovanie konštrukcií a princípy cirkulárnej ekonomiky zvýraznil význam hliníkových zliatin v automobilovom priemysle. Recyklácia hliníka zohráva kľúčovú úlohu pri znižovaní emisií skleníkových plynov a energetickej náročnosti, pričom zliatiny na odliatky predstavujú hlavný spôsob začlenenia sekundárneho hliníka do automobilových komponentov. Zliatina A356 je v tomto smere zásadná vďaka priaznivej kombinácii zlievateľnosti, mechanických vlastností a recyklovateľnosti.

Použitie sekundárnej zliatiny A356 prináša ekonomické aj environmentálne prínosy, avšak jej vlastnosti sú limitované recykláciou indukovanými nečistotami, najmä železom. Tvorba železitých intermetalických fáz predstavuje hlavný problém, keďže znižuje únavovú a koróznu odolnosť v náročných automobilových a elektromobilových aplikáciách.

Legovanie mangánom poskytuje čiastočne účinný spôsob zmiernenia negatívnych účinkov železa tým, že mení morfológiu železitých fáz a umožňuje čiastočné zlepšenie mechanických vlastností. Úplné odstránenie obmedzení spojených so zvýšením obsahom železa však pri vysoko recyklovaných zliatinách spravidla nie je možné, čo zdôrazňuje potrebu návrhu zliatiny založeného na požadovanom výkone.

Celkovo predstavujú sekundárne zliatiny A356 udržateľné materiálové riešenie pre široké spektrum automobilových aplikácií, pokiaľ sú recykláciou indukované obmedzenia adekvátne riadené. Pre ďalšie rozšírenie využitia recyklovaného hliníka v mobilite budúcnosti bude nevyhnutný vývoj zliatin tolerantných voči nežiadúcim sprievodným prvkom, zlepšenie triedenia šrotu a návrh komponentov prispôsobený konkrétnej aplikácii.

Poďakovanie

Tento výskum bol podporený Ministerstvom školstva, vedy, výskumu, vývoja a mládeže SR projektom VEGA 1/0461/24 "Štúdium novej generácie sekundárnych (recyklovaných) Al-zliatin".

Zdroje

[1]Raabe, D., Tasan, C.C., Olivetti, E.A., Strategies for improving the sustainability of structural metals, Nature, 575, 64–74, 2019.
[2]Hirsch, J., Recent development in aluminium for automotive applications, Light Metal Age, 78(3), 22–31, 2014.
[3]European Aluminium, Sustainability Roadmap for the European Aluminium Industry, European Aluminium Association, Brussels, 2018.
[4]Miller, W.S., Zhuang, L., Bottema, J., et al., Recent development in aluminium alloys for the automotive industry, Materials Science and Engineering A, 280(1), 37–49, 2000.
[5]Kaufman, J.G., Introduction to Aluminum Alloys and Tempers, ASM International, Materials Park, OH, USA, 2000.
[6]Luo, A., Recent advances in light metals and manufacturing for automotive applications, CIM Journal, 12(11), 2021.
[7]Hirsch, J.R., Aluminium in Innovative Light-Weight Car Design, Materials Transactions, 52(5), 2011.
[8]Paraskevas, D., Kellens, K., Dewulf, W., Duflou, J.R., Environmental modelling of aluminium recycling: A life cycle assessment approach, Resources, Conservation & Recycling, 77, 46–56, 2013.

[9] Ducker Worldwide, Automotive Aluminium Study: Global Aluminium Content in Cars, Ducker Worldwide LLC, Detroit, MI, USA, 2016.
[10] Das, S., The life-cycle impacts of aluminum body-in-white automotive material, International Journal of Life Cycle Assessment, 16(3), 268–279, 2011.
[11] Miller, W.S., Automotive Materials and Manufacturing, SAE International, Warrendale, PA, USA, 2014.
[12] Ellingsen, L.A.-W., Singh, B., Strømman, A.H., The size and range effect: Life-cycle greenhouse gas emissions of electric vehicles, Journal of Industrial Ecology, 20(1), 76–89, 2014.
[13] Kim, H.C., Wallington, T.J., Arsenault, R., Bae, C., Ahn, S., Lee, J., Cradle-to-gate emissions from a commercial electric vehicle lithium-ion battery, Environmental Science & Technology, 50(14), 7715–7722, 2016.
[14] Hao, H., Qiao, Q., Liu, Z., Zhao, F., Impact of vehicle electrification and lightweighting on energy use and GHG emissions, Applied Energy, 188, 155–168, 2017.
[15] Hirsch, J., Lightweight aluminium for electric vehicles, Light Metals, 2019, 1095–1101, 2019.
[16] European Aluminium, Recycling Aluminium – A Pathway to a Sustainable Economy, European Aluminium Association, Brussels, 2016.
[17] Schlesinger, M.E., Aluminum Recycling, CRC Press, Boca Raton, FL, USA (2013).
[18] International Aluminium Institute, Life Cycle Inventory Data for Aluminium Production, IAI, London, UK, 2018.
[19] Gaustad, G., Olivetti, E., Kirchain, R., Improving aluminum recycling: A material flow analysis, Resources Policy, 58, 166–178, 2018.
[20] Taylor, J.A., The effect of iron in Al–Si casting alloys, Progress in Materials Science, 57(4), 701–760, 2004.
[21] Campbell, J., Complete Casting Handbook: Metal Casting Processes, Metallurgy, Techniques and Design, 2nd ed., Butterworth-Heinemann, Oxford, UK, 2015.
[22] Lumley, R., Fundamentals of Aluminium Metallurgy: Production, Processing and Applications, Woodhead Publishing, Cambridge, UK, 2010.
[23] Makhlouf, M.M., Evolution of a recycled aluminium alloy deformed by the equal channel angular pressing process, Journal of Minerals, Metallurgy and Materials, 19(11), 1016, 2016.
[24] Hirsch, J., Recent development in aluminium for automotive applications, Light Metal Age, 78(3), 22–31, 2014.
[25] www.made-in-china.com. A356 Aluminium Alloy Metal Casting, Gravity Casting, Die Casting for Electric Vehicle Charging Gun Metal Butt Connectorm, 2025.
[26] Šurdová, Z., Tillová, E., Kuchariková, L., Mikolajčík, M., The Study of Porosity in A356 Secondary Aluminium Alloys with Higher Iron Content. System Safety: Human - Technical Facility – Environment. 6(1). pp. 430-438, 2025.
[27] Samuel, A.M., Samuel, F.H., Doty, H.W., Observations on the formation of β-Al$_5$FeSi phase in 319 type Al-Si alloys, Journal of Materials Science**,** 31, 5529-5539, 1996.

29th International Seminar of Ph.D. Students

SEMDOK 2026

Western Tatras – Zuberec, Slovak Republic
February, 4 to February 6, 2026

PRELIMINARY STUDIES OF HYBRID COATINGS OBTAINED ON AZ91 MAGNESIUM ALLOY SUBSTRATE

Leon Sułkowski[1], Rafał Orłowski[1], Filip Wolański[1], Ewa Jonda[2*], Małgorzata Dziekońska[2], Daniel Kajánek[3]

[1] Students of the Andrzej Strug 5th General Secondary School with Bilingual Departments in Gliwice, Górnych Wałów 29 St., 44100 Gliwice, Poland.

[2] Department of Engineering Materials and Biomaterials, Faculty of Mechanical Engineering and Technology, Silesian University of Technology, 18a Konarskiego St., 44 100 Gliwice, Poland.

[3] Research Centre of the University of Žilina, University of Žilina, Univerzitná 8215/1 St., 01026 Žilina, Slovakia.

**corresponding author: ewa.jonda@polsl.pl, +48322372606, Konarskiego 18A St., 44100 Gliwice, Poland.*

1. Introduction

Advances in technology are driving an increasing demand for surface layers with enhanced functional and technological properties. Methods such as plasma electrolytic oxidation (PEO) and high velocity oxy-fuel (HVOF) are widely used to improve the reliability and extend the service life of both new and refurbished machine components, representing efficient surface engineering approaches [1-4]. In particular, PEO is an effective surface treatment process for light metals and their alloys, providing corrosion protection through the formation of a hard, ceramic-like coating on the substrate [5].

The PEO process has been an established coating technology for over 30 years and has been extensively applied in commercial settings throughout most of this time. It exhibits several characteristics that make it particularly distinctive and potentially highly advantageous. One such feature is the continuous restructuring of the coating across its entire thickness, which reduces residual stresses and improves uniformity throughout the layer. Additionally, since the coatings are formed through partial consumption of the substrate, they exhibit excellent interfacial adhesion. Nevertheless, the resulting coatings are not entirely free from defects; in fact, they typically contain signific porosity, micro-cracks, inclusions, and other imperfections [6–9]. On the other hand, thermal spraying is a widely used method for depositing coatings, allowing the formation of metallic, carbide, ceramic, and composite layers with nearly any chemical or phase composition on appropriately prepared substrates. This technique enables the production of coatings with enhanced properties, such as low oxidation, reduced porosity, and high adhesion [10-15].

The main aim of the present study was to investigate hybrid coatings applied to magnesium alloy substrates and to characterize their functional properties. Magnesium alloys are inherently prone to low resistance to abrasive wear and corrosion, which poses a significant technical challenge and limits their broader application across various industrial sectors.

2. Materials and methodology

AZ91 magnesium alloy was selected as the substrate material. In the first step, a coating was produced using the PEO (Plasma Electrolytic Oxidation) method. Prior to PEO treatment, AZ91 alloy samples were ground with #1200 SiC abrasive paper. The PEO coating was prepared in a phosphate - based electrolyte bath, consisting of $Na_3(PO_4)$ x $12H_2O$ and KOH dissolved in deionized water, with a pH of 12.5 ± 0.5.

For the preparation of the PEO coating, a two - electrode system was used consisting of the AZ91 alloy connected as the anode and a stainless - steel plate connected as the cathode supplied by a Keysight N8762A (USA) DC power source. During the coating process, a constant distance of 10 cm between electrodes was maintained, and a laboratory stirrer (Heidolph Instruments, Schwabach, Germany) was employed to improve the distribution of reactants over the sample surface. The temperature of the electrolyte bath did not exceed 50°C and was maintained using a water - cooling system. The concentrations of $Na_3(PO_4)$ x $12H_2O$ was 12 g/L and a current density of 0.05 A/cm^2 was applied to the sample. The concentration of KOH was set to 1g/L in all electrolyte solutions. The treatment time of PEO treatment was set to 5 min.

In the second step cermet coatings were deposited onto the AZ91 magnesium alloy substrate covered with the PEO coating. The feedstock material was a commercial powder with the chemical composition Cr_3C_2-25wt.%NiCr (Amperit 588.074, Häganäs) with the chemical composition (element, wt.%): C-9÷11, Fe-max. 0.5, Ni-18÷22, O_2-max.0.6 and Cr-balance. According to the manufacturer, the declared particle size range was − 45 + 15 μm for powder, and the mean volume-to-surface diameter, $d_{VS}50$ was 35 μm. Moreover, the particle size distribution was monomodal and relatively narrow. The cermet coatings were deposited by the HVOF method with a MECEL Hipo Jet2700 system. Propane and oxygen were used as the fuel, whereas nitrogen served as the carrier gas. During spraying, the maximum flame temperature reached approximately 3250 K.

The microstructure of the sprayed coatings was examined on polished cross - sections using a scanning electron microscope (SEM, Supra 35, Zeiss, Oberkochen, Germany), while the chemical composition was analysed by energy-dispersive X-ray spectroscopy (EDS) (Supra 35, Zeiss, Oberkochen, Germany). The areas selected for the EDS measurements were randomly distributed across the coating. The topography and thickness of the sprayed coatings were also investigated by SEM. The porosity of the PEO+HVOF coatings was estimated according to the ASTM E2109-01 standard and quantified using the open-source software ImageJ (version 1.50i). Surface roughness in the sprayed coating was determined using a stylus profilometer, in accordance with ISO 4288 standard. For each sample five measurements were carried out and average, as well as standard deviation values were calculated.

3. Results and discussion

The topography of deposited samples confirmed the typical morphology of HVOF-sprayed coatings. The coating surface is relatively smooth, without craters or unexpected material peaks. Some observed irregularities are probably related to the carbide particles which possess high melting point and cannot be fully melted in the flame (Fig. 1).

Metallographic examinations revealed that samples exhibited a compact and dense structure (Fig. 2 a, b). However, a small number of pores and micro - cracks were observed in the microstructure. The presence of partially melted particles in the coating can be attributed to the short residence time of the powder particles in the HVOF spray flame, leading to the formation of pinholes and cracks. The occurrence of cracks and voids can reduce coating durability, promote crack propagation, and eventual delamination. The average thickness of the as sprayed coatings was about 128.5 ± 6 µm.

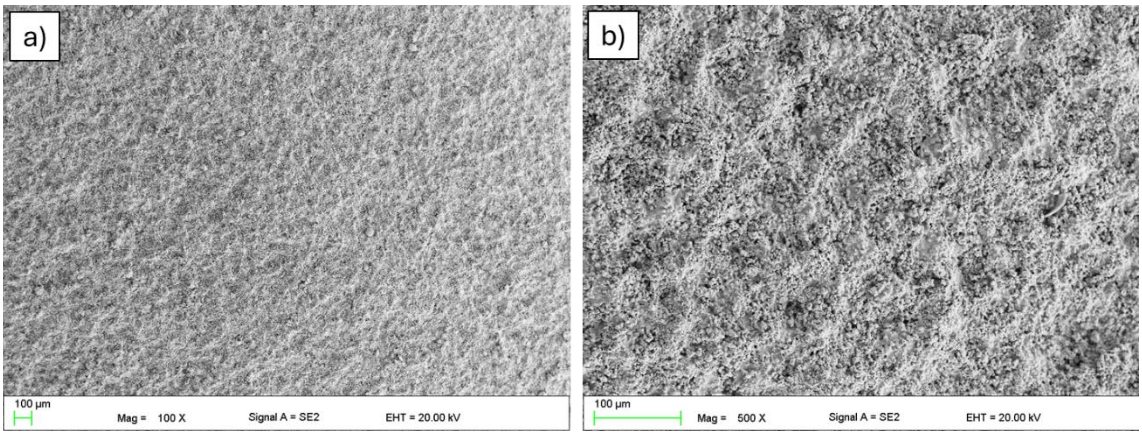

Fig. 1. *The surface topography of the sprayed coatings (a, b) (SEM)*

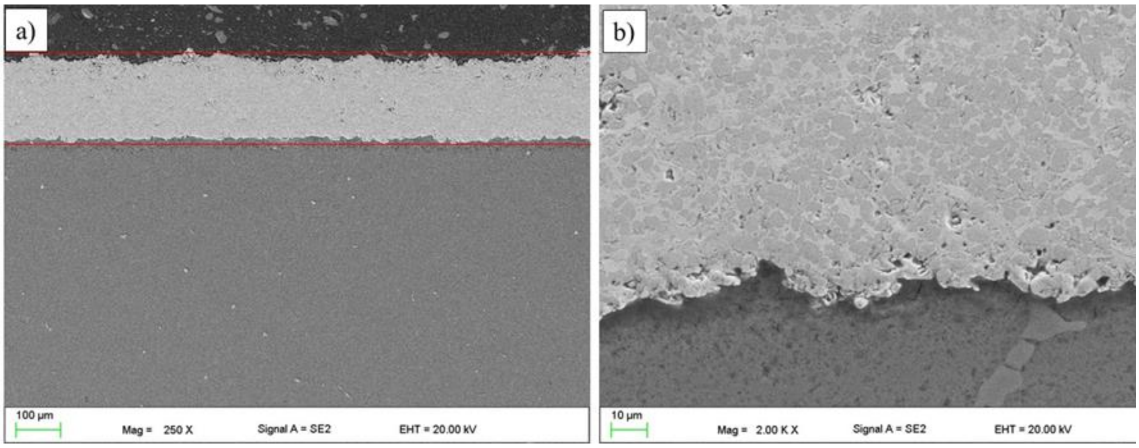

Fig.2. *The SEM image of coatings' cross-section*

Elemental distribution maps of the analysed area confirmed the presence of elements in the PEO+HVOF coating, corresponding to the components of both coatings, which suggests that it was possible to make a hybrid coating (Fig. 3 a, b).

Figure 4a shows the microstructure, 4b presents chemical composition of the deposited PEO +HVOF coating determined by EDS and 4c shows distribution diagram of the elements in the analysis area of the coating. The elemental composition of the PEO +HVOF coating was evaluated using the EDS analysis. As expected, all PEO coatings are composed of O, P, Mg and a small amount of Al, Na, Si, and the O content is approximately 46 %. In contrast, HVOF coatings consist of elements originating from the coating material: Cr, C and Ni. In both cases the presence of Mg and Al elements in the coatings is attributed to the magnesium alloy substrate. The porosity assessment indicated that it is possible to obtain relatively dense coatings, which obtained porosity value 2.8±0.5%.

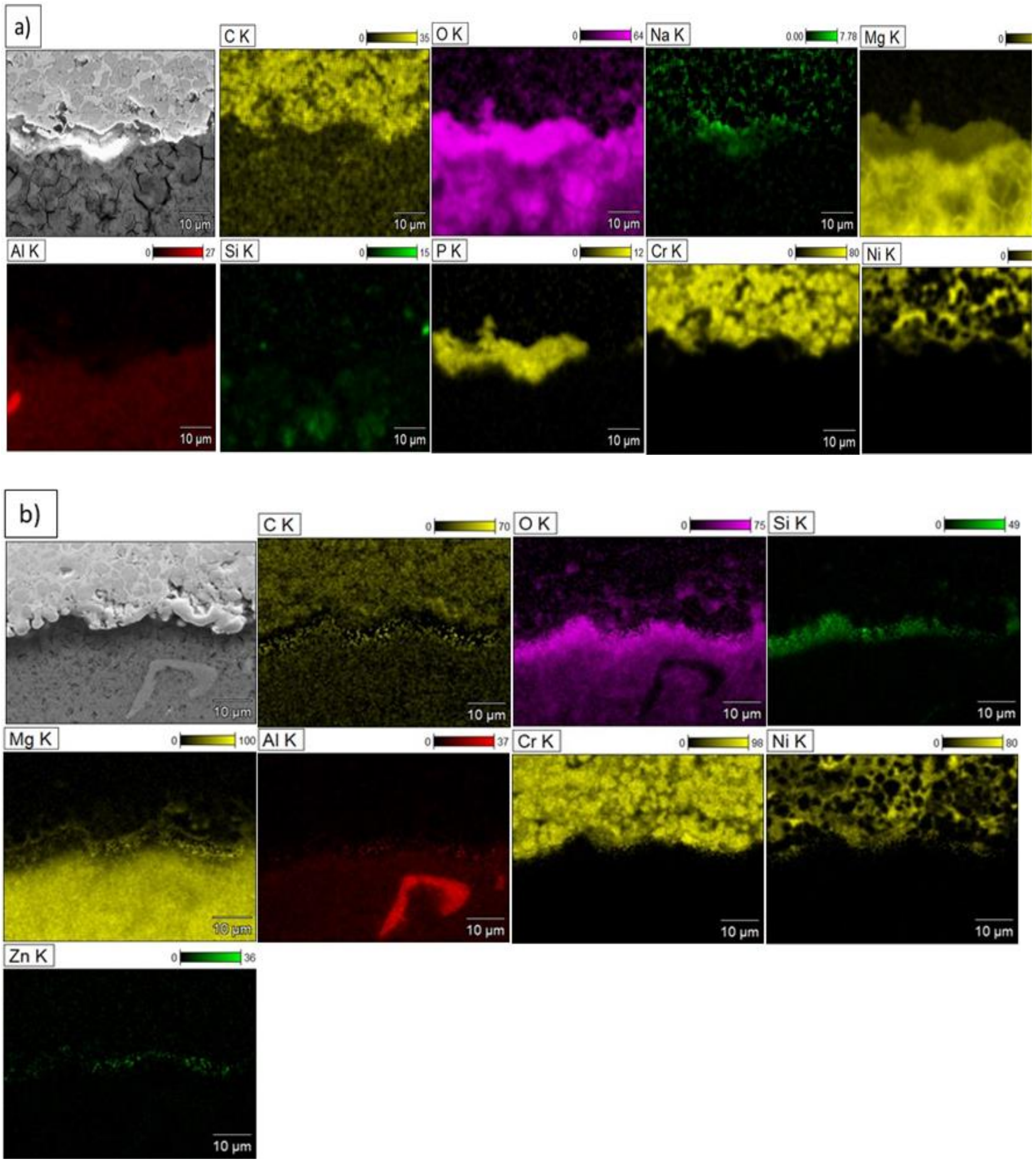

Fig.3. *Elemental distribution maps of the analysed area of the PEO+HVOF coating*

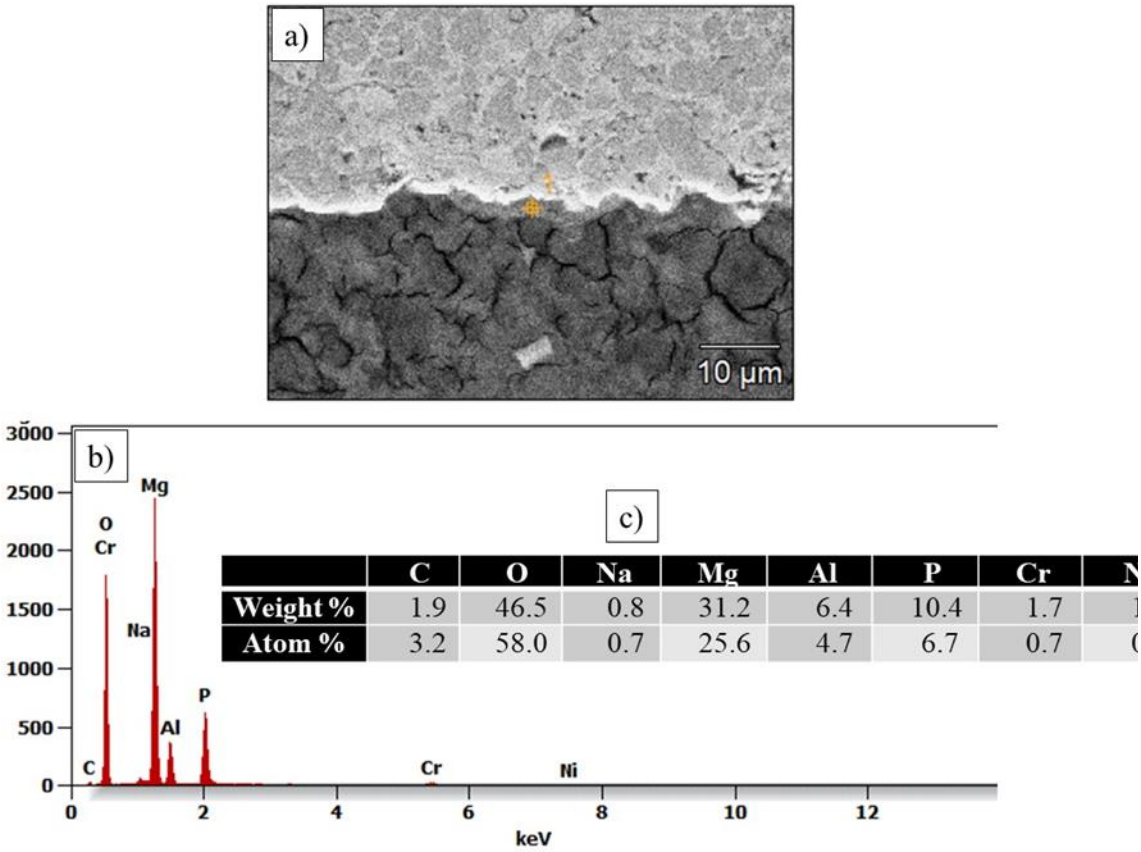

	C	O	Na	Mg	Al	P	Cr	N
Weight %	1.9	46.5	0.8	31.2	6.4	10.4	1.7	1
Atom %	3.2	58.0	0.7	25.6	4.7	6.7	0.7	(

Fig.4. *The SEM microstructure of hybrid coatings' (a), and EDS analysis of the chemical composition from the analysed point 1 (b), and element distribution diagram of the elements in the analysis area of the coating (c)*

4. Conclusions

Based on the preliminary results obtained in this study, it was demonstrated that the formation of hybrid coatings using plasma electrolytic oxidation (PEO) and high velocity oxy-fuel (HVOF) processes is feasible. Such coatings can serve as an alternative to other conventional surface engineering methods aimed at improving or restoring the surface properties of machine and equipment components. A key factor determining the operational performance of the produced coatings is the proper selection of deposition process parameters and the materials used for their fabrication. In particular, the high flame temperature during thermal spraying and the nozzle-to-substrate distance play a critical role. Excessively high flame temperatures combined with insufficient spraying distance may lead to degradation of the PEO coating during the spraying process. The investigations presented in this work are of a fundamental nature; however, the possibility of developing new hybrid coatings on light structural alloys, which enhance mechanical properties, corrosion and wear resistance, and reduce production costs, makes this topic highly relevant and warrants further, more extensive research.

Acknowledgment

The present study was manufactured as part of the activities of project within project-oriented education - Project Base Learning (PBL) implemented with secondary school students as part of the Excellence Initiative – Research University programme.

References

[1] Hadzima,B., Kajánek, D., Jambor, M., Drábiková, J. , Brezina, M., Buhagiar, J., Pastorková, J. and Jacková, M.: PEO of AZ31 Mg Alloy: Effect of Electrolyte Phosphate Content and Current Density. Metals. Vol. 10, pp. 1521, 2020.

[2] Wu, T., Blawert, C., Lu, X., Serdechnova, M., Zheludkevich, L. M.: Difference in formation of plasma electrolytic oxidation coatings on MgLi alloy in comparison with pure Mg. Journal of Magnesium and Alloys. Vol. 9, No. 5, pp. 1725-1740, 2021.

[3] Pawlowski, L.: The science and engineering of thermal spray coatings, J. Wiley and sons, Chichester, West Sussex, 2008.

[4] Jonda, E., Łatka, L., Maciej, A., Khozhanov, A.: Investigations on the Microstructure and Corrosion Performance of Different WC-Based Cermet Coatings Deposited by High Velocity Oxy Fuel Process onto Magnesium Alloy Substrate. Advances Science Technology Research Journal.Vol.17, pp.25-35, 2023.

[5] Zhu, S., Wang, Ch., Li, X.,Pan, L., Liu, W., Peng, J.: Corrosion behavior and formation mechanism of plasma electrolytic oxidation coatings on 1060 aluminum alloy in $Si(OC_2H_5)_4$-$(NaPO_3)_6$-NaOH electrolyte. Surface and Coatings Technology. Vol. 520, No. 15, pp. 133015, 2026.

[6] Clyne, T.W., and Troughton, S.C.: A review of recent work on discharge characteristics during plasma electrolyticoxidation of various metals. International Materials Reviews. Vol. 64, No. 3, pp. 127-162, 2019.

[7] Gamba, M., Cristoforetti, A., Fedel, M., Ceriani, F., Ormelles, M., Brenna, A.: Plasma Electrolytic Oxidation (PEO) coatings on aluminum alloy 2024: A review of mechanisms, processes, and corrosion resistance enhancement. Applied Surface Science Advances. Vol. 26, pp. 100707, 2025.

[8] Fattah-Alhosseini, A., Salimi, H., Karbasi, M.: A comprehensive overview in improving corrosion resistance of Mg alloys: Enhancing protective coatings with plasma electrolytic oxidation and superhydrophobic coatings. Journal of Magnesium and Alloys. Vol. 13, No. 4,pp. 1386-1404, 2025.

[9] Li, Ch., Li, Y., Zhang, T., Wang, F.: Effect of adding K_2TiF_6 and K_2ZrF_6 to neutral electrolyte on the performance of plasma electrolytic oxidation coatings on AZ91 Mg alloy. Journal of Materials Research and Technology. Vol. 30, pp. 7684-7696, 2024.

[10] Liu, Ch., Lu, K., Li, Y., Chen, Q., Zhang, T., Wang, F.: Influence of post-treatment process on corrosion and wear properties of PEO coatings on AM50 Mg alloy. Journal of Alloys and Compounds. Vol. 870, pp. 159462, 2021.

[11] Morelli, S., Rombolà, G., Bolelli, G., Lopresti, M., Puddu, P., Boccaleri, E., Seralessandri, L., Palin, L., Testa, V., Milanesio, M., Lusvarghi, L.: Hard ultralight systems by thermal spray deposition of WC-CoCr onto AZ31 magnesium alloy. Surface and Coatings Technology. Vol. 451, pp. 129056, 2022.

[12] Ozbek, Y.Y.,Ozgurluk, Y., Odabas, O., Karaoglanli, A. C.: Thermal degradation resistance of HVOF-sprayed Cr_3C_2–NiCr composite coatings under oxidizing and corrosive environments. Surface and Coatings Technology. Vol. 513, pp. 132456 2025.

[13] Subbiah, R., Arun, A., Lakshmi, A.,Naga Sai, A., Harika, A., Ram, N., NSateesh, N.: Experimental Study of Wear Behaviour on Al-2014 Alloy Coated with Thermal Spray HVOF (HighVelocity Oxy-Fuel) and Plasma Spray Process– Review. Vol. 18, No. 7, pp. 5151-5157, 2019.

[14] Li, Z., Li, Y., Li, J., Li, F., Lu, H., Du, J., et al.: Effect of NiCr content on the solid particle erosion behavior of NiCr-Cr_3C_2 coatings deposited by atmospheric plasma spraying. Surface and Coatings Technology. Vol. 381:125144, 2020.

[15] Wei, Z., Cui, D., Wei, Z., Hong, S.: HVOF spray of Cr_3C_2–NiCr coating for enhancing the corrosion resistance of nickel aluminium bronze in 3.5% NaCI solution with different sulphide concentrations. Journal of Materials Research Technology. Vol. 23, pp. 869–881, 2023.

29th International Seminar of Ph.D. Students

SEMDOK 2026

Western Tatras – Zuberec, Slovak Republic
February, 4 to February 6, 2026

ANALÝZA MECHANICKEJ STABILITY LASEROVÝCH ZVAROVÝCH SPOJOV OCELE S960MC V PODMIENKACH ELEKTROLYTICKÉHO VODÍKOVANIA

Lukáš Šikyňa[1*]**, František Nový**[1]**, Martin Slezák**[1]**, Veronika Chvalníková**[1]
[1] Strojnícka fakulta, Katedra materiálového inžinierstva, Žilinská univerzita v Žiline, Univerzitná 8215/1, 010 26 Žilina, Slovenská republika
**lukas.sikyna@fstroj.uniza.sk, +421 41 513 2632*

1. Úvod

Vysokopevné ocele typu S960MC sú kľúčovým materiálom pre efektívne odľahčené konštrukcie, avšak ich dlhodobá mechanická stabilita môže byť ohrozená degradáciou spôsobenou vodíkom, a to najmä v kritických zónach zvarových spojov. Práve tepelne ovplyvnená oblasť (TOO), charakteristická výraznou mikroštruktúrnou heterogenitou a prítomnosťou zvyškových napätí, predstavuje primárne miesto pre akumuláciu vodíka a následnú iniciáciu trhlín. Hoci technológia laserového zvárania (LBW) minimalizuje tepelné ovplyvnenie, lokálne mikroštruktúrne gradienty v tejto oblasti môžu za špecifických elektrochemických podmienok stále viesť k vodíkom asistovanému praskaniu (HAC) [1, 2]. Difúzia vodíka do materiálu, či už počas prevádzky alebo vplyvom povrchovej expozície, spôsobuje degradáciu plastických vlastností a vyvoláva predčasný lom, čo je obzvlášť kritické pri oceliach s citlivou martenzitickou alebo bainitickou štruktúrou [3, 4]. Predkladaná práca sa preto zameriava na analýzu stability mechanických vlastností a náchylnosti na porušenie laserových zvarov S960MC v závislosti od intenzity elektrolytického nasycovania. Cieľom je prostredníctvom mechanických skúšok a fraktografie identifikovať vplyv vodíka na degradačné mechanizmy a morfológiu lomu.

2. Experimentálny materiál

Ako experimentálny materiál bola zvolená termomechanicky spracovaná vysokopevná oceľ S960MC (Strenx® 960MC) vo forme plechov s hrúbkou 4 mm. Tento materiál je charakteristický vysokou pevnosťou, pričom jeho nominálna medza klzu dosahuje 960 MPa a medza pevnosti sa pohybuje v intervale 980 až 1250 MPa pri zachovaní minimálnej ťažnosti 7 % Tab, 1 [5].

Tab. 1 *Mechanické vlastnosti ocele S960MC*

Medza pevnosti Rm [MPa]	Medza klzu Rp0.2 [MPa]	Ťažnosť A5 (%)	Hrúbka [mm]
980-1250	*960*	*7*	*3-10*

Spektrálna analýza GDOES potvrdila zhodu chemického zloženia s normami výrobcu, hoci odhalila mierne vyšší podiel kremíka a mangánu (Tab. 2). Práve tieto prvky môžu zohrávať kľúčovú úlohu pri modifikácii mechanickej odozvy a kinetiky difúzie vodíka v mriežke [6].

Tab. 2 *Nominálne a experimentálne chemické zloženie ocele S960MC (hm. %)*

Prvok	***C***	***Mn***	***Si***	***P***	***S***	***Nb***	***V***	***Ti***
Norma	≤0,12	≤1,30	≤0,25	≤0,12	≤0,010	≤0.05	≤0.05	≤0.05
Merané	0,17	1,38	0,30	0,006	<0.001	<0.001	0,05	0,015

Príprava zvarových spojov prebehla technológiou laserového zvárania (LBW) bez použitia prídavného materiálu, pričom procesné parametre boli optimalizované s cieľom dosiahnuť bezchybné tupé spoje na celej hrúbke prierezu. Aby sa eliminovala povrchová kontaminácia, ktorá by mohla skresliť proces absorpcie vodíka, boli stykové plochy pred zváraním mechanicky upravené a odmastené acetónom. Z takto pripravených zvarencov boli následne vyrezané skúšobné telesá v súlade s normou EN ISO 6892-1, určené na elektrolytické sýtenie a následnú verifikáciu mechanických vlastností.

Tab. 3 *Parametre laserového zvárania*

Výkon laseru [W]	**Rýchlosť posuvu [mm s^{-1}]**	**Poloha ohniska [mm]**	**Prietok ochranného plynu [l min^{-1}]**
3500	*15*	*-4*	*12*

3. Experimentálne metódy

Proces nasycovania vodíkom prebiehal v prostredí vodného elektrolytu zloženého z 1 litra destilovanej vody, 2,8 ml koncentrovanej kyseliny sírovej (96 % H_2SO_4) a 1 g tiokyanatanu draselného (KSCN), pričom metodika vychádzala zo štandardizovaných postupov pre katodické nabíjanie [7]. Experimenty boli realizované pri izbovej teplote, s dôrazom na presnú reguláciu prúdovej hustoty, čo umožnilo skúmať súvislosť medzi absorpciou vodíka a následným skrehnutím materiálu. V elektrickom obvode plnili vzorky funkciu katódy, zatiaľ čo ako anóda slúžila sieťka z platinovaného volfrámu (Obr. 1).

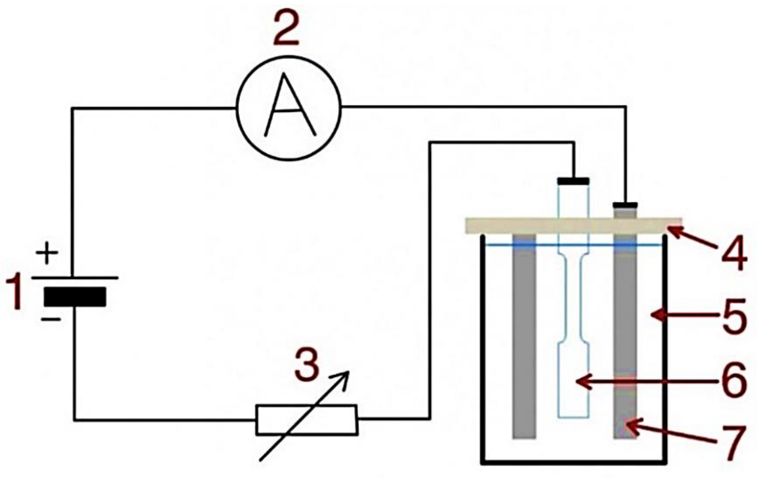

Obr. 1 *Schematický diagram elektrolytického nasycovania vzorky vodíkom*

Zostava experimentálneho zariadenia (Obr. 1) bola tvorená sériovým zapojením zdroja jednosmerného napätia (1), ampérmetra (2) a odporových dekád (3). Samotná vzorka bola v elektrolytickej cele (5) uchytená pomocou nevodivého držiaka (4). Aby sa garantovala presná geometrická hustota prúdu a eliminovali sa nežiaduce účinky rozptylu poľa, do roztoku bola ponorená výlučne definovaná dĺžka meranej časti vzorky (6), pričom sa dbalo na zachovanie odstupu od dna nádoby aj od poplatinovanej anódy (7).

Pre analýzu citlivosti laserových zvarov na vodíkovú degradáciu boli aplikované dve úrovne prúdovej hustoty: 0,5 a 1,0 mA/cm², s dobou expozície stanovenou na 8 hodín. Bezprostredne po ukončení procesu nasycovania boli vzorky podrobené ťahovej skúške. Experimentálny postup bol navrhnutý a realizovaný v súlade s odporúčaniami pre elektrolytické nasýtenie vysokopevnostných ocelí vodíkom [7, 8]. Výsledky získané na vzorkách dotovaných vodíkom boli následne konfrontované s referenčným stavom bez vodíka, čo umožnilo identifikovať a objasniť mechanizmy vedúce ku krehnutiu.

3. Výsledky a diskusia

3.1 Metalografická charakteristika ocele S960MC

Oceľ S960MC, ktorá bola predmetom analýzy, predstavuje mikrolegovaný konštrukčný materiál. Jeho chemické zloženie v kombinácii s procesom termomechanického valcovania a riadeného ochladzovania vedie k formovaniu jemnej martenziticko-bainitickej štruktúry. Kľúčovú úlohu zohrávajú legujúce prvky, najmä titán, ktorý prostredníctvom tvorby jemných precipitátov TiC zvyšuje pevnosť materiálu. Tieto precipitáty zároveň plnia funkciu zjemňovania zrna a pôsobia ako ireverzibilné pasce pre vodík. Pohľad na mikroštruktúru (Obr. 2a)) odhalil v osi plechu súvislý segregačný pás v pozdĺžnom smere. Tento jav je charakteristický pre ocele spracované metódou TMCP a súvisí s minoritnou segregáciou prvkov počas tuhnutia a valcovania. I keď tieto pásy nemajú zásadný vplyv na mechanické vlastnosti, na lokálnej úrovni môžu modifikovať difúziu a zachytávanie vodíka, čo je kritické najmä pri elektrolytickom nasycovaní.

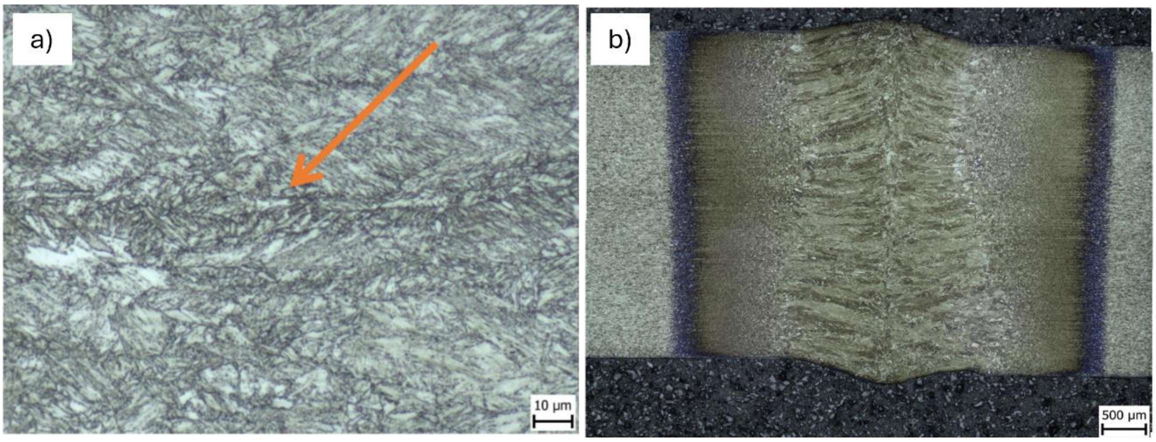

Obr. 2 *Mikroštruktúra ocele S960MC a); Zvarový kov a TOO ocele S960MC po laserovom zváraní b); leptané 3% Nital*

Makroskopický prierez laserového zvaru je dokumentovaný na obr. 2b. Zvarový kov má typickú geometriu pripomínajúcu presýpacie hodiny a je lemovaný úzkymi tepelne ovplyvnenými oblasťami, čo je priamy dôsledok nízkeho tepelného príkonu laserovej technológie. Kým zvarový kov vykazuje čisto martenzitickú štruktúru vzniknutú rýchlym tuhnutím, priľahlá TOO je tvorená špecifickými podzónami v závislosti od teplotného cyklu. Rozhranie medzi taveninou a TOO je ostré, bez výskytu pórovitosti či makrodefektov, čo potvrdzuje integritu spoja a úplný prievar. Detailnejší pohľad na TOO však ukazuje mikroštruktúrny gradient: od hrubozrnného martenzitu (CGHAZ) pri hranici tavenia, cez jemnozrnný martenzit (FGHAZ), až po interkritickú oblasť (ICHAZ) pri základnom materiáli. V interkritickej zóne TOO spôsobila čiastočná austenitizácia vznik heterogénnej zmesi martenzitu, popúšťaného martenzitu a feritu. Práve táto postupná transformácia mikroštruktúry v rámci TOO zapríčiňuje lokálne variácie v tvrdosti a difuzivite vodíka.

3.2 Výsledky skúšky ťahom

Vzorky v referenčnom stave (bez nasycovania), dosahovali stabilné hodnoty medze pevnosti (Rm ≈ 1055 MPa) a medze klzu (Rp0,2 ≈ 970 MPa), pričom rovnomerné predĺženie (A) sa pohybovalo na úrovni 9,2 %. Tieto parametre sú v plnej zhode s nominálnymi vlastnosťami základného materiálu, čo potvrdzuje integritu zvarového spoja a absenciu defektov či zmäkčených zón.

Po expozícii vodíku, došlo k degradácii mechanických vlastností v priamej závislosti od intenzity prúdovej hustoty. Pri aplikácii prúdovej hustoty 0,5 mA/cm^2 klesla priemerná medza pevnosti na hodnotu 967 MPa, čo predstavuje 8 % stratu voči referencii. Ešte kritickejší bol prepad ťažnosti na úroveň 1,1 %, čo signalizuje nástup výrazného vodíkového skrehnutia, hoci medza klzu poklesla len minimálne (931 – 940 MPa). To naznačuje, že prítomnosť vodíka negatívne ovplyvňuje predovšetkým plasticitu materiálu, a nie jeho schopnosť odolávať počiatočnej plastickej deformácii.

Zvýšenie prúdovej hustoty na 1,0 mA/cm^2 viedlo k extrémnej degradácii materiálu. Medza pevnosti sa prepadla do intervalu 388 až 488 MPa, čo zodpovedá strate pevnosti presahujúcej 55 %, pričom hodnoty ťažnosti klesli pod kritickú hranicu 0,4 %. Tento trend nasledovali aj sily pri lome (Fm), čo potvrdzuje predčasný krehký charakter porušenia.

Experimentálne výsledky jednoznačne preukazujú, že vyššia prúdová hustota počas elektrolytického procesu vedie k intenzívnejšej absorpcii vodíka, a tým aj k vyššej náchylnosti laserových zvarov S960MC na skrehnutie. Pozorovaný kolaps ťažnosti a pevnosti korešponduje s mechanizmami vodíkom asistovaného praskania v oblasti taveniny a tepelne ovplyvnenej oblasti, čo je v súlade s poznatkami o správaní mikrolegovaných ocelí pri katodickom nabíjaní [1, 3]. Je zrejmé, že intenzita prúdu funguje ako akcelerátor tohto degradačného procesu.

3.2 Výsledky fraktorgrafie

Fraktografia referenčného spoja bez vplyvu vodíka (obr. 3a)) potvrdila dominanciu tvárneho lomu. Lom neprechádzal cez zvarový kov a tepelne ovplyvnenú oblasť (TOO), čo indikuje mechanickú homogenitu spoja. Väčšiu časť lomovej plochu tvorila hustá sieť jamiek vzniknutých spájaním mikrodutín okolo precipitátov (1 – 3 µm). Táto štruktúra potvrdzuje, že k porušeniu došlo pri vysokom plastickom napätí a bez degradačného pôsobenia vodíka.

V prípade vzoriek nasycovaných prúdom 0,5 mA/cm^2 mal lom zmiešaný charakter. Kým stredová oblasť si zachovala známky plasticity, okraje boli ploché a krehké. Tento jav poukazuje na nerovnomernú distribúciu vodíka s maximálnou koncentráciou pri povrchu v dôsledku elektrochemického nasycovania. Detail lomovej plochy (Obr. 3b) poukazuje na krehké kvázi-štiepenie porušenie s riečnnou morfológiou na fazetách. Globulárne inklúzie fungovali ako pasce pre vodík. V ich okolí dochádzalo k rekombinácií atómov vodíka a iniciácii mikrotrhlín, ktoré sa následne prepojili do štiepnych faziet.

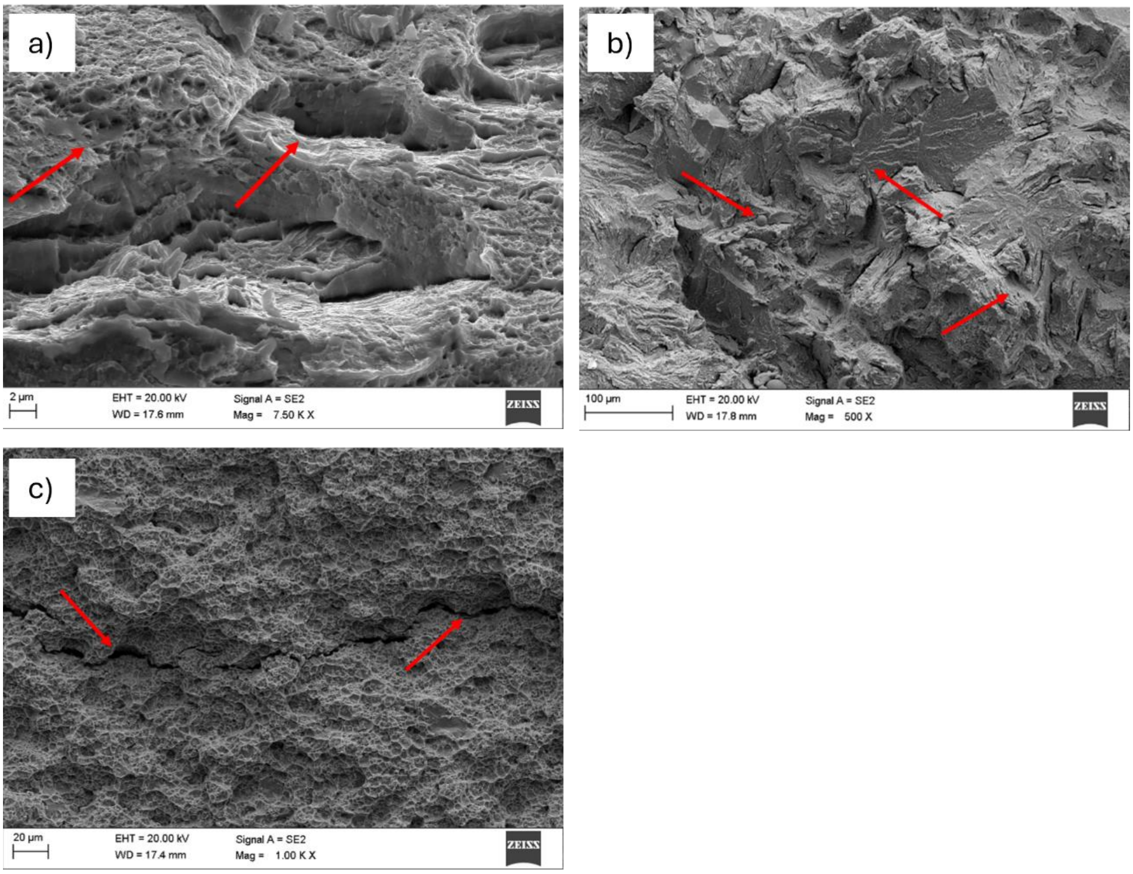

Obr. 3 *Fraktografia laserom zváraného spoja S960MC; bez nasýtenia vodkíkom a); po elektrolytickom nasycovaní vodíkom pri 0,5 mA/cm^2 b); po elektrolytickom nasycovaní vodíkom pri 1,0 mA/cm^2 c); SEM ZEISS SUPRA 35*

Aplikácia maximálnej prúdovej hustoty 1,0 mA/cm^2 viedla k radikálnej zmene na plne krehký lom v celom priereze. Plochý povrch bez známok deformácie a prítomnosť početných sekundárnych trhlín korešpondujú s extrémne nízkou ťažnosťou a pevnosťou zistenou pri ťahovej skúške.

Detailný pohľad (Obr. 3c) potvrdzuje dominanciu mechanizmu vodíkom asistovaného praskania (HAC). Pozorovaná sieť mikrotrhlín a štiepnych faziet spolu s vetvením prasklín indikuje, že vodík spôsobil výrazné oslabenie hraníc zŕn a fázových rozhraní, čo viedlo k interkryštalickému aj transkryštalickému šíreniu lomu.

4. Záver

Výsledky štúdie jednoznačne potvrdzujú, že mechanická stabilita laserových zvarov ocele S960MC je priamo závislá od intenzity elektrolytického nasycovania, pričom so zvyšujúcou sa prúdovou hustotou rapídne rastie náchylnosť na vodíkové skrehnutie. Experimentálne dáta preukázali postupnú degradáciu lomového správania: kým pri nižšom zaťažení (0,5 mA/cm^2) došlo k prechodu od tvárneho lomu k zmiešanému kvázi-štiepeniu, aplikácia prúdu 1,0 mA/cm^2 spôsobila výrazný plasticity a vznik plne krehkého lomu sprevádzaného drastickým poklesom pevnosti.

Poďakovanie

Tento výskum bol podporený Vedeckou grantovou agentúrou Ministerstva školstva, výskumu, vývoja a mládeže Slovenskej republiky VEGA, č. 1/0831/25.

Literatúra

[1] Djukic, M. B., Zeravcic, V. S., Bakic, G. M., Sedmak, A., & Rajicic, B. 2015. Hydrogen damage of steels: A case study and hydrogen embrittlement model. Engineering Failure Analysis, Volume: 58, Pages: 485-498. https://doi.org/10.1016/j.engfailanal.2015.05.017

[2] Lynch, S. 2012. Hydrogen embrittlement phenomena and mechanisms. Corrosion Reviews, Volume: 30 (3-4), Pages: 105-123 https://doi.org/10.1515/corrrev-2012-0502

[3] Guo, W., Crowther, D., Francis, J. A., Thompson, A., Liu, Z., Li, L. 2015. Microstructure and mechanical properties of laser welded S960 high strength steel. Materials & Design, Volume 85, 2015, Pages 534-548. ISSN 0264-1275

[4] Chen, Y. S., Huang, C., Liu, P. Y., Yen, H. W., Niu, R., Burr, P., Moore, K. L., Martínez-Pañeda, E., Atrens, A., Cairney, J. M. 2024. Hydrogen trapping and embrittlement in metals– a review. International Journal of Hydrogen Energy. Volume: 136, Pages: 789-821 https://doi.org/10.1016/j.ijhydene.2024.04.076

[5] www.ssab.com Strenx 960 MC SSAB [online]. 2023: https://www.ssab.com/cs-cz/znacky-a-vyrobky/strenx/nabidka produktu/960/mc

[6] Schneider, C., Ernst, W., Schnitzer, R., Staufer, H., Vallant, R., Enzinger, N. 2018. Welding of S960MC with undermatching filler material. Welding in the World, 62, 801-809. https://doi.org/10.1007/s40194-018-0570-1

[7] Drexler, A., Bergmann, C., Manke, G., Kokotin, V., Mraczek, K., Pohl, M., Ecker, W. 2021. On the local evaluation of the hydrogen susceptibility of cold formed and heat treated advanced high strength steel (AHSS) sheets. Materials Science and Engineering: A, 800, 140276. https://doi.org/10.1016/j.msea.2020.140276.

[8] Gordiak, M., 2018 Metody vodíkování ocelí pro experimentální účely. Brno: Vysoké učení technické v Brně, Fakulta strojního inženýrství.

HODNOTENIE MECHANICKEJ A KORÓZNEJ ODOLNOSTI HORČÍKOVÝCH ZLIATIN V SIMULOVANOM PROSTREDÍ ĽUDSKÉHO TELA

Melisa Šnircová[1*], Peter Palček[1], Martin Slezák[1], Milan Uhričík[1], Edita Illichmanová[1]
[1] Strojnícka fakulta, Katedra materiálového inžinierstva, Žilinská univerzita v Žiline, Univerzitná 8215/1, 010 26 Žilina, Slovenská republika
** melisa.snircova@fstroj.uniza.sk, +421 41 513 2620, Strojnícka fakulta, Katedra materiálového inžinierstva, Žilinská univerzita v Žiline, Univerzitná 8215/1, 010 26 Žilina, Slovenská republika*

1. Úvod

Horčík je nenahraditeľnou súčasťou prírody a ľudského tela. V prírode sa predovšetkým kvôli svojej reaktivite vyskytuje prevažne vo forme zlúčenín. Je súčasťou kremičitanov, uhličitanov a chloridov, kde má oxidačný stupeň Mg^{2+}. Ďalej je významnou súčasťou morskej vody. Ako prvok je horčík súčasťou štruktúr ľudského tela. Napomáha funkcii enzýmov, správnemu fungovaniu svalov a nervov a zúčastňuje sa mnohých reakcii v organizme. [1]

Pre svoje výnimočné vlastnosti akými sú biokompatibilita, nízka hustota a nízka hmotnosť sa po mnohé roky dostáva do povedomia biomedicínskych inžinierov a výrobcov implantátov ako perspektívny materiál na výrobu vnútro telových biodegradovateľných implantátov. [2]

Horčík má pre využitie v medicíne niekoľko nedostatkov. Horčík je korózne nízko odolný predovšetkým v prostrediach obsahujúcich ióny Cl^-, a preto by jeho korózia v prostredí telesných tekutín bola príliš rýchla. Pri korózii tohto kovu sa ďalej uvoľňuje množstvo plynného vodíka, ktorý by mohol nepriaznivo ovplyvniť okolité prostredie biomateriálu. Vylepšovanie vlastností horčíka a jeho zliatin je predmetom výskumu po mnohé roky. Jednou z metód úpravy vlastností materiálov je legovanie. Legovaním je možné pozmeniť vhodnou voľbou legúr či už mechanické alebo korózne vlastnosti horčíka. Pred voľbou vhodných legúr je potrebné zhodnotiť mechanické a korózne správanie horčíkových zliatin napríklad v simulovanom prostredí ľudského tela. Na hodnotenie mechanického správania zliatin horčíka sú používané skúšky ťahom a skúšky tvrdosti, ktoré so sebou významne korelujú. Jednou z najpoužívanejších je skúška tvrdosti podľa Vickersa. Pri hodnotení koróznej odolnosti materiálov sú používané predovšetkým potenciodynamická polarizácia a elektrochemická impedančná spektroskopia (EIS). Táto technika je obľúbená pre simulovanie správania materiálov v prostredí ľudského tela čiže vodivého prostredia. Vhodnou kombináciou skúšok a meraní je možné získať poznatky a prehľad korózneho správania materiálov ako je horčík. [2] [3]

Výskum sa zameriava na komerčne čistý horčík, ako aj používané zliatiny AZ a AE. Tieto zliatiny horčíka však v súčasnosti nie sú dostatočne diskutované ako možné biomateriály. Cieľom výskumu je zhodnotiť vplyv druhu a množstva legúr na mechanické a korózne správanie v simulovanom prostredí ľudského tela a na záver určiť najvhodnejšiu zliatinu pre biomedicínske aplikácie. Objavenie vhodnej kombinácie horčíka a legúr iných kovov by mal výrazný vplyv na používanie tohto kovu v biomedicíne a na prípadné nahradenie niektorých menej vhodných materiálov na výrobu implantátov, stentov, skrutiek a podobne.

2. Kovové materiály v biomedicínskom inžinierstve

Kovové materiály sa v biomedicínskych aplikáciách používajú predovšetkým na fixáciu zlomenín či náhrade kĺbov. Prostredie ľudského tela je pomerne agresívne, a preto majú kovové implantáty náchylnosť ku korózii. Jedným z aktuálne a najčastejšie používaných kovov na implantáty je titán, ktorý ale nie je ideálnym materiálom z niekoľkých dôvodov. Výroba a spracovanie titánu je finančne nákladné, pretože sa prirodzene nenachádza v čistom stave. Ďalšou nevýhodou titánových materiálov je prílišná odlišnosť vlastností medzi titánom a ľudskou kosťou. Titánové zliatiny majú modul pružnosti približne 110 GPa, pričom ľudská kosť má modul pružnosti okolo 5-20 GPa. Tento markantný rozdiel v moduloch pružnosti vytvára následné vysoké namáhanie na spojení/rozhraní kosť-implantát. Titán má však nateraz viac výhod ako nevýhod. Na implantáty sa používa pre jeho vysokú odolnosť voči korózii. Je to pevný, biokompatibilný a ľahký materiál. Skôr ako samotný čistý titán sa používajú jeho zliatiny. Titánové zliatiny sa dokonca vyznačujú lepšími fyzikálnymi, chemickými a koróznymi vlastnosťami. Stredom záujmu biomedicínskych inžinierov sa postupne stáva horčík. Horčík má výhodné mechanické vlastnosti, narozdiel od titánu je biologicky odbúrateľný. V tele horčík reaguje s vodou a degraduje vďaka čomu sa stráca potreba sekundárnych operácii za účelom odstránenia implantátov. Degradáciou horčíka vznikajú katióny Mg^{2+}, ktoré sú potrebné pre správne fungovanie metabolických procesov, katalyzujú stovky druhov enzýmov a podporujú rast kostí. Problémom použitia horčíka stále zostáva jeho rýchla degradácia a prudké korózne správanie. [1] [2]

Tvrdosť materiálov meriame v praxi najmä vnikajúcimi skúškami. Podstatou skúšok tvrdosti je posudzovanie tvrdosti daného materiálu podľa odporu voči deformácii povrchu. Deformáciu vyvoláme mechanickým účinkom tvrdšieho telesa s predpísanými rozmermi. Menej v praxi používanými sú odrazové metódy, ktoré môžeme zahrnúť medzi dynamické skúšky. Tvrdosť materiálu nemožno považovať za fyzikálnu veličinu, pretože sa jedná o porovnávacie merania. Do vzťahov pre vyhodnocovanie výsledkov merania dosádzame veličiny – silu [N] a plochu $[mm^2]$. Medzi najpoužívanejšie metódy patria skúšky podľa Brinella (STN EN ISO 6506-1), Vickersa (STN EN ISO 6507-1), Knoopa (ISO 4545-1) a Rockwella (STN EN ISO 6508-1). [4] [5]

2.1. Skúšky tvrdosti podľa Brinella, Vickersa a Knoopa

Pri týchto skúškach sa do povrchu skúšaného materiálu vtláčajú telesá (indentory) konštantným zaťažením F, tým vznikne vtlačok s plochou povrchu S. Tvrdosť potom určíme ako pomer F/S a označuje sa HBW (Brinell), HV (Vickers) alebo HK (Knoop). Vzorky materiálu, ktoré sa prebrúsia uložíme na hladké, čisté a nepoddajné podložky. Zaťaženie F musí pôsobiť kolmo na povrch. Minimálne hrúbky vzoriek pri skúškach tvrdosti sú presne definované normami pre jednotlivé meracie metódy a príslušné zaťaženia. Skúšky sa navzájom líšia tvarom indentora (štvorboký ihlan, guľôčka z tvrdokovu a podobne).

Pri Vickersovej skúške tvrdosti môžeme voliť hodnoty zaťaženia F=1,961 (0,2); 2,942 (0,3); 4,903 (0,5); 980,7(100); 294,2 (30) N; atď. Vickersovu tvrdosť potom označujeme

HV 0,2; HV 0,3; HV 0,5; HV 30, HV 100. Označenie HV sa uvádza za hodnotu tvrdosti a je doplnené indexom, ktorý charakterizuje podmienky skúšky v nasledujúcom poradí: veľkosť skúšobného zaťaženia (kp), čas pôsobenia zaťaženia (s). [4]
Pri skúškach bolo použitých päť vzoriek materiálov, konkrétne technicky čistý horčík Mg 99,9 a zliatiny AZ31, AZ63, AZ91, AE21. Normalizované chemické zloženie zliatin je v Tabuľke 1.

***Tab. 1** Chemické zloženie zliatin horčíka podľa ASTM [6]*

	Obsah prvku [v hm. %]			
Názov zliatiny	*Al*	*Zn*	*KVZ*	*Mn*
AZ31	*3*	*1*	-	*0.3*
AZ63	*6*	*3*	-	*0.3*
AZ91	*9*	*1*	-	*0.3*
AE21	*2*	-	*1*	*0.3*

Na vzorkách bola vykonaná statická skúška tvrdosti podľa Vickersa. Pred samotnými skúškami tvrdosti sme museli každú z piatich vzoriek prebrúsiť na brúsnom papieri zrnistosti p4000, ďalej vyčistiť izopropanolom a vysušiť prúdom vzduchu. Táto príprava vzorky pred meraním slúži na to, aby sa odstránili z povrchu materiálu nežiadúce oxidy a korózne produkty, a taktiež aby nerovnosti na povrchu vzorky neovplyvňovali meranie. Tvrdomer na ktorom sme meranie vykonali bol INNOVATEST FALCON 450. Tvar indentora bol štvorboký ihlan s vrcholovým uhlom 136°. Vzorky sme v danom poradí vkladali na podložku tvrdomera, navolili sme veľkosť skúšobného zaťaženia a čas pôsobenia zaťaženia (30 s). Po spustení zariadenia sa začne indentor približovať k povrchu až sa ho dotkne a následne postupne dosiahne úplné zaťaženia. Po 30 sekundách úplného zaťaženia sa indentor odstráni a pomocou mikroskopickej optiky sa odmerajú uhlopriečky vtlačku, z ktorých systém automaticky vypočíta tvrdosť vo Vickersoch.

2.2 Potenciodynamická polarizácia

Rozsah skúšky bol od -200 mV do +300 mV voči koróznemu potenciálu. Rýchlosť zmeny potenciálu bola 1 mV za sekundu. Výsledné potenciodynamické krivky boli analyzované Tafelovou analýzou zobrazenou na Obr. 1, čím boli zistené hodnoty korózneho potenciálu E_{kor}, koróznej prúdovej hustoty i_{kor}, koeficientov β_A a β_C a vypočítaná bola korózna rýchlosť r_{kor} (v_{kor}).

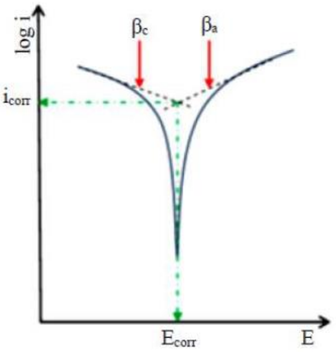

Obr. 1 *Tafelova analýza potenciodynamickej krivky [7]*

3. Výsledky a diskusia

Z nameraných hodnôt tvrdosti materiálov (Tab. 2) a ich priemerov vidno, že najvyššiu hodnotu tvrdosti mala zliatina AZ91, naopak najnižšia tvrdosť bola zistená na vzorke komerčne čistého horčíka Mg 99,9. Pomerne vysokú tvrdosť dosiahla aj zliatina AE21.

Tab. 2 *Namerané hodnoty tvrdosti*

Názov materiálu	*Veľkosť skúšobného zaťaženia/ čas pôsobenia zaťaženia [kp/s]*	*Nameraná hodnoty tvrdosti*	*Priemer hodnôt*
Mg 99.9	*5/30*	*22,9 HV*	*23,8 HV*
		26,7 HV	
		21,8 HV	
AZ31	*5/30*	*42,7 HV*	*43,7 HV*
		43,6 HV	
		44,7 HV	
AZ63	*5/30*	*52,9 HV*	*56,4 HV*
		59,9 HV	
		56,4 HV	
AZ91	*5/30*	*59,01 HV*	*61,1 HV*
		61,5 HV	
		62,8 HV	
AE21	*5/30*	*56,9 HV*	*57,06 HV*
		57,3 HV	
		56,98 HV	

Zo získaných výsledkov (Tab. 3) vyplýva, že najkladnejší korózny potenciál (E_{kor}) mala vzorka AZ63. Korózny potenciál charakterizuje termodynamiku korózie a s kladnejšími hodnotami stúpa ušľachtilosť kovu. Najnižšia hodnota prúdovej hustoty korózie bola zaznamenaná pri zliatine AZ91. Prúdová hustota korózie charakterizuje kinetiku korózie. Ďalej sa pri hodnotení odolnosti materiálu zameriavame na rýchlosť korózie (r_{kor}). Najnižšiu rýchlosť korózie sme zaznamenali pri vzorke AZ91. Pri hodnotení celkovej koróznej odolnosti metódou potenciodynamickej polarizácie je nutné prihliadať na všetky vyššie uvedené veličiny. Potom môžeme určiť, že korózne najodolnejším materiálom bola vzorka AZ91. Najhoršie pri potenciodynamických skúškach obstála AE21. Pre názornosť je uvedené aj grafické znázornenie nameraných výsledkov na Obr. 2.

***Tab. 3** Namerané výsledky potenciodynamickej polarizácie*

Názov materiálu	E_{kor} [mV]	i_{kor} [mA/ cm^2]	β_A [mV]	β_C [mV]	r_{kor} [mm/ rok]
Mg 99.9	*-1744*	*12,924*	*142*	*206*	*0,295*
AZ31	*-1584*	*9,034*	*64*	*139*	*0,206*
AZ63	*-1496*	*7,6*	*46*	*174*	*0,17*
AE21	*-1533*	*20,550*	*72*	*139*	*0,407*
AZ91	*-1520*	*7,041*	*52*	*188*	*0,161*

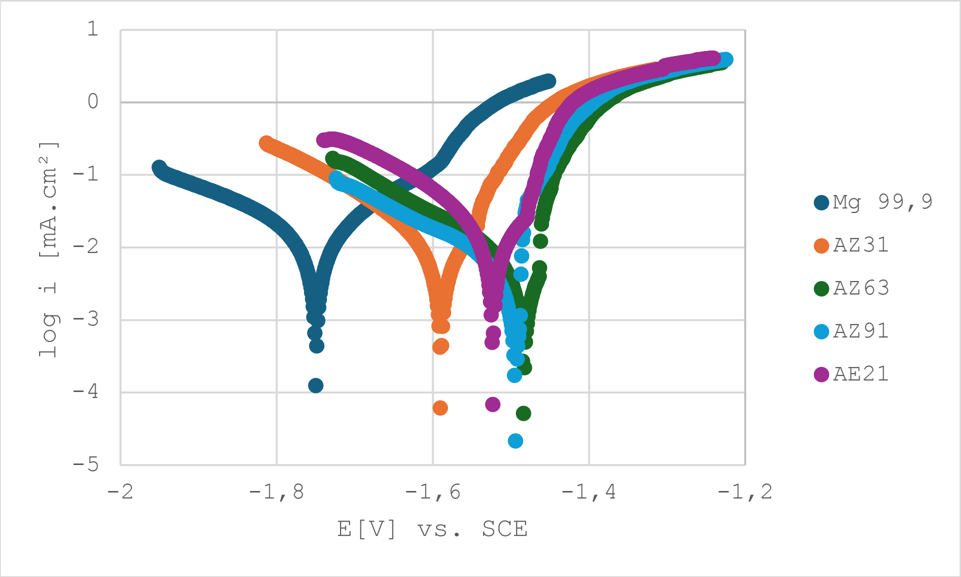

***Obr. 2** Potenciodynamické krivky vzoriek horčíkových materiálov*

Teoretická časť článku bola zameraná na zhrnutie doterajších poznatkov o horčíku, jeho zliatinách a spôsoboch hodnotenia mechanickej a koróznej odolnosti horčíka. Experimentálna časť bola potom zameraná na určenie najvhodnejších legúr horčíka pre biomedicínske aplikácie. Na posúdenie koróznej odolnosti vzoriek bola použitá potenciodynamická polarizácia. Na základe získaných výsledkov meraní a ich analýz boli stanovené nasledovné závery:

- Legúra hliníka v zliatine AZ91 napomáha dosiahnutiu vyššej pevnosti zliatiny.
- Zliatina AZ 91 mala zo všetkých vzoriek najvyššiu tvrdosť (61,1 HV).
- Zliatina AZ91 by po podrobnejšom štúdiu, z hľadiska biokompatibility v dôsledku vyššieho obsahu hliníka mohla slúžiť na biomedicínske aplikácie.
- Prímesy KVZ (prvky vzácnych zemín) znižujú tvrdosť zliatin horčíka.
- Komerčne čistý horčík Mg 99,9 nie je vhodný pre svoju nízku tvrdosť na biomedicínske účely.
- Korózny potenciál (E_{cor}) zliatiny AZ91 je pozitívnejší (-1520 mV) ako korózny potenciál zliatiny AE21 (-1533 mV), z čoho vyplýva, že AZ91 je výrazne korózne odolnejšia ako AE21.
- Zliatina AZ 91 vykazovala zo všetkých vzoriek najvyššiu koróznu odolnosť.

Globálnym záverom tejto práce je, že najvhodnejšími legúrami horčíka pre biomedicínske aplikácie z hľadiska zvyšovania pevnosti a koróznej odolnosti sú hliník a zinok. V zliatine AZ91 boli dosiahnuté vo všetkých experimentoch optimálne výsledky pre biomedicínu z mechanického a korózneho hľadiska. Zliatina AE21 dosiahla najhoršie výsledky v oboch experimentoch.

Poďakovanie

Výskum bol podporený Ministerstvom školstva, výskumu, vývoja a mládeže Slovenskej republiky prostredníctvom projektov VEGA č. 1/0461/24, VEGA 1/0729/26 a KEGA č. 033ŽU-4/2026.

Literatúra

[1]Fatima, G., Dzupina, A., Alhmadi, H. B., Magomedova, A., Siddiqui, Z., Mehdi, A., RAZA, A. M.: Magnesium matters: A comprehensive review of its vital role in health and diseases. Cureus, Vol. 16, No. 10, 2024.
[2] Palček, P., Markovičová, L., Zatkalíková, V.: Materiály pre biomedicínske inžinierstvo. EDIS- vydavateľské centrum ŽU, Žilina, ISBN 978-80-554-0988-7, 2015.
[3] Davis, J.R.: Alloying: understanding the basics. ASM International, Ohio-USA, ISBN 978-0-87170-744-4, 2001.
[4] Skočovský, P., Bokůvka, O., Konečná, R., Tillová, E.: Náuka o materiáli pre odbory strojnícke. EDIS- vydavateľské centrum ŽU, Žilina, 2013.
[5]Veles, P.: Mechanické vlastnosti a skúšanie kovov. ALFA, Bratislava, 1985.
[6] Kajánek, D., Hadzima, B., Brezina, M., Jacková, M.: Effect of Applied Current Density of Plasma Electrolytic Oxidation Process on Corrosion Resistance of AZ31 Magnesium Alloy. Communications — Scientific Letters of the University of Žilina, Vol. 21, pp 32–36, 2019.
[7]Nazari, M. H., Zhang, Y., Mahmoodi, A., Xu, G., Yu, J., Wu, J., & Shi, X.: Nanocomposite organic coatings for corrosion protection of metals: A review of recent advances. Progress in Organic Coatings, 2022.

29th International Seminar of Ph.D. Students

SEMDOK 2026

Western Tatras – Zuberec, Slovak Republic
February, 4 to February 6, 2026

THE DESIGN OF A NOVEL TEST SPECIMEN GEOMETRY FOR ADDITIVELY MANUFACTURED MATERIALS

Peter Špuro[1*], Andrej Czán[1], Mario Drbúl[1], Marek Roszak[2], Oktawian Bialas[2], Jozef Bronček[1]
[1] Department of Machining and Manufacturing Technology, Faculty of Mechanical Engineering, University of Zilina, Univerzitná 1, 010 26 Žilina, Slovakia
[2] Department of Engineering Materials and Biomaterials, Faculty of Mechnical Engineering, Silesian University of Technology, ul. Konarskiego 18A, 44-100 Gliwice, Poland
**Corresponding author: peter.spuro@fstroj.uniza.sk*

1. Introduction

Metal additive manufacturing (MAM) enables the direct fabrication of metallic components from digital models through layer-by-layer material deposition [1]. The main techniques include selective laser melting (SLM), Binder Jetting (BJ), and Atomic Diffusion Additive Manufacturing (ADAM), which differ in material deposition mechanisms, thermal gradients, and post-processing, affecting microstructure, mechanical properties, and residual stress formation [2]. ADAM, developed by Markforged, is a Material Extrusion (MEX)-based technique that combines filament extrusion with subsequent metallurgical sintering [3]. A composite filament containing metal particles in a polymer binder forms a “green part,” which is transformed into a fully metallic component after debinding and sintering [4]. Compared to SLM and BJ, ADAM generally produces lower residual stresses, improving dimensional stability and the mechanical response of the parts [5,6]. Tensile testing is a fundamental method for evaluating the mechanical properties of metallic materials [7]. Standard dog-bone specimens are most commonly used [8,9], but conventional shapes often fail outside the gauge section, rendering the results invalid [7,8]. For harder materials, specimen slippage in grips may also occur, distorting the results [10]. For these reasons, a specific specimen geometry was designed to ensure secure clamping, localized fracture within the gauge section, and minimal stress concentration in the heads, improving the accuracy and comparability of tensile test results. The objective of this study is to evaluate the suitability of the proposed specimen geometry for tensile testing of metallic materials, focusing on controlled failure within the functional section, minimizing stress concentration in the heads, and ensuring accurate measurement of mechanical properties.

1.1 Materials and Methods

For the printing process, 17-4 PH stainless steel was chosen. This precipitation-hardening alloy is recognized for its high strength and outstanding corrosion resistance. It is particularly suitable for applications that demand a balance of mechanical performance, durability, and resistance to environmental factors. The chemical composition of the alloy is shown in Table 1.

Tab. 1 *Chemical composition of Markforged 17-4 PH stainless steel*

Elements	***C***	***Cr***	***Ni***	***Mo***	***Si***	***Mn***	***N***	***Cu***	***S***
[wt. %]	*0,06*	*16.50*	*4.03*	*0.01*	*0.36*	*0.15*	*0.52*	*3.77*	*0.05*

For the tensile tests, specimens with machined heads (Fig. 1) were used, chosen to prevent slippage of the sample in the grips of the testing machine. Conventional dog-bone specimens tended to slip in the clamping system during testing, which was caused by the high hardness of the material and the resulting low friction between the specimen surface and the grips. The use of machined heads allowed a more uniform distribution of clamping pressure, providing a more stable fixation of the specimen during the test.

As a result, failure occurred within the functional (gauge) section, ensuring the correct localisation of the fracture and the validity of the measured results. In dog-bone specimens, it was frequently observed that failure did not occur in the functional section but rather in the clamped area, or the specimen underwent only plastic elongation without complete rupture. Such tests had to be subsequently classified as invalid because they did not meet the requirements for determining tensile properties.

To optimize the additive manufacturing process, reduce material usage, and shorten printing time, the dimensions of the tensile test specimens were modified. The functional length of the specimen was reduced to 20 mm. This modification was justified since significant elongation and necking are not expected for these tool steels after heat treatment. The gauge section diameter was set to 6 mm, ensuring a sufficient cross-section to obtain representative mechanical properties.

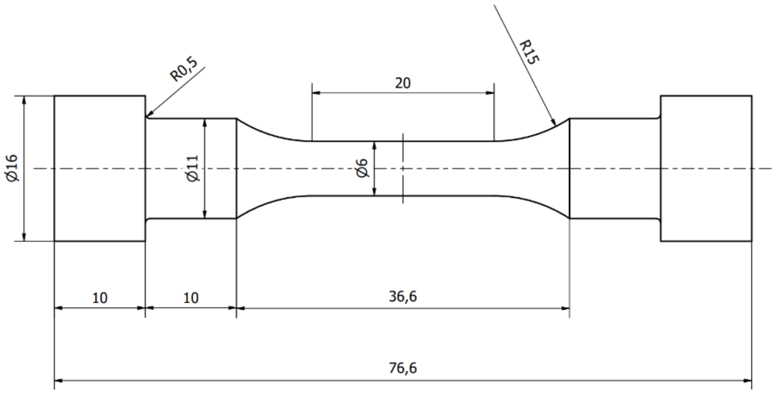

Fig. 4 *Schematic representation of the specimen*

The specimen was fabricated in a horizontal (lying) orientation to minimize support entrapment and ensure the quality of the final component (Fig. 2).

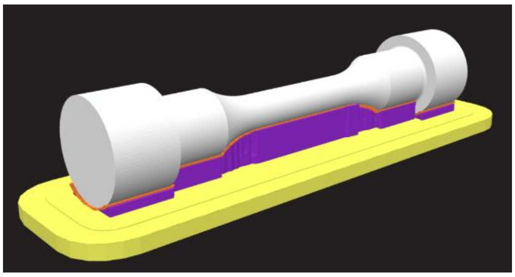

Fig. 5 *Horizontal orientation of the specimen*

The specimens were fabricated with a layer height of 0.127 mm, a solid infill, and four perimeters. The total fabrication time for the green part was approximately five hours.The specimen was oriented to enable optimal printing and included support structures to ensure stability throughout the process. A ceramic release layer was applied between the layers, facilitating easier separation after sintering. Process simulation and layer visualization in the slicer provided an overview of the part's structure, orientation, and the expected fabrication sequence, which is important for ensuring the quality and accuracy of the specimen intended for the tensile test.

Tensile tests were conducted according to ASTM E8/E8M for metallic materials on specimens with machined heads, which were slightly modified to ensure secure clamping and prevent slippage during testing (Fig. 3). The tests were performed on an INSTRON universal testing machine, using grips designed for specimens with machined heads.

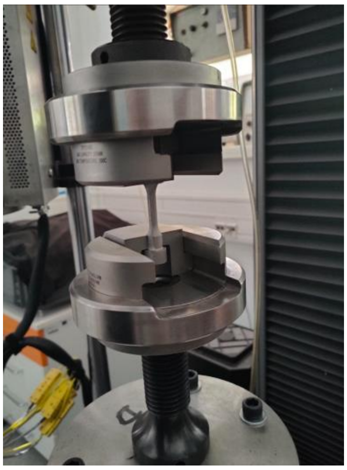

Fig. 6 *Clamping of tensile specimen*

2. Results and discussion

During the tensile tests, fracture occurred exclusively within the functional (gauge) section, confirming that the proposed specimen geometry ensured proper localization of failure (fig.4). No slippage of the specimens in the gripping system or premature failure in the clamped regions was observed, demonstrating the effectiveness of the machined heads in providing stable and reliable fixation during loading.

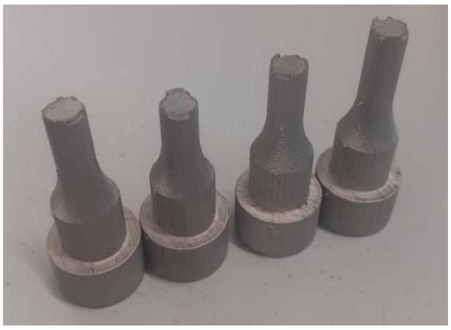

***Fig. 4** Specimens after tensile testing*

Based on the average measured values, a maximum load of approximately 33 kN was achieved, and the average ultimate tensile strength Rm reached approximately 1190 MPa, while the measured elongation was approximately 2.9% (Tab. 2). These results confirm that the study's objective to achieve controlled fracture within the functional section and obtain valid tensile test results was successfully achieved

***Tab. 2** Mechanical properties of 17-4 PH*

Max. load [kN]	Tensile strength Rm [MPa]	Rp1 [MPa]	Load at Rp1 [kN]	Rp0.2 [MPa]	Load at Rp0.2 [kN]	Elongation [%]
33	1190	1108	31	835	23	2.9

During the tensile tests, fracture occurred exclusively within the functional (gauge) section, confirming that the proposed specimen geometry ensured proper localization of failure. No specimen slippage or premature failure in the clamped regions was observed, demonstrating the effectiveness of the machined heads [11, 12].

On average, the maximum load was approximately 33.7 kN, the ultimate tensile strength (Rm) reached about 1190 MPa, and the elongation of the specimens was around 2.9%, consistent with reported data for additively manufactured metallic parts [11, 13, 14].

Comparison with the literature indicates that machined heads and optimized specimen geometry significantly reduce the risk of failure outside the gauge section. Park et al. [11] and Shanbhag et al. [12] highlighted the importance of specimen geometry and orientation in tensile testing of AM components, while Li Han et al. [15] demonstrated that necking location and fracture depend on dog-bone specimen geometry. Alkindi et al. [16] emphasized the effect of printing angle on the tensile strength of 17-4 PH stainless steel, illustrating the influence of layer orientation.

The 17-4 PH material produced via ADAM exhibits mechanical properties comparable to those reported by Galati and Minetola [13] and Henry et al. [14]. The lower residual stresses typical of ADAM contribute to stable fracture localization and predictable mechanical response of the parts.

In conclusion, the designed specimen geometry, including machined heads and optimized gauge length, is suitable for tensile testing of harder metallic materials produced by ADAM, and the results comply with the ASTM E8/E8M standard [12].

Conclusion

This study confirmed that the proposed tensile specimen geometry with machined heads is suitable for mechanical testing of metallic materials produced by Atomic Diffusion Additive Manufacturing (ADAM). The modified design ensured secure clamping, eliminated specimen slippage, and consistently localized fracture within the gauge section, thereby fulfilling the requirements of ASTM E8/E8M.

The measured mechanical properties of 17-4 PH stainless steel were in good agreement with literature data, demonstrating that the optimized geometry enables reliable and valid tensile test results. Overall, the results indicate that the proposed specimen design improves test repeatability and accuracy for harder additively manufactured metallic materials.

Acknowledgment

This research was funded by the University of Zilina project VEGA 1/0722/25 Research on additive technologies with a focus on their application in the design and construction of cutting tools, 09I05-03-V02-00080 DigiDent (Research on the Digitalization of Dental Implant Components for the Creation of Personalized 3D Models for the Manufacturing Process), KEGA 028ŽU-4/2024: “Implementation of innovative approaches in the education of students in the field of 3D metrology, APVV-20-0561 Research into the implementation of new measuring methods for the calibration of measuring systems for industrial metrological practice, APVV-20-0216 Research on the Implementation of High-Impact Surface Technologies for Precision Automotive Structural Components and by the grant scheme UNIZA 21068: “Research on the Mechanical Properties of Materials in Additive Manufacturing”.

References

[1] Zhang, Y.; Wu, L.; Guo, X. et al., Additive Manufacturing of Metallic Materials: A Review, J. Mater. Eng. Perform., 2018, 27, 1–13.

[2] Bikas, H.; Stavropoulos, P.; Chryssolouris, G., Additive manufacturing methods and modelling approaches: a critical review, Int. J. Adv. Manuf. Technol., 2016, 83, 389–405.

[3] Badiru, A.B.; Valencia, V.V.; Liu, D. (Eds.), Additive Manufacturing Handbook: Product Development for the Defense Industry, CRC Press, 2017.

[4] Jamróz, W.; Szafraniec, J.; Kurek, M. et al., 3D Printing in Pharmaceutical and Medical Applications – Recent Achievements and Challenges, Pharm. Res., 2018, 35, 176.

[5] Kok, Y.; Tan, X.P.; Wang, P.; Nai, M.L.S.; Loh, N.H.; Liu, E.; Tor, S.B., Anisotropy and heterogeneity of microstructure and mechanical properties in metal additive manufacturing: A critical review, Mater. Des., 2018, 139, 565–586.

[6] Galati, M.; Minetola, P., Analysis of Density, Roughness, and Accuracy of the Atomic Diffusion Additive Manufacturing (ADAM) Process for Metal Parts, Materials, 2019, 12, 4122.

[7] Seong Je Park, Ji Eun Lee, Sun Chul Jin et al., Tensile test of additively manufactured specimens with external notch removed via laser cutting in material extrusion, Polymer Testing, 2022, 110, 107581. https://doi.org/10.1016/j.polymertesting.2022.107581

[8] Balduzzi, G.; Zelaya-Lainez, L.; Hochreiner, G.; Hellmich, C., Dog-bone Samples may not Provide Direct Access to the Longitudinal Tensile Strength of Clear-wood, The Open Civil Engineering Journal, 2021, 15, 1–12.

[9] Callister, W.D.; Rethwisch, D.G., Materials Science and Engineering: An Introduction, 10th Edition, Wiley, 2018.

[10] ASTM International, ASTM E8 / E8M – Standard Test Methods for Tension Testing of Metallic Materials, West Conshohocken, PA: ASTM International, 2023. [Online]. Dostupné: https://www.astm.org/e0008_e0008m-23.html

[11] Seong Je Park, Ji Eun Lee, Sun Chul Jin et al., Tensile test of additively manufactured specimens with external notch removed via laser cutting in material extrusion, Polymer Testing, 2022, 110, 107581. https://doi.org/10.1016/j.polymertesting.2022.107581

[12] Admet, Tensile Grip Buying Guide and Common Errors in Tensile Testing, Admet, 2014.

[13] Galati, M.; Minetola, P., Analysis of Density, Roughness, and Accuracy of the Atomic Diffusion Additive Manufacturing (ADAM) Process for Metal Parts, Materials, 2019, 12, 4122.

[14] Henry, T.C.; Morales, M.A.; Cole, D.P. et al., Mechanical behavior of 17-4 PH stainless steel processed by atomic diffusion additive manufacturing, Int. J. Adv. Manuf. Technol., 2021, 114, 2103–2114.

[15] Li Han, N. Reynolds, I. Dargue, G. Williams, The Effect of Specimen Dimensions on Obtained Tensile Properties of Sheet Metals, Key Engineering Materials, 2009.

[16] Alkindi, T., Alyammahi, M., Susantyoko, R.A. et al., The effect of varying specimens' printing angles to the bed surface on the tensile strength of 3D-printed 17-4PH stainless-steels via metal FFF additive manufacturing, MRS Communications, 2021, 11, 310–316. https://doi.org/10.1557/s43579-021-00040-0

[17] J. Dzugan, E. Lucon, M. Koukolikova, Y. Li, S. Rzepa, M.S. Yasin, S. Shao, N. Shamsaei, M. Seifi, M. Lodeiro, F. Lefebvre, U. Mayer, J. Olbricht, M. Houska, V. Mentl, Z. You, ASTM interlaboratory study on tensile testing of AM deposited and wrought steel using miniature specimens, Theoretical and Applied Fracture Mechanics, 2024, 131, 104410. https://doi.org/10.1016/j.tafmec.2024.104410

[18] He, P., Du, W., Wang, L., Kiran, R., & Yang, M., Additive Manufacturing and Mechanical Performance of Trifurcated Steel Joints for Architecturally Exposed Steel Structures, Materials, 2020, 13(8), 1901. https://doi.org/10.3390/ma13081901

[19] Banerjee, S.; Joens, C.J., Debinding and sintering of metal injection molding (MIM) components, In Handbook of Metal Injection Molding; Heaney, D.F., Ed.; Woodhead Publishing, 2012; pp. 133–180.

29th International Seminar of Ph.D. Students

SEMDOK 2026

Western Tatras – Zuberec, Slovak Republic
February, 4 to February 6, 2026

Experimental Evaluation of Hybrid Composite Beams

Akshat Tegginamath[1*], **Michal Petru**[1]
[1] Department of Design of Machine Elements & Mechanism, Faculty of Mechanical Engineering, Technical University of Liberec, Liberec, Czech Republic
**Corresponding author: akshattm93@gmail.com, +420 792484909, Koleje TUL Harcov, Liberec 4601, CZ*

1. Introduction

Traditional automotive structural components are typically manufactured from steel or cast iron, which provide adequate protection but significantly increase vehicle weight, thereby reducing efficiency. To address environmental concerns and improve fuel economy, the automotive industry is increasingly adopting lightweight materials. Replacing conventional structural components with composite materials enables substantial weight reduction while maintaining comparable mechanical performance, leading to improved vehicle efficiency.

Ojeda et al. [1] experimentally evaluated the crashworthiness of composite automotive components and validated their performance through numerical simulations. Glass fiber– and carbon fiber–reinforced composites were investigated, demonstrating significant weight reduction while maintaining acceptable stiffness and strength. The study concluded that composite materials are viable alternatives for automotive structural applications, with finite element modeling proving effective for early-stage validation.

Hesse et al. [2] focused on optimizing carbon fiber–reinforced polymer (CFRP) structures for crashworthiness, particularly for battery electric vehicles, which suffer from increased mass due to battery systems. Their work established a systematic optimization workflow, showing that CFRP composites, despite design complexity, offer high specific energy absorption and enable lighter and safer vehicle structures.

Composite materials consist of a matrix and reinforcement, combining multiple constituents to enhance overall performance [3–6]. Their use in automotive structures has grown due to their favourable strength-to-weight ratios. Further environmental benefits can be achieved through hybrid composites incorporating natural fibers alongside synthetic reinforcements.

Natural fiber composites (NFCs) have gained increasing attention due to their low cost, renewability, biodegradability, and reduced manufacturing impact [9–11]. Common natural fibers include hemp, flax, jute, and cotton, combined with thermoplastic or thermoset matrices [9,12]. Although the concept of natural fiber reinforcement dates back thousands of years, modern NFCs offer a sustainable alternative for lightweight structural applications.

This study focuses on hybrid composite structural beams intended for automotive bumper applications, aiming to achieve weight reduction while maintaining mechanical performance.

2. Materials

The hybrid composites consisted of layers of flax fabrics and glass fabrics (S-glass) stacked in various sequences. The composite samples produced consisted of 8 layers of fabrics each and the list of samples that were tested are: sample 1: G (8 layers fabrics); sample 2: F (8 layers fabrics); sample 3: G 4 (7 layers of flax fabrics and 1 layer of glass fabrics); sample 4: G 2,7 (6 layers of flax fabrics and 2 layers of glass fabrics); sample 5: G 3,4,5,6 (4 layers of flax fabrics and 4 layers of glass fabrics); sample 6: K (8 layers of Kevlar fabric); sample 7: C (8 layers of carbon fabric). Shape and dimensions of samples are shown in **Fig. 1**.

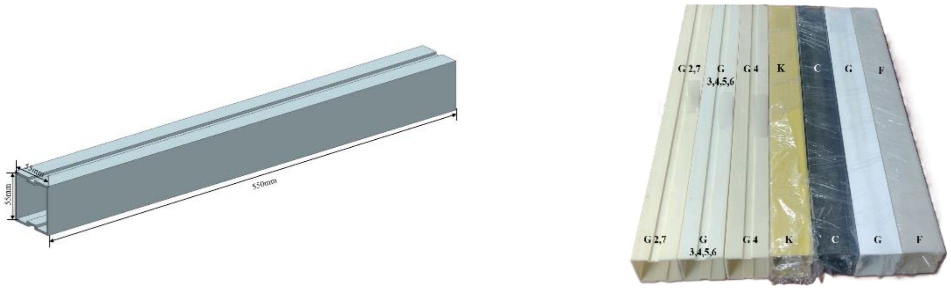

c) CAD model *d) marked of samples*

Fig. 1 Beams used for testing

3. Experiment

The beams that were prepared were subjected to dynamic loading tests. The composite beams were subjected to dynamic loading and the setup used during the tests is given below in **Fig. 2**.

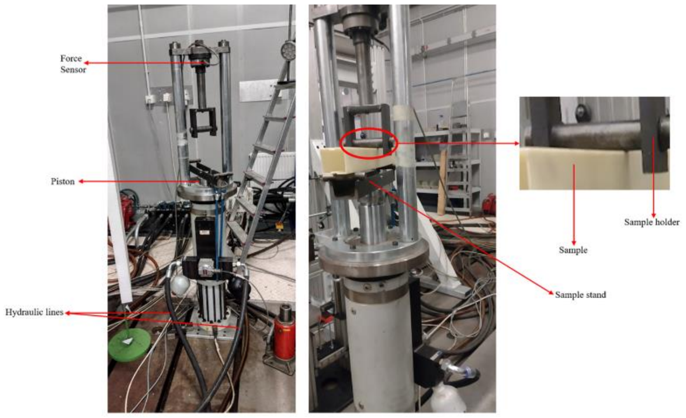

Fig. 2 Setup for dynamic loading, (left) without the sample, (right) with the sample, force 4 kN, frequency 5 Hz, amplitude 4 kN

4. Results

The time required to break each sample measured and tabulated for the samples which were subjected to dynamic loading. The testing of the beam samples were conducted according to the conditions that were set using the Inova testing software. From the time taken for the samples to break, the number of cycles taken to break was calculated. The results of the tests for all samples are presented in **Tab. 1**. A representative sample selected from all the samples after dynamic testing is shown in **Fig. 3**.

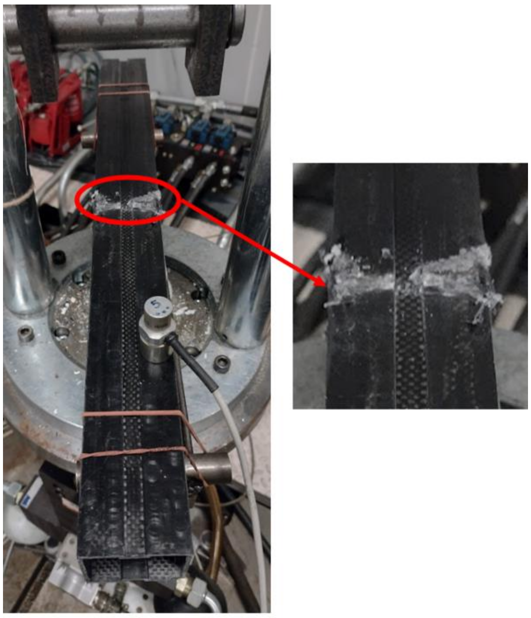

Fig. 3 Illustrative example of a selected sample after dynamic testing, (left) overall view, (right) detail of the failure

Tab. 1 *Results of the number of cycles required for failure of the composite beams*

Samples	***Number of layers***	***Times (minutes) taken to break***	***Number of cycles to break***
F	8	0.67	201
G	8	40.26	12.078
G4	8	3.263	979
G 2.7	8	20.19	6.057
G 3, 4, 5, 6	8	31.43	9.430
K	8	1.33	400
C	8	260.66	78.199

5. Conclusions

Dynamic loading of the composite beams showed that with the increase in the number of layer so of the glass fabric, the number of cycles taken for the composite beams to break increase. It could also be seen that the number of cycles taken for the composite sample with eight layers of glass fabric to break when compared to the number of cycles for the composite beam with four layers of glass fabric to break only increase by 28.1% and on the other hand when there was an increase of 387.06% when the number of cycles taken for the composite beam with only one layer of glass fabric was compared with the composite beam with eight layers of fax fabric. Among the pure composite beams, the beam made from carbon fiber fabrics performed exceedingly well.

References

[1]Ojeda, R. C.: Experimental Evaluation and Predictive Modeling of Composite Materials Crashworthiness. Thesis, 2024.

[2] Hesse, S. H., Duddeck, F.: Optimization of Automotive Composite Structures for Crashworthiness. Thesis, 2021.

[3] Karthi, N., Kumaresan, K., Sathish, S., Gokulkumar, S., Prabhu, L., Vigneshkumar, N.: An overview: Natural fiber reinforced hybrid composites, chemical treatments and application areas. Materials Today: Proceedings, Vol. 27, pp. 2828–2834, 2020.

[4] Suriani, M. J., Ilyas, R., A., Zuhri, M. Y. M., et al.: Critical review of natural fiber reinforced hybrid composites: Processing, properties, applications and cost. Polymers, Vol. 13, No. 20, p. 3514, 2021.

[5] Haris, N. I., Ilyas, R. A., Hassan, M. Z., Saupuan, S. M., Afdzaluddin, A., Jamaludin, K. R., Zaki, S. A., Ramlie, F.: Dynamic mechanical properties and thermal properties of longitudinal basalt/woven glass fiber reinforced unsaturated polyester hybrid composites. Polymers, Vol. 13, No. 19, p. 3343, 2021.

[6] Sapuan, S. M., Aulia, H. S., Ilyas, R. A., Atiqah, A., Dele-Afolabi, T. T., Nurazzi, M. N., Supian, A. B. M., Atikah, M. S. N.: Mechanical properties of longitudinal basalt/woven-glass-fiber-reinforced unsaturated polyester-resin hybrid composites. Polymers, Vol. 12, No. 10, p. 2211, 2020.

[7] Shurtleff, W., Aoyagi, A.: Henry Ford and his researchers: History of their work with soybeans. Soyfoods and Chemurgy (1928–2011): Extensively annotated bibliography and sourcebook. Lafayette, CA: Soyinfo Center, 2011.

[8] Bledzki, A. K., Sperber, V. E., Faruk, O.: Natural and wood fibre reinforcement in polymers. Shawbury, Shrewsbury, Shropshire, U.K.: Rapra Technology Ltd., 2002.

[9] More, A. P.: Flax fiber–based polymer composites: A Review. Advanced Composites and Hybrid Materials, Vol. 5, No. 1, pp. 1–20, 2021.

[10] Ramesh, M., Nijanthan, S., Palanikumar, K.: Processing and mechanical property evaluation of kenaf-glass fiber reinforced polymer composites. Applied Mechanics and Materials, Vols. 766–767, pp. 187–192, 2015.

[11] Rezghi Maleki, H., Hamedi, M., Kubouchi, M., Arao, Y.: Experimental investigation on drilling of natural flax fiber-reinforced composites. Materials and Manufacturing Processes, Vol. 34, No. 3, pp. 283–292, 2018.

[12] Scaffaro, R., Maio, A., Gulino, E. F., Megna, B.: Structure-property relationship of PLA–Opuntia Ficus indica biocomposites. Composites Part B: Engineering, Vol. 167, pp. 199–206, 2019.

UNIVERSITY OF ŽILINA
Faculty of Mechanical Engineering
Department of Materials Engineering

kmi@fstroj.uniza.sk
http://kmi2.uniza.sk
phone: +0421/ 41 513 2600
Univerzitná 8215/ 1, 010 26 Žilina, Slovak Republic

The Department of Materials Engineering provides accredited study programs for a bachelor's degree (Bc) in "Mechanical Technologies," a master's degree (Ing) in "Technical Materials," and a doctoral degree (PhD) in "Technical Materials" (doctoral study). The department also has accreditation for habilitation (associate professor) and the appointment of professors (professor) in the field of "Mechanical Technologies and Materials."

Department of Materials Engineering graduates are comprehensively prepared for research, development, and production of technical materials, including their technological processing into semifinished and finished products, as well as quality control and operational diagnostics. They possess a detailed understanding of methods for evaluating the structure and properties of technical materials, grasp the relationships between material composition, structure, and properties, and are knowledgeable of new materials, technologies for their production and processing, and methods for evaluating and influencing their utility properties. Additionally, they can design optimal materials from technological, economic, and ecological perspectives. The department places special emphasis on the targeted scientific education of doctoral students, who are required to complete internships at significant European workplaces for a minimum of three months during their studies.

The scientific research and teaching activities take place in various Laboratories. The department has achieved numerous significant research results throughout its existence. In the field of alloy crystallization research, they have successfully applied and verified an alloy with vermicular graphite for castings of combustion engines, glass molds, and mechanical products for transportation. The Department of Materials Engineering has been engaged in significant collaborations with both foreign (Italy, Germany, Austria, Poland, Hungary, Slovenia, and Czech Republic) and domestic universities, research institutes, and industrial companies that align with the department's scientific, professional, and educational profile. Through this targeted cooperation, the department conducts scientific research activities, experimental work, study stays, professional excursions, and internships for students and academic staff.